HAYES, MICHAEL

DETERMINATION OF IMPLANTATION PROFILES BY
(p,γ)-RESONANCE REACTIONS

PhD   UP   1995

Determination of implantation profiles by (p,γ)-resonance reactions

by

MICHAEL HAYES

Submitted in partial fulfilment of the requirements for the degree

PHILOSOPHIAE DOCTOR

in the

Faculty of Science (Department of Physics)

University of Pretoria

Pretoria

November 1995

Promoter: Professor E. Friedland

SUMMARY

Determination of implantation profiles by (p,γ)-resonance reactions

by

Michael Hayes

Promoter: Professor E. Friedland

Physics Department

Submitted in partial fulfilment of the requirements for the degree Philosophiae Doctor in the Faculty of Science.

The importance of ion implantation in physics and technology has steadily increased over the years. It is a reliable technique to introduce species into a target, altering the chemical, metallurgical, optical and electronic properties of the target material. Measurements of the depth distribution profiles of the implanted species provide information on a wide range of topics, including ion-solid interactions, doping and diffusion phenomena.

Several techniques have been developed in order to determine the depth distribution profiles of implanted ions. Destructive techniques, such as etching and sputtering provide this information, but can not be used in diffusion studies. Rutherford backscattering on the other hand is a non-destructive method, but is not very suitable for implanted ions of which the mass is smaller than that of the target material. Nuclear reaction analysis provides a non-destructive method of determining amongst others the implantation profile of ions with a mass number smaller or similar to that of the target material into which it is implanted. Nuclear reaction analyses with narrow and strong resonances are used for high resolution measurements. Such resonances are unfortunately not available for all light elements.

For this study, nuclear reaction analysis was employed to determine the profiles of $^{13}C^+$ and $^{27}Al^+$ ions implanted into silicon, gallium arsenide, magnesium and stainless steel. The $^{13}C^+$ ions were detected using the $^{13}C(p,\gamma)^{14}N$ nuclear reactions. Particularly suited for this study is the resonance at 1.75 MeV which has a resonance width of 75 eV. During the investigation of the $^{27}Al^+$ implantation, the $^{27}Al(p, \gamma)^{28}Si$ nuclear reaction was used. Here the resonance at 0.992 MeV is employed which has a resonance width of 100 eV. The projected range, straggling width, skewness and kurtosis of the implantation profiles are presented and compared to those values obtained by the theoretical predictions of the TRIM 91.14 code.

SAMEVATTING

Bepaling van inplanteringsprofiele deur (p,γ)-resonansie reaksies

deur

Michael Hayes

Studieleier: Professor E. Friedland

Departement Fisika

Voorgelê ter gedeeltelike vervulling van die vereistes vir die graad Philosophiae Doctor in die Fakulteit Natuurwetenskappe.

Die belangrikheid van iooninplantering in fisika en in die tegnologie, het oor die jare geleidelik toegeneem. Dit is 'n betroubare metode om spesies binne 'n skyf te plaas en sodoende die chemiese, metallurgiese, optiese en elektriese einskappe van die skyfmateriaal te verander. Inligting aangaande 'n wye gebied van onderwerpe, insluitende ioon–vastestof wisselwerking, dotering en diffusieverskynsels, word deur meting van die diepteverspreidingsprofiele van hierdie geïnplanteerde spesies verkry.

Verskeie metodes is ontwikkel om hierdie diepteverspreidingprofiele van die geïnplanteerde ione te bepaal. Etsing en verstuiwingsmetodes verskaf 'n vernietigende manier om die nodige inligting te bekom, maar kan nie tydens diffusieondersoeke gebruik word nie. Rutherfordterugverstrooiing aan die ander kant is 'n nie vernietigende metode, maar is nie heeltemal geskik vir inplanteringsione waarvan die massa kleiner is as die van die skyfmateriaal nie. Kernreaksieontleding verskaf 'n nie vernietigende metode om inplanteringsprofiele, van onder andere ione met 'n kleiner of soortgelyke massagetal as die skywe waarin dit geïnplanteer is, te bepaal. Kernreaksieontledings met smal en skerp resonansies word gebruik vir metings met 'n hoë oplosvermoë. Sulke resonansies is ongelukkig nie vir alle ligte ione beskikbaar nie.

Vir hierdie studie is kernreaksieontleding gebruik om die profiele van $^{13}C^+$ en $^{27}Al^+$ geïnplanteerde ione in silikon, galliumarsenied, magnesium en vlekvrye staal te bepaal. Die $^{13}C^+$ ione is waargeneem deur van die $^{13}C(p,\gamma)^{14}N$ kernreaksie gebruik te maak. Besonder geskik vir hierdie studie is die resonansie by 1.75 MeV wat 'n resonansiewydte van 75 eV het. Gedurende die ondersoek na die $^{27}Al^+$ inplantering, is van die $^{27}Al(p,\gamma)^{28}Si$ kernreaksie gebruik gemaak. Hier is die resonansie by 0.992 MeV gebruik wat 'n resonansiewydte van 100 eV het. Die waardes van die geprojekteerde reikwydte, afdwalingswydte, skeefheid en kurtosis van die inplanteringsprofiele word aangebied en vergelyk met die waardes wat deur die teoretiese voorspelling van die TRIM 91.14 kode verkry is.

Acknowledgements

I would sincerely like to thank the following persons for their contribution towards this study:

My promoter, Professor E. Friedland for his guidance and support throughout this study.

Professor F.D. Auret for his encouragement during this study.

Dr. Wolsey Barnard, Dr. Gerrit Myburg, Dr. Stewart Goodman and Mr. Walter Meyer for helpful discussions, assistance and encouragement.

Mr. Thilo Hauser for his willingness to assist with the measurements.

Mr. Roelf van Weele, Mr. Gerrit Pretorius and Mr. Peter Nawrotski for the technical support.

The staff of the Physics department for their support.

Dr John Cornell and his staff at the National Accelerator Centre for their help with the automatic energy scanning system.

Dr. Johan Prins, Mr. Mervin Naido and Ms. Lorraine De Matos for the implantation at the Schonland Research Centre for Nuclear Sciences.

Professor S. Kalbitzer and his staff for the implantations and the nuclear reaction measurements done at the Max-Planck-Institut für Kernphysik.

My wife, Elize, for her support, patience and encouragement during this study.

My mother for providing me with the initial opportunity to further my education.

The financial assistance of the Foundation for Research Development is greatly acknowledged.

TABLE OF CONTENTS

CHAPTER 5:   REVIEW OF PREVIOUS RESULTS

CHAPTER 6:   RESULTS AND DISCUSSION

CHAPTER 7:   SUMMARY OF RESULTS

CHAPTER 8:   REFERENCES   112

CHAPTER 9:   PUBLICATIONS   120

CHAPTER 1

INTRODUCTION

The stopping of projectiles in matter has been of scientific interest for over 500 years. The invention of the ballista for throwing large missiles through air for considerable distances brought one of the first examples of scientific research in stopping powers. Soon after the discovery of energetic particle emission from radioactive materials, there was interest in how these were slowed down in the traversing matter. The theory of stopping of ions in solids is discussed in chapter 2.

When an energetic ion or atom enters a solid, it loses energy by interactions with the electrons and the nucleus of the atoms in the solid until it comes to rest. These interactions happen at random so the projected range of the ion or atom is not a unique value, but has a distribution about the mean projected range. The implantation of ions into a solid is of interest to the physicist for the insights it gives to the atomic collision processes, and to the engineer for its technological applications. For these reasons a great deal of experimental and theoretical effort has gone into primarily determining the mean projected range, but also range distribution.

The experimental methods that have been developed to determine such depth profiles can be characterised by either their destructive or non-destructive nature. In destructive techniques, the surface of the sample is removed by either anodic oxidation or ion sputtering, the profiles being observed simultaneously by Auger-electron spectroscopy, secondary ion mass spectrometry or detection of electrons emitted from neutron-activated implantations. On the other hand, non-destructive methods offer obvious advantages, especially if variations of the depth profiles after implantations are under investigation. For heavy implanted ions or atoms, the Rutherford backscattering technique has been successfully applied by numerous authors.

1

If the implanted ions and the substrate atoms have similar masses, the energy difference between analysing particles backscattered from the ions and from the substrate atoms will be too small to detect. Similarly, when the mass of the implanted ions is smaller than the mass of the substrate atoms, the backscattering yield from the substrate atoms will mask the backscattered yield from the implanted ions. When the backscattering technique fails, the implantation profiles may be determined by nuclear reactions of the implanted ions with either neutrons or charged particles. This technique has the advantage that the energy of the analysing particles can be chosen in such a way that nuclear reactions between the particles and the substrate atoms are not possible or can be discriminated.

Using nuclear reactions with charged particles, two techniques can be applied. Firstly, depth profiling by way of the energy analysis method can be applied when the reaction cross section of the emitted particles varies smoothly with the energy of the analysing beam. Secondly, in the resonance method, a high intensity peak (resonance) is required in the reaction cross section of the emitted particles as a function of analysing beam energy. A more detailed discussion of the resonance method, which was employed during the nuclear reaction analysis in this study, is presented in chapter 3.

Chapter 4 deals with the experimental techniques and apparatus used during the preparation, implantation and analysis of implanted samples. One of the most important requirements of resonant nuclear reaction measurements is the ability to vary the energy of the incident beam in small, constant steps in a reliable and reproducible way. For this, an automatic energy scanning system was employed. Certain of the theoretical aspects and working principles of this scanning system are discussed.

A summary of the results from previous range parameter investigations is presented in chapter 5. In chapter 6 the results of this study are presented. Section 6.1 deals with the depth distributions of the samples that have been implanted with $^{13}C^+$ ions, while section 6.2 deals with the samples that have been implanted with $^{27}Al^+$ ions. In section 6.3 the third and fourth distribution moments of the theoretical predictions are investigated. A summary of this study is presented in chapter 7.

CHAPTER 2

STOPPING OF IONS IN SOLIDS

An energetic ion entering a solid target will lose its energy in a series of collisions with the electrons and nuclei of the target atoms and will ultimately be brought to rest. Such an ion is said to have been implanted into the target. Scientific interest in this process arises because it provides an important tool for studying a wide range of topics, including ion-solid interactions, radiation damage mechanisms, doping and diffusion phenomena. Commercial interest in the process arises because it provides a controllable technique for introducing atomic species into a target that can alter the chemical, optical, metallurgical and electronic properties of the target material. It is hence important to predict the effects caused by implantation, and to establish the characteristics of a particular implantation, for example, to what depths do the implanted species penetrate and what is their distribution.

2.1   PROCESSES OF ENERGY LOSS

An energetic ion that enters a target loses energy to a target atom by two independent processes, namely electronic and nuclear collisions. Electronic collisions involve energy transfer from the moving ion to the electrons of the target atoms (excitation and ionisation). Because of the small mass of the electrons, there is only a very small momentum transfer in such a collision, and the deflections of the ion will therefore usually be negligible. In nuclear collisions kinetic energy is transferred to the struck atoms (large momentum transfer), and this results in the projectile ion suffering relatively large deflections. At high ion energies electronic losses dominate the slowing down process. An empirical rule [1] for characterising this high energy region, is that if the projectile velocity v is greater than the orbital velocity v_1 of the valence electron in the atom (called the critical velocity) electronic stopping dominates, where

3

$$v_1 = v_0 Z_2^{2/3}$$

and v_0 is the Bohr velocity given by

$$v_0 = e^2 / h.$$

Z_2 is the atomic number of the target atom, e is the electron charge and h is Planck's constant. Even below this critical velocity, electronic stopping may still be the most important process, particularly for light particles striking heavy target atoms. For heavy particles at low energies nuclear stopping gradually assumes importance until it forms the major part of the energy loss process. The higher energy transfer to target atoms during nuclear interactions will result in the slowing down of the penetrating ion to occur faster. The large momentum transfer on the other hand will cause increasing scattering thereby enhancing lateral spread of the incident ion.

The rate of energy loss with distance $-\mathrm{d}E / \mathrm{d}x$ (also called the stopping power) can be expressed as a combination of the nuclear and the electronic stopping contributions [2]

$$-\frac{\mathrm{d}E}{\mathrm{d}x} = N\left[S_n(E) + S_e(E)\right]. \qquad\qquad 2.1.1$$

Here N is the number of target atoms per unit volume while $S_n(E)$ and $S_e(E)$ are the nuclear and electronic stopping powers respectively. By integrating equation 2.1.1, the total distance R travelled by an ion slowing down to rest from an initial energy E_0 is found as

$$R = \frac{1}{N}\int_0^{E_0} \frac{\mathrm{d}E}{S_n(E) + S_e(E)}. \qquad\qquad 2.1.2$$

4

The separation of the energy loss into two components ignores any possible correlation between the two. This correlation is probably not significant when the incident ion suffers many collisions [3], but is very important in single scattering studies.

Calculating the range from equation 2.1.2 is a very complicated process that requires exact values of the nuclear and electronic stopping powers for the range of energies involved. In most cases an exact solution of the problem is not possible and numerical methods have to be applied. Some of these methods will be discussed in section 2.2.
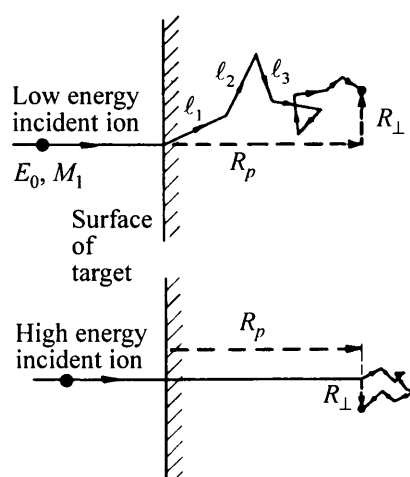
Fig. 2.1: Basic range concepts for incident ions with low and high incident energies [4].

Figure 2.1 depicts a simple illustration of an ion slowing down in a solid with a random array of atoms. For a high energy incident ion, the path is essentially a straight line in the original direction of motion since the energy loss of the ion is due to electronic stopping. A small amount of straggle occurs at the end of the path owing to nuclear collisions. At lower incident ion energies, where the nuclear and electronic stopping powers are more comparable, the ion path follows a zigzag course with many large deflections, the path length decreasing as the energy decreases. The projected range R_p is defined (with reference to figure 2.1) as the

5

component of the distance travelled by the ion in the original direction of the incident ion. The lateral range $R_\perp$ is defined as the component of the range perpendicular to the original direction of the incident ion. The total range $R = \sum \ell_i$, where ℓ_i is the path length between the ith and the (i-1)[th] deflection.
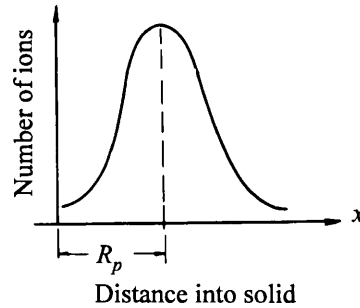
Fig. 2.2: Distribution of final implanted ion positions as function of distance in the solid [4].

As a beam of ions will have different random impact parameters with the surface atoms, each ion that strikes the target will not follow exactly the same path, even though its initial energy is fixed. This means that their collision sequences will be completely different from each other. Not only will the number of collisions suffered by an individual ion vary, but also its total range. This results in a distribution of stopping positions, which is usually assumed to have a Gaussian shape, as illustrated in figure 2.2.

2.2 ENERGY DEPENDENCE OF THE STOPPING CROSS SECTION

Figure 2.3 schematically illustrates how the electronic and nuclear contributions of the stopping cross section depend on the incident ion energy. When the incident ion energy is very low (eV range), the nuclear stopping and electronic stopping are comparable. For high ion energies (> 10 MeV range) stopping is well described by

6

the Bethe-Bloch formalism. The electronic stopping decreases when moving to higher energies in the Bethe-Bloch region. This is due to the fact that the higher the velocity of the incident ion, the less time it has to interact with each target atom it comes into contact with.
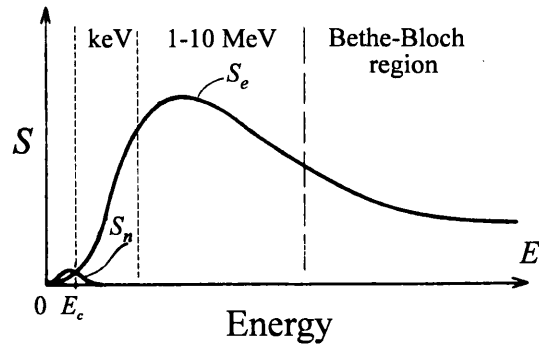
Fig. 2.3: **Typical dependencies of electronic S_e and nuclear S_n contributions to the stopping power S as a function of the incident particle energy [5]. The critical energy E_c is the energy above which the electronic stopping dominates.**

The complete Bethe-Bloch formula [6] is:

$$S_e = \frac{4\pi e^4 Z_1^2 Z_2}{m v^2}\left[\ln\left(\frac{2m v^2}{I}\right) + \ln\left(\frac{1}{1-\beta^2}\right) - \beta^2 - \frac{C}{Z_2}\right]. \qquad 2.2.1$$

Here m is the electron mass, $\beta = v / c$, v is the incident ion velocity, c is the velocity of light, I is the mean excitation potential and C/Z_2 describes the shell corrections. I is defined by the formula

$$\ln I = \sum_n f_n \ln E_n \qquad 2.2.2$$

where E_n and f_n are the possible energy transitions and corresponding oscillator strengths for the target atom. In practice, equation 2.2.2 is too complicated to use except for the simplest target atoms. Usually arguments of the Thomas-Fermi

7

nature have been used to estimate I. The simplest result of such an approach is Bloch's rule

$$I = I_0 Z_2,$$

where $I_0 \approx 10 \ eV$.

Two energy regions are of importance in this study. The first will be the region from 1 keV to 1000 keV and is called the low energy region while the second is the region from 1 MeV to 10 MeV, called the medium energy region.

2.2.1 THE LOW ENERGY REGION (1 keV < E < 1000 keV)

Ions with energies in this region have velocities smaller than the Thomas-Fermi velocity (also called the critical velocity). It is difficult to obtain a precise theoretical stopping formalism for these ions since their effective charges are not accurately known. The 150 keV ^{13}C$^+$ and ^{27}Al$^+$ ions as well as the 300 keV ^{20}Ne^{++} ions used in this study fall into this category. It can be observed from figure 2.3 that the electronic stopping increases approximately proportionally with velocity in this range. This is due to an increase in the average charge state of the ion with increasing velocity.

By far the most widely used theory for the ranges of incident ions into solids in this energy range is that developed by Lindhard, Scharff and Schiøtt (LSS) [2]. This work brought together all the pieces and bridging approximations made by various authors [7, 8], so that calculations of stopping and range distributions could, for the first time, be made with a single model. They considered the interactions between heavy ions on the basis of a Thomas-Fermi statistical model, which gives an atomic potential for the incident ion and the target atom of the form

$$V(r) = \frac{Z_1 Z_2 e^2}{4\pi\varepsilon_0 r} \phi\left(\frac{r}{a}\right). \qquad 2.2.3$$

8

Here $a = a_0\left(Z_1^{2/3} + Z_2^{2/3}\right)^{-1/2}$, a_0 is the Bohr radius, Z_1 and Z_2 are the atomic numbers of the incident ion and target atom respectively, ε_0 is the permittivity of free space, r is their separation, e is the electron charge and ϕ is the Thomas-Fermi screening function.

The LSS theory is applicable over the entire range of atomic species and incident energies up to the maximum stopping power. However, since it is based on the Thomas-Fermi model, it is most accurate for ions with many electrons in the energy range where they are neither fully stripped nor almost neutral. The LSS theory predicts a nuclear stopping power of the form shown in figure 2.4 (solid line curve). Energies E and distances R are expressed in terms of dimensionless parameters ε and ρ, where

$$\varepsilon = E \frac{aM_2}{Z_1 Z_2 e^2 \left(M_1 + M_2\right)} \qquad 2.2.4$$

and

$$\rho = RN 4\pi a^2 \frac{M_1 M_2}{\left(M_1 + M_2\right)^2}. \qquad 2.2.5$$

Here M_1 and M_2 are the incident ion and target atom masses respectively and N is the number of target atoms per unit volume.

Using these reduced energy and distance parameters, the reduced nuclear stopping power, that is $\left(d\varepsilon / d\rho\right)_n$, is a function of ε only, and is independent of incoming particle or stopping substance, so that the solid curve in figure 2.4 is a universal nuclear stopping power. Using the same units the reduced electronic stopping power $\left(d\varepsilon / d\rho\right)_e$ is given by [4]

$$\left[\frac{d\varepsilon}{d\rho}\right]_e = k\varepsilon^{1/2} \qquad 2.2.6$$

9

where

$$k = \xi_e \frac{0.0793 Z_1^{1/2} Z_2^{1/2} (M_1 + M_2)^{3/2}}{(Z_1^{2/3} + Z_2^{2/3})^{3/4} M_1^{3/2} M_2^{1/2}}$$

2.2.7

and

$$\xi_e \approx Z_1^{1/6}.$$
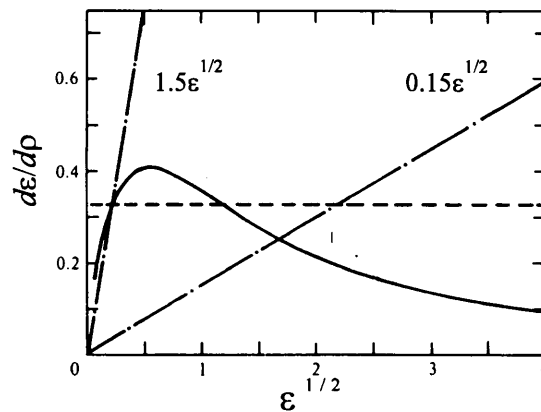
Fig. 2.4: **Nuclear and electronic stopping powers in reduced units. The solid curve represents the Thomas-Fermi nuclear stopping power S_n, while the dot and dash lines represent the electronic stopping power S_e for $k = 0.15$ and $k = 1.5$. The dashed line gives the nuclear stopping power S_n for the r^{-2} potential [4].**

A universal curve cannot be obtained for reduced electronic stopping, since the electronic stopping parameter k depends on the colliding atoms. The reduced average total path length can be calculated from the following equation

$$\rho = \int_0^\varepsilon d\varepsilon / [S_n(\varepsilon) + S_e(\varepsilon)].$$

2.2.8

10

Curves of ρ versus ε can be obtained by numerical integration of equation 2.2.8 using different values of the electronic stopping parameter k, as illustrated in figure 2.5. To use these curves for a particular experimental combination of Z_1, Z_2 and E, it is necessary to calculate ε and k from equations 2.2.4 and 2.2.7 respectively. The value of ρ is then read off (figure 2.5) and converted into a range R using equation 2.2.5. Expressing R in $\mu g/cm^2$ and E in keV, the relationships for ρ and ε are

$$\varepsilon = E \frac{32.5}{Z_1 Z_2 \left(Z_1^{2/3} + Z_2^{2/3}\right)^{1/2}} \frac{M_2}{\left(M_1 + M_2\right)} \qquad 2.2.9$$

and

$$\rho = R \frac{166}{\left(Z_1^{2/3} + Z_2^{2/3}\right)} \frac{M_1}{\left(M_1 + M_2\right)^2}. \qquad 2.2.10$$
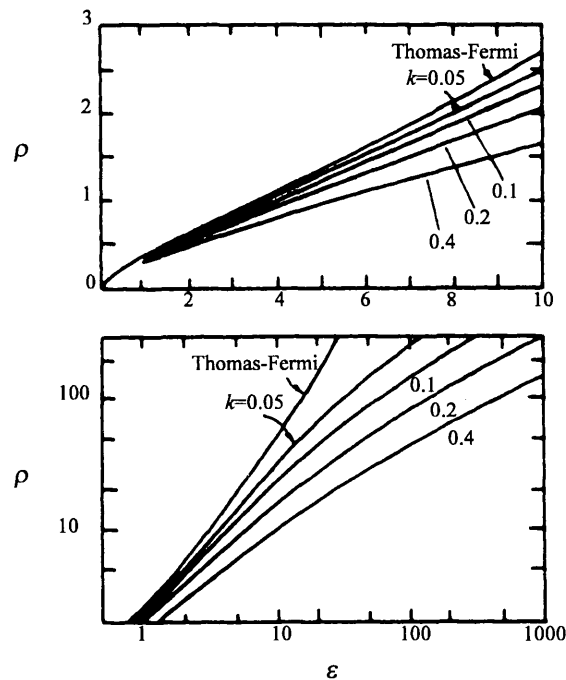
Fig. 2.5: Reduced range energy plots for various values of the electronic stopping parameter k [4].

11

The most interesting range quantity is the average projected range R_p, since this is the property usually measured experimentally. At very high energies, where the stopping is predominantly electronic, the total path length R and the average projected range R_p are to a good approximation equal. Conversely, for low energy particles, where nuclear stopping predominates R_p may be considerably less than R.

The approach adopted by the LSS theory to the problem of ion ranges provides an elegant set of formulae, graphs and tables from which the range distribution of any ion in any substrate may be found.

2.2.2 THE MEDIUM ENERGY REGION (1 MeV $< E <$ 10 MeV)

In this energy region the electronic stopping reaches a maximum, and starts decreasing towards the Bethe-Bloch region. This region is of the utmost importance to this study as it will describe the stopping of the 0.992 MeV and 1.75 MeV protons used in the nuclear reaction analysis. None of the stopping theories described thus far provide adequate explanations for experimentally observed stopping in this energy region. The only way to acquire an accurate description of the stopping is thus by the inter- and extrapolation of experimentally obtained data. This method was employed by Ziegler [6] in the formulation of his stopping curves for protons incident on 92 different elemental targets.

Ziegler based his analysis on the interpolation formula first proposed by Varelas and Biersack [9] to determine the stopping powers in this energy range, that is

$$\frac{1}{S} = \frac{1}{S_{low}} + \frac{1}{S_{high}}$$

or

$$S = \left(S_{low} S_{high} \right) / \left(S_{low} + S_{high} \right) \qquad 2.2.11$$

12

where S_{low} (low energy stopping) is given by

$$S_{low} = A_1 E^{1/2}$$

2.2.12

and S_{high} (high energy stopping) is given by

$$S_{high} = \frac{A_2}{E} \ln\left(1 + \frac{A_3}{E} + EA_4\right).$$

2.2.13

Here A_1, A_2 and A_3 are fitting constants and

$$A_4 = 4m / IM_1.$$

Here m is the electron mass, I is the mean excitation potential and M_1 is the mass of the incident ion. The fitting formula (equation 2.2.11) asymptotically agrees with the following equation

$$S_e = Z_1^{1/6} \times 8\pi e^2 a_0 \frac{Z_1 Z_2}{\left(Z_1^{2/3} + Z_2^{2/3}\right)^{3/2}} \times \frac{v}{v_0}$$

2.2.14

for incident ions at low energies, and with equation 2.2.1 for high energy ions. In equation 2.2.14, a_0 is the Bohr radius of the hydrogen atom and v_0 is the Bohr velocity.

To determine the high energy stopping powers (S_{high}), Ziegler used the Bethe stopping formula (equation 2.2.1) as the theoretical basis in the high energy region. He constructed fits to all the experimentally obtained stopping power data with ion energies > 400 keV. As no theoretical predictions relate energy loss to ion mass, all the data for protons, deuterons and tritons were reduced to a common energy scale by depicting them as a function of ion energy divided by ion mass.

Very little scatter is seen on the data of the stopping graphs at high energies and it is believed that the fits at high energies are accurate to 1%. For the energy range from

13

600-2000 keV there is more scatter of the experimental data. To obtain stopping powers below 600 keV, it is recommended that the stopping powers obtained by the low energy fits be used. At 600 keV the accuracy of the Bethe-fit is expected to be 3% [6].

It is of basic physical interest to obtain the factors by which the Lindhard formula (equation 2.2.14) must be multiplied to give the best fit to the low energy experimental data. It turned out that a velocity-proportional stopping did not give the best fit to the low energy data. Better fits were obtained by setting the stopping proportional to $E^{0.45}$. Thus, Ziegler decided to use the following equation instead of equation 2.2.12

$$S_{low} = A_1 E^{0.45}.$$

In order to interpolate stopping to elements without experimental data, Ziegler attempted to find a 2-parameter fit (one parameter for low energies and one parameter for high energies) and used the basic 4-parameter fit of equation 2.2.11. A_2 was found to decrease slowly with Z_2 and was approximated by

$$A_2 = (243 - 0.375Z_2)Z_2.$$

A_1 is critical in attempting to interpolate stopping to unmeasured elements. Ziegler used tabulated helium (He) stopping power values as a basis for interpolating between the empirical A_1 values. The parameter A_3 was found by linear interpolation between experimentally determined values, and it appears that the calculated stopping powers are very insensitive to the value of A_3.

2.3 ENERGY LOSS IN COMPOUNDS

The process by which a particle loses energy when it moves swiftly through a medium consists of a random sequence of independent encounters between the incident ion and an electron attached to an atom in the case of electronic energy

14

loss, or the ion and an atomic core in the case of nuclear energy loss. If the target contains more than one element, the situation differs only with respect to the type of atom the ion encounters. The energy lost to the electrons, or to the atomic core, in each encounter should be the same at a given ion velocity, regardless of the environment of the target atoms, since the interaction is considered to take place with only one atom at a time. The energy loss in a medium composed of various atomic species is thus the sum of the losses in the constituent elements, weighted proportionately to their abundance in the compound. This postulate is known as Bragg's rule and states that the stopping cross section $S^{A_m B_n}$ of a medium of composition $A_m B_n$ is given by

$$S^{A_m B_n} = mS^A + nS^B.$$
<div align="right">2.3.1</div>

Here S^A and S^B are the stopping cross sections of the atomic constituents A and B.

2.4 ENERGY STRAGGLING

The energy resolution is normally composed of two contributions, that is the instrumental energy resolution δE_i and energy straggling δE_s. The influence of the beam spread on the energy resolution is included in the instrumental energy resolution. Assuming the two contributions are independent, the total energy resolution δE is given by

$$\left(\delta E\right)^2 = \left(\delta E_i\right)^2 + \left(\delta E_s\right)^2.$$
<div align="right">2.4.1</div>

An energetic particle that moves through a medium loses energy through many individual encounters. Such a discrete process is subject to statistical fluctuations. As a result, identical energetic particles which have the same initial velocity, do not necessarily have exactly the same energy after passing through a thickness Δx of a homogeneous medium. The energy loss ΔE is subject to fluctuations. This phenomenon, sketched in figure 2.6, is called energy straggling. Energy straggling

<div align="center">15</div>

places a finite limit on the precision with which energy loss and hence depths can be resolved. It is thus very important to have quantitative information on the magnitude of energy straggling for any combination of incident ion energy, target material and incident ion type.
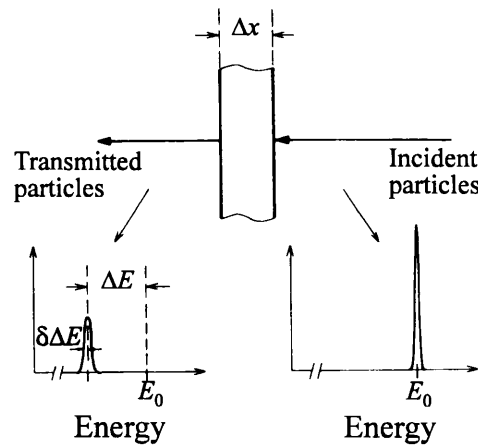
Fig. 2.6: A monoenergetic beam of energy E_0 loses energy ΔE in traversing a thickness Δx of a medium. Simultaneously, energy straggling broadens the energy profile.

Light particles such as protons in the mega-electron volt (MeV) range lose energy primarily by encounters with the electrons in the target, and the dominant contribution to energy straggling is the statistical fluctuations in these electronic interactions. Bohr derived a value for energy straggling (Ω_B) using the same classical model discussed in section 2.1. For a layer of thickness t, Bohr straggling has a variance

$$\Omega_B^2 = 4\pi \left(Z_1 e^2\right)^2 N Z_2 t. \tag{2.4.2}$$

Introducing the abbreviation

$$s^2 = 4\pi \left(Z_1 e^2\right)^2 N Z_2 \tag{2.4.3}$$

16

the Bohr value of energy straggling has the simple form of

$$\Omega_B^2 = s^2 t.$$
2.4.4

To determine the energy resolution in equation 2.4.1, one notes that (assuming a Gauss distribution) the full width at half maximum is $2(2\ln 2)^{1/2}$ times the standard deviation, that is

$$\delta E_s = 2.3548\,\Omega_B.$$
2.4.5

Bohr's theory predicts that energy straggling does not depend on the energy of the projectile, and that the root mean square value of the energy variation increases with the square root of the electron density per unit area ($NZ_2 t$) in the target. Bohr's model assumes that an individual energy transfer takes place between a free stationary electron and a fully ionised projectile of charge $Z_1 e$. These assumptions are fulfilled only in the Bethe-Bloch region. At energies near the maximum of the energy loss curve and below, the assumption of a fully ionised projectile is no longer valid. That electrons are bound to atoms and are not stationary as assumed, also becomes increasingly important as the projectile energy decreases. To account for this, Lindhard and Scharff [10] extended Bohr's theory and derived a correction factor for low and medium energy projectiles. They obtained

$$\Omega^2 = \Omega_B^2 \frac{L(\chi)}{2} \qquad \text{for } \chi \leq 3,$$

and

$$\Omega^2 = \Omega_B^2 \qquad \text{for } \chi \geq 3.$$

Here χ is a reduced energy variable given by

$$\chi = v^2 / Z_2 v_0^2,$$

17

with v the velocity of the projectile, $L(\chi) = \ln\left(2m_e v_1^2 \, / \, I\right)$ is the stopping number that appears in the Bethe-Bloch formula and v_0 is the Bohr velocity.

Bonderup and Hvelplund [11] extended this model by using explicit expressions of $\Omega(v,r)$ as a function of the atomic electron density $\rho(r)$ in a pseudo Thomas-Fermi type calculation:

$$\frac{\Omega^2}{\Omega_B^2} = \frac{1}{Z_2} \int_0^\infty 4\pi r^2 \rho(r) \left[\frac{\Omega^2(v,r)}{\Omega_B^2}\right] dr \, .$$

The electron charge density was calculated from a Lenz-Jensen model. Similar computations were performed by Chu [12] using more realistic Hartree-Slater atomic wave functions. The results of these calculations differ only slightly from each other. They predict stronger reductions of the straggling width for reduced energies ($\chi \leq 1$) than experimentally found. Besenbacher et al [13], who analysed the straggling results for some gasses at particle energies below 1 MeV/amu, explained these deviations from the theoretical results by additional straggling contributions from spatial atomic correlation effects and charge state fluctuations. However, similar deviations are reported for energy loss straggling in solids [14-17], where spatial correlation effects and charge state fluctuations are thought to be negligible. This deviation is probably due to a spatial correlation effect resulting from the Pauli exclusion principle which reduces the collision probability with bound electrons [18].

For the energy range of incident ions, used in this study (0.8 - 1.8 MeV), the theory predicted by Bohr is adequate to describe the energy straggling by the incident ion in penetrating the solid.

2.4.1 LINEAR ADDITIVITY OF ENERGY STRAGGLING

No reliable experimental data have been published on energy straggling in compounds and their relationship in straggling of the elemental targets. The most obvious suggestion of how energy straggling behaves in a compound $A_m C_n$ proceeds as follows. If N_A and N_C are the volume densities of the individual elements A and C, then the individual energy straggling in a thickness t of elements A and C is

$$\left(\Omega_B^A\right)^2 = 4\pi\left(Z_1 e^2\right)^2 N_A Z_A t,$$

and

$$\left(\Omega_B^C\right)^2 = 4\pi\left(Z_1 e^2\right)^2 N_C Z_C t.$$

This implies that for a volume density $N^{A_m C_n}$ of the compositional units $A_M C_N$ in the compound we can write

$$\frac{\left(\Omega_B^A\right)^2}{N_A Z_A t} = \frac{\left(\Omega_B^C\right)^2}{N_C Z_C t} = 4\pi\left(Z_1 e^2\right)^2.$$

This is independent of the target, the ratio simply given by the square of the energy variance per electron in a unit area of the target with thickness t.

An extension of Bohr's model to a compound target then predicts that straggling should apply independently of the composition of the target and will therefore be given by:

$$\left(\Omega_B^{A_m C_n}\right)^2 = 4\pi\left(Z_1 e^2\right)^2 N^{A_m C_n}\left(mZ_A + nZ_C\right)t.$$

19

2.5 COMPUTER CALCULATIONS OF STOPPING AND RANGE

The computer simulation of the slowing down and scattering of energetic ions in materials can be used in studies of ion implantation, radiation damage, sputtering and the reflection and transmission of ions. The Monte Carlo method as applied in simulation techniques has a number of distinct advantages over present analytical formulations based on transport theory. It allows a more rigorous treatment of elastic scattering, explicit consideration of surfaces and interfaces and easy determination of energy and angular distributions.

The transport of ions in matter (TRIM) program [19], which was used to calculate projected range parameters in this study, consists of following a large number of individual ion or particle "histories" in a target. Each history begins with a given energy, position and direction. The particle is assumed to change direction as a result of binary nuclear collisions and move in straight free-flight-paths between collisions. The energy is reduced as a result of nuclear and electronic energy losses, and the ion track is terminated either when the energy drops below a pre-specified value or when the particle's position is outside the target. The target is considered amorphous with atoms at random locations, and thus the directional properties of the crystal lattice are ignored. This method is applicable to a wide range of energies from approximately 0.1 keV to several MeV. It must be noted that TRIM is not a true Monte Carlo calculation in the sense of following an ion through a static lattice. Instead, it assumes a fictitious distribution of collision parameters and free path lengths in an amorphous solid.

The nuclear and electronic energy losses or stopping powers are assumed to be independent. Thus, particles lose energy in discrete amounts in nuclear collisions and continuously from electronic interactions. For the sake of computer efficiency, effects of minor influence on range distributions have been omitted from the computer program. These effects were carefully tested to check the validity of this omission. For a detailed description of the TRIM program the reader is referred to Ziegler [19].

20

CHAPTER 3

NUCLEAR REACTION ANALYSIS

Analytical methods based on electronic interactions have long been used in the materials analysis laboratory, but determinations based on nuclear spectroscopy are much more recent. If radioactivity, produced by irradiation is detected afterwards, the method is called activation analysis. On the other hand, if the emitted radiation is detected instantaneously, the method is called prompt radiation analysis. Such radiation is emitted within 10^{-14} seconds [20] after the nuclear reaction is initiated. This provides a distinction from activation analysis which relies on radioactive decay occurring over a longer time scale.

Most of the work performed using nuclear reactions is based on the detection of light elements for which charged particle induced reactions are particularly suitable and for which difficulties often arise in other methods of analysis. An important parameter of nuclear reactions is the reaction energy (Q value) which is often large so that the radiation produced is reasonably energetic. The background radiation is normally low at such high energies and the product radiation would therefore be easy to detect. Alternatively, the reaction energy can sometimes be negative so that the reaction only takes place when the incident radiation exceeds a threshold energy. As the charged particles penetrate the sample material they undergo energy loss by amongst others ionisation and this can be used to derive information on the depth distribution of a particular nuclide. In this, chapter nuclear interactions and prompt nuclear analysis are discussed.

3.1   NUCLEAR REACTIONS

In general nuclear reactions can be devided into two classes known as compound nucleus reactions and direct reactions. In the first, the incident particle is captured forming a nucleus in a highly excited state (called the compound nucleus), which then

21

decays to the ground state or a less excited state of the nucleus by ejecting a particle or emitting a gamma ray. In direct reactions, the incident particle interacts with individual nucleons in the nucleus while passing it without forming an intermediate state. The most obvious difference between the two reaction mechanisms is the interaction time. In direct reactions, this is of the order of the transit time of the incident particle over the nuclear diameter ($\sim 10^{-22}$ seconds) while the fastest decay times of compound nuclei are orders of magnitude longer.

3.1.1 THE COMPOUND NUCLEUS

An energetic particle approaching a nucleus will be in a distinct angular momentum state relative to the centre of the nucleus. When the particle enters the nucleus, it enters a doorway state appropriate to its energy and angular momentum. This particle can now collide with a number of the other nucleons. In all these collisions energy must be approximately conserved while angular momentum and parity must be conserved. All nucleons involved in collisions must be in allowed (in the shell-theory potential) and otherwise unoccupied orbits after, as well as before collisions.

There are several orbits in each shell that can be reached without violation of the above mentioned rules. Thus, while the complete sharing of available energy among all the nucleons is unlikely, the excitation energy is shared amongst a great number of nucleons. The wave function for the state of the compound nucleus includes a term from each of the orbital configurations that can be reached by these collisions. Only a small fraction of these terms allow a nucleon to be emitted and it is thus only after a large number of collisions that a nucleon will be emitted.

3.1.2 CLASSIFICATION OF ELECTROMAGNETIC TRANSITIONS

When a nucleon is in a high energy state while a low energy state is unfilled, it can jump to the lower energy state with the energy released in the process coming off as a quantum of electromagnetic radiation commonly called a gamma ray. It must

22

however be remembered that single particle transitions are the exception, and most transitions are between collective states.

The nucleus can be treated as an extended charge distribution in which currents flow, generated by the orbital as well as the spin motions of the nucleons. The electric and magnetic fields produced are complicated and the actual charge distribution is therefore expanded in multipole moments.

During a transition the emitted electromagnetic field can also be described by electric and magnetic multipole moments. Although the parity property is of no particular importance in a classical radiation problem, it is an important parameter for electromagnetic transitions between nuclear states. For a mutipole radiation between the initial state i and the final state f producing a parity change π_γ, conservation of parity would require that

$$\pi_i = \pi_f \pi_\gamma \qquad\qquad 3.1.1$$

where π_γ is the parity of the electromagnetic radiation field. It has been experimentally found that this selection rule is obeyed for electromagnetic transitions. In quantum mechanical calculations [21] each multipole moment of order L_γ is found to produce a radiation field that carries off an angular momentum $\overline{L}_\gamma \hbar$. The conservation of angular momentum ($\overline{I}$) thus requires that

$$\overline{I}_i = \overline{I}_f + \overline{L}_\gamma. \qquad\qquad 3.1.2$$

The parity change π_γ is directly related to L_γ and

$$\pi_\gamma = (-1)^{L_\gamma} \text{ for electric multipole radiation, while}$$

$$\pi_\gamma = -(-1)^{L_\gamma} \text{ for magnetic multipole radiation.}$$

23

The classification of a few common types (lowest order) of transitions with their selection rules is given in table 3.1. In a given transition, one or at the most two multipole radiations are of importance. This occurs because in the expression for the gamma transition probability, given by

$$\lambda_\gamma = \lambda_\gamma(E1) + \lambda_\gamma(M1) + \lambda_\gamma(E2) + \ldots,$$

only a limited number of terms are allowed by the selection rules (equation 3.1.1 and equation 3.1.2). For these terms, the gamma decay probability of a multipole of a lower order exceeds that of the next higher order by a factor of 10^2 to 10^4 [21].

Table 3.1: **Classification of electromagnetic transitions.**

Name	Abbreviation	L_γ	π_γ
Electric dipole	$E1$	1	-1
Magnetic dipole	$M1$	1	+1
Electric quadrupole	$E2$	2	+1
Magnetic quadrupole	$M2$	2	-1
Electric octupole	$E3$	3	-1
Magnetic octupole	$M3$	3	+1
Electric 16-pole	$E4$	4	+1
Magnetic 16-pole	$M4$	4	-1

Because the nuclear wave functions are only approximately known, theoretical estimates of the decay constants are also only approximate. For a single proton transition in which the final state is an s state, Weisskopf [21] has estimated the decay constant for electric mutipole radiation by

$$\lambda_\gamma(EL_\gamma) \approx S \frac{e^2}{\hbar \lambda_\gamma} \left(\frac{R}{\lambda_\gamma} \right)^{2L_\gamma} \qquad 3.1.3$$

and the decay constant for magnetic mutipole radiation by

24

$$\lambda_\gamma (ML_\gamma) \approx 10 \left(\frac{\hbar}{M_p cR} \right)^2 \lambda_\gamma (EL_\gamma) . \qquad\qquad 3.1.4$$

Here R is the radius of the nucleus, M_p is the proton mass, $\lambdabar_\gamma$ is the wavelength of the electromagnetic radiation divided by 2π and S is a statistical factor given by

$$S = \frac{2(L_\gamma + 1)}{L_\gamma \left[1 \times 3 \times 5 \cdots (2L_\gamma + 1) \right]^2} \left(\frac{3}{L_\gamma + 3} \right)^2 .$$

Typical values of $R / \lambdabar_\gamma$ are around 1/40 [22]. Multipoles that differ by unity in their order would thus, even without the factor S, differ by 10^{-3} in their decay rate. The factor S on the other hand also decreases by about 10^{-2} for each order [23]. From equations 3.1.3 and 3.1.4 it is also clear that magnetic multipole radiation is less probable than electric multipole radiation of the same order. Figure 3.1 illustrates the results of equations 3.1.3 and equation 3.1.4 as a function of gamma ray energy for a nucleus with A = 55.
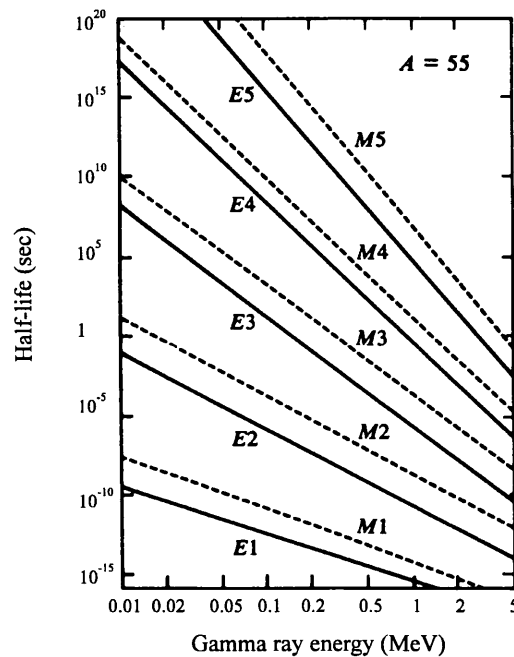
Fig. 3.1: Half-life calculations for gamma ray multipole emission as a function of gamma ray energy according to the Weisskopf estimates for a nucleus with A = 55.

25

3.1.3 GAMMA RADIATION FROM A COMPOUND NUCLEUS

If the compound nucleus is designated by $_Z^A X$ and the energy of the excited state of the nucleus by E^*, a typical radioactive decay is illustrated in figure 3.2. The excited level E^* can decay by either the emission of gamma rays, $\gamma_1, \gamma_2, \gamma_3$ and γ_4 to reach the ground state of the compound nucleus, or by ejecting protons of three distinct energies p_0, p_1 and p_2. The proton groups $p_1 + p_2$ feed excited states of the residual nucleus $_{Z-1}^{A-1} Y$, which can decay to the ground state by emitting the gamma rays γ_5, γ_6 and γ_7. This residual nucleus may be unstable and decays to the excited or ground state of the nucleus $_Z^{A-1} X$ by ejecting a β-particle. The γ-transitions $(\gamma_1 - \gamma_7)$ and proton emissions are likely to occur very rapidly after the formation of the compound nucleus, that is within $< 10^{-12}$ seconds [24], but the half life for the β-decay and hence the emission of γ_8 will take much longer. It must however be noted that the above description is only a possible radioactive decay scheme and particle decay is not possible in all cases.
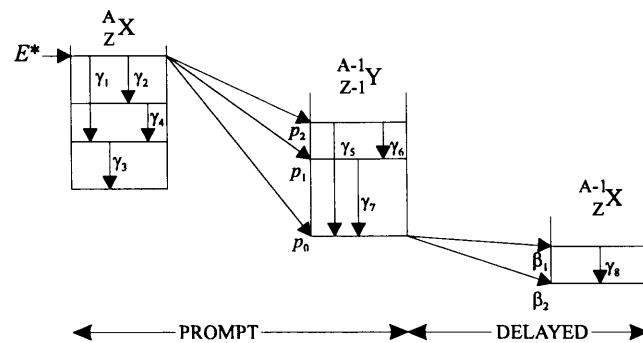
Fig. 3.2: **Energy level representation of an excited compound nucleus $_Z^A X$ in an excited state E^* which promptly decays by γ-ray emission to its ground state or by proton emission to the excited states of the residual nucleus $_{Z-1}^{A-1} Y$. This nucleus is unstable and decays during a longer time by beta emission to the nucleus $_Z^{A-1} X$.**

26

This difference in the radioactive decay time gives rise to the two methods of analysing radioactive decay. When the radionuclide has a half-life that is sufficiently long so that the sample under investigation can be removed from the place of irradiation before all the nuclei decay, delayed analysis methods are applied. When the emission is measured while the irradiation is in progress, prompt analysis techniques are applied.

3.2 PROMPT RADIATION ANALYSIS

In prompt radiation analysis (PRA), the presence of an element in a sample is detected through the nuclear radiation emitted instantaneously from nuclear reactions produced in the target by the irradiating (analysing) beam. One of the important advantages of PRA is that it can be used to measure the depth distribution of elements in the surface or near surface region. The dependence of the emitted radiation on depth is due to the energy loss suffered by the incident ion on traversing the target and to the energy loss suffered by the ion emitted from the reaction as it emerges from within the target.

In the use of PRA for depth profiles, two methods can be applied. 1. The energy-analysis method is applied when the nuclear cross section is a smoothly varying function of energy. During such an analysis the energy of the analysing beam is kept fixed, and the energy spectrum of particles emitted by the reaction is recorded. From this spectrum the depth profile can be derived. 2. When a sharp peak in the cross section (σ) as a function of incident particle energy is present as illustrated in figure 3.3, the resonance method is applied. Here the depth profile is derived from the measurement of the nuclear reaction yield as a function of the analysing beam energy.
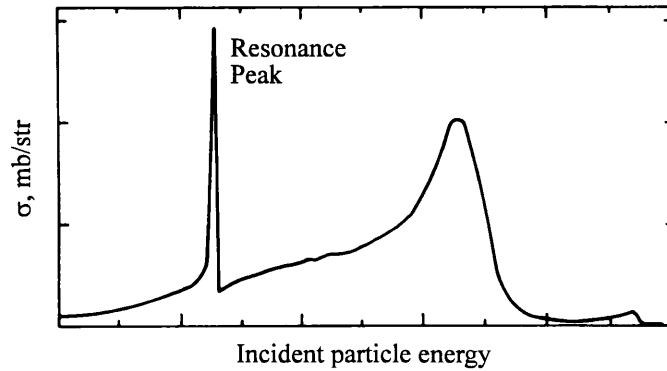
Fig. 3.3: Cross section (σ) in millibarns (mb) per steradian (Str) versus incident particle energy for a resonant nuclear reaction [25].

During this study, nuclear reaction analysis with the resonance method was employed and therefore only this method will be discussed in section 3.2.1.

3.2.1 THE RESONANCE METHOD

Many nuclear reactions have the property that the reaction yield exhibit's one or more sharp peaks or resonances as a function of incident particle energy. The use of the resonance method in the depth profiling of trace elements takes advantage of the sharp peak in the nuclear reaction cross section. This method consists of measuring the reaction yield (most often γ-rays) due to the interaction between the incident particle and the impurity atoms as a function of incident particle energy.

Incident ions having an energy E_0 larger than the resonance energy E_R are slowed down until E_R is reached at depth x, where the nuclear reaction will then occur at a rate proportional to the impurity concentration. The depth x and the incident particle energy E_0 are related through the equation

$$E_0 = E_R + \left(\frac{dE}{dx}\right)_{in} \frac{x}{\cos\theta_1}. \qquad 3.2.1$$

28

Here θ_1 is the angle between the incident particle and the surface normal while the stopping power $(dE/dx)_{in}$ for the incident particle is assumed to be constant in the small energy interval $E_0 \geq E \geq E_R$ $((dE/dx)_{E_0} \approx (dE/dx)_{E_R})$.

The top part of figure 3.4 shows a sample of SiO_2 with two aluminium implanted regions. The middle part of the figure exhibits the yield of photons as a function of energy that would be obtained in the idealised case where the intrinsic width of the resonance, the Doppler broadening which is produced by the thermal motion of the reactant atoms in the target, the beam energy distribution, energy loss straggling, etc. are all neglected. The bottom part of the figure represents the experimentally observed yield curves. From this it is clear that, depending on the numerical values of the different contributions, some of the above mentioned factors will have to be taken into account when performing a resonance reaction analysis.
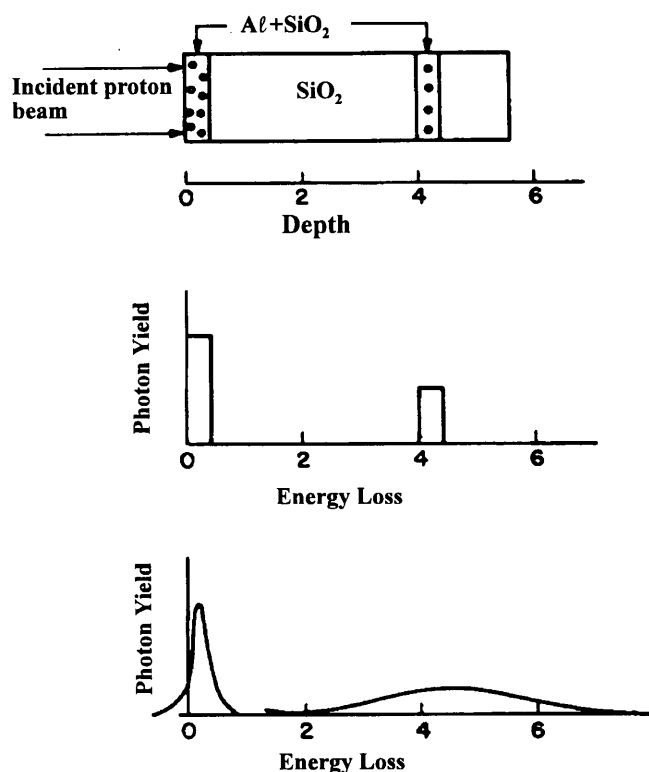
Fig. 3.4: Diagram to illustrate in simplified form how a nuclear resonance reaction can provide depth distribution information about an element in a sample [26].

29

In a typical resonance analysis, one would consider flat targets with a laterally uniform composition that contain the nuclei of interest with a depth dependent concentration $C(x)$. These targets would be bombarded perpendicular with an ion beam, and the reaction yield produced by the well chosen nuclear reaction will be detected at an angle θ, with solid angle Ω. If the accelerator energy setting is given by $\overline{E}_0$, and the probability of an incoming particle to producing a detected event at a depth interval $x \to x + dx$ is given by $q(x, \overline{E}_0)dx$, the mean number of detected events for a number of incoming particles n_0 is given by [27]

$$N(\overline{E}_0) = n_0 \int_0^\infty C(x)\, q(x, \overline{E}_0)\, dx .$$

<div align="right">3.2.2</div>

The infinite upper limit of the integral, in the above equation, means integration up to a value of x above which $C(x) = 0$, or $q(x, \overline{E}_0)dx = 0$, or to the maximum depth from which the emitted particle would be detected.

In principle, depth profiling by resonance reactions consists of recording yield curves when the experimental conditions are chosen such that $q(x, \overline{E}_0)$ presents a narrow peak near a depth x_0 depending on $\overline{E}_0$. By varying $\overline{E}_0$, $C(x)$ is then sampled mainly in the vicinity of x_0, as illustrated in figure 3.5 (b). The depth resolution would now be set by the width of $q(x, \overline{E}_0)$.

If the energy of the accelerator is set at $\overline{E}_0$ and the probability of finding the energy $E \to E + dE$ of a beam particle that penetrates to a depth x by $g(E, \overline{E}_0, x)dE$, then the expression of $q(x, \overline{E}_0)$ is found by integrating the cross section $\sigma_\theta(E)$ over all the possible energies E, weighted by the probability $g(E, \overline{E}_0, x)dE$. It is thus possible to write

<div align="center">30</div>

$$q\left(x,\overline{E}_0\right) = \Omega\xi \int_0^{E_0} \sigma_\theta(E)\,g\left(E,\overline{E}_0,x\right)\mathrm{d}E . \qquad\qquad 3.2.3$$

Here ξ is the detection efficiency, If one sets $x = 0$, $g\left(E,\overline{E}_0,0\right)$ is the energy spread of the beam which depends only on the accelerator. $\overline{E}_0$ is thus the mean energy value of the beam particles. If $\sigma_\theta(E)$ is sharply peaked at $E = E_R$, as illustrated in figure 3.5 (a), the reaction yield will only be large in the vicinity of the depths for which $g\left(E,\overline{E}_0,x\right)$ is also peaked near $E = E_R$. This is so around the value x_0 where the mean energy loss is near $\overline{E}_0 - E_R$, that is

$$\overline{E}_0 - E_R \approx x_0\,\frac{\mathrm{d}E}{\mathrm{d}x}. \qquad\qquad 3.2.4$$
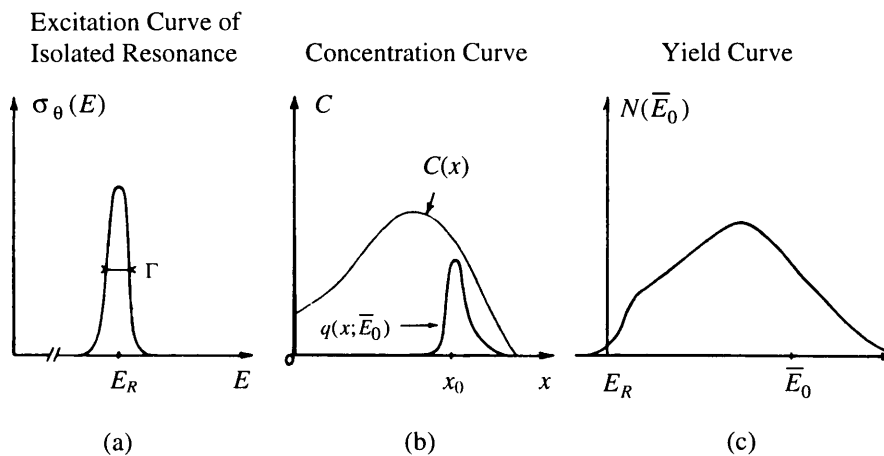
Fig. 3.5: **Principles of depth profiling with the resonance technique.**

It can be seen from figure 3.5 (b) that $q\left(x,\overline{E}_0\right)$ will be sharply peaked around the value x_0. As the energy straggling of the beam particles increases with the penetration x, $g\left(E,\overline{E}_0,x\right)$ and therefore $q\left(x,\overline{E}_0\right)$ is broadened with respect to the beam spread $g\left(E,\overline{E}_0,0\right)$. The depth resolution thus deteriorates with increasing x.

If $C(x)$ extends over moderate depths, the energy losses ΔE that are considered are small with respect to the beam energy, that is

$$\Delta E \ll \overline{E}_0 . \qquad\qquad 3.2.5$$

Under these conditions the stopping power does not depend appreciably on the actual particle energy ($E = \overline{E}_0 - \Delta E$). The assumption can thus be made that the stopping power is the same at all depths and for all particles as for the mean starting energy $\overline{E}_0$ at the surface. Equation 3.2.2 through equation 3.2.3 may now be expressed as the double integral

$$N(\overline{E}_0) = n_0 \Omega \xi \int_0^\infty \int_0^{E_0} C(x) \sigma_\theta (E) \, g(E, \overline{E}_0, x) \mathrm{d}E \, \mathrm{d}x . \qquad\qquad 3.2.6$$

The probability function $g(E, \overline{E}_0, x)\mathrm{d}E$ can be factorised, so that

$$g(E, \overline{E}_0, x) = g'(E) \, g''(\overline{E}_0, x)$$

and

$$\int_0^{E_0} \sigma_\theta (E) \, g'(E) \, g''(\overline{E}_0, x) \, \mathrm{d}E \approx \hat{\sigma}_\theta (\overline{E}_0) \, g''(\overline{E}_0, x) \int_0^{E_0} g'(E) \mathrm{d}E$$
$$= \hat{\sigma}_\theta (\overline{E}_0) \, g''(\overline{E}_0, x) \, \hat{h}(\overline{E}_0)$$

with

$$\hat{h}(\overline{E}_0) = \int_0^{E_0} g(E) \, \mathrm{d}E .$$

Equation 3.2.6 is therefore simplified into a double convolution [27, 28]

32

$$N\left(\overline{E}_0\right) = n_0 \Omega \xi \, \hat{\sigma}_\theta\left(\overline{E}_0\right) \, \hat{h}\left(\overline{E}_0\right) \int_0^\infty C(x) \, g''\left(\overline{E}_0, x\right) dx \,. \qquad 3.2.7$$

The first part of the convolution (up to the integral) may be written as

$$\rho\left(\overline{E}_0\right) = \hat{\sigma}_\theta\left(\overline{E}_0\right) \, \hat{h}\left(\overline{E}_0\right) = \hat{\sigma}_\theta\left(\overline{E}_0\right) \, \hat{h}_B\left(\overline{E}_0\right) \, \hat{h}_D\left(\overline{E}_0\right) . \qquad 3.2.8$$

Here $\hat{\sigma}_\theta(\overline{E}_0)$ is the resonance line shape centered at E_R and $\rho\left(\overline{E}_0\right)$ is the overall energy resolution function (instrument function) of the measurement. The effective incident particle beam energy spread seen by the reacting nuclei is itself the sum of the actual accelerator beam energy spread, with centered probability density $\hat{h}_B\left(\overline{E}_0\right)$ and of the apparent beam energy spread due to the thermal agitation induced Doppler broadening, with centered and symmetrical probability density $\hat{h}_D\left(\overline{E}_0\right)$. For our investigation, the contribution of $\hat{\sigma}_\theta(\overline{E}_0)$ was negligible (75 and 100 eV) when compared with the overall instrumental energy resolution (1-2 keV). Because the accelerator beam energy spread is in the order of 1 keV, the assumption can be made that the beam energy spread due to Doppler broading is also negligible.

The last factor in equation 3.2.7 (the integral) depends on the target, the nature of the incoming particles and on the resonance energy E_R in the vicinity of which the measurement is carried out. This factor is critically affected by the energy straggling process undergone by the incident particles in the target.

In this investigation the correction for the instrumental energy resolution $\rho(E)$ and the straggling $g''\left(\overline{E}_0, x\right)$ is done simultaneously when the yield curves of the implanted samples were analysed. In order to make these corrections, a Gaussian fit was made to the experimental yield curve. The computer code PROFIL, that uses a deconvolution algorithm described in detail by Friedland [29], was then used to determine correction factors for each data point by using the fitted yield curve. Finally, each data point on the original yield curve was multiplied by these correction factors to obtain the corrected implantation profile.

33

CHAPTER 4

EXPERIMENTAL PROCEDURE

Nuclear reaction analyses (NRA) were performed on implantation profiles of $^{13}C^+$ and $^{27}Al^+$ implanted gallium arsenide (GaAs), silicon (Si), magnesium (Mg) and stainless steel samples by using the $^{13}C(p,\gamma)^{14}N$ and $^{27}Al(p,\gamma)^{28}Si$ reactions. Decay schemes of these nuclear reactions are presented and the modifications to the existing apparatus, needed to perform NRA, are discussed. Other aspects that will be discussed in this chapter include sample preparation, method of data acquisition and analysis.

4.1 SAMPLE PROPERTIES AND PREPARATION

Small discs of approximately 3 mm thickness with diameters of 10 mm and 13 mm were cut with a Materials Science Spark Erosion Unit from cylinders of stainless steel and magnesium respectively. The stainless steel was of the type 304 (72% Fe / 18% Cr / 10% Ni) while the magnesium was a single crystal grown along the <0001> direction so that the magnesium discs had surfaces normal to this direction.

One face of each disc was mechanically polished, using a Kent Mark II mechanical polisher, and three diamond resins varying in the size from 15, 3 and 0,25 microns (in that order). Each sample was then ultrasonically cleaned in pure ethanol after which it was electrolytically polished with a Polectrol electrolytical polisher. A solution of 8.5% perchloric acid, 83% methanol and 8.5% butyl glycol was used as electrolyte for the stainless steel samples. A solution of 8% perchloric acid, 9% distilled water, 73% ethanol and 10% butyl glycol was used as electrolyte for the magnesium samples. The samples were then given a rinse in deionised water and dried by blowing nitrogen gas over them.

34

Gallium arsenide and the silicon samples were obtained from single crystal wafers grown along the <100> direction. These wafers were cleaved along the (100) cleavage planes to obtain samples of approximately 1 cm^2.

The majority of the implantations were performed with a Varian-Extrion implanter at the Wits-CSIR Schonland Research Centre for Nuclear Sciences in Johannesburg and the rest at the Max Planck-Institut für Kernphysik in Heidelberg Germany. Table 4.1 contains the implantation parameters for the single crystal gallium arsenide, silicon and magnesium as well as the polycrystalline stainless steel. It must be noted that the implantations were performed at 300 K and 77 K, and the surface region of some of the silicon samples was amorphized by pre-implantation with ^{20}Ne^{++}.

During the implantations, the sample holder was tilted in such a way that the normal of the target surface was at an angle of 7° to the direction of the impinging ions. This was done to prevent any channelling of the implanted ions in the single crystals. The ^{13}C$^+$ and ^{27}Al$^+$ implants were performed with an accelerating energy of 150 keV and the ^{20}Ne^{++} implants with an accelerating energy of 300 keV. The 300 keV ^{20}Ne^{++} implantation ensured amorphization to a depth approximately one and a half times the projected range of the ^{13}C$^+$ implantations. A typical value for the average vacuum during the implantations was 10^{-6} mbar. At a dose rate of $\pm 10^{13}$ ions cm^{-2}s^{-1}, implantation times of around 30 minutes and 90 minutes were required for the 2×10^{16} and 5×10^{16} ions cm^{-2} implantation fluences respectively. Using the same implantation rate, the implantation time for the 1×10^{15} ions cm^{-2} implantation fluence was around 2 minutes.

Table 4.1: Implantation parameters of the single crystals GaAs, Si and Mg, and the polycrystalline stainless steel. All the ions were implanted at 150 keV.

TARGET	IMPLANTED ION	IMPLANTED FLUENCE (cm^{-2})	IMPLANTATION TEMPERATURE (K)
Silicon 01	$^{20}Ne^{++}$	1×10^{15}	300
	$^{13}C^{+}$	2×10^{16}	300
Silicon 02	$^{20}Ne^{++}$	1×10^{15}	77
	$^{13}C^{+}$	2×10^{16}	77
Silicon 03	$^{13}C^{+}$	2×10^{16}	300
Silicon 04	$^{13}C^{+}$	2×10^{16}	77
Silicon 05	$^{27}Al^{+}$	5×10^{16}	300
Silicon 06	$^{27}Al^{+}$	5×10^{16}	77
Gallium Arsenide 01	$^{13}C^{+}$	5×10^{16}	300
Gallium Arsenide 02	$^{13}C^{+}$	5×10^{16}	77
Gallium Arsenide 03	$^{27}Al^{+}$	5×10^{16}	300
Gallium Arsenide 04	$^{27}Al^{+}$	5×10^{16}	77
Magnesium 01	$^{13}C^{+}$	5×10^{16}	300
Magnesium 02	$^{13}C^{+}$	5×10^{16}	77
Magnesium 03	$^{27}Al^{+}$	5×10^{16}	300
Magnesium 04	$^{27}Al^{+}$	5×10^{16}	77
Magnesium 05	$^{27}Al^{+}$	5×10^{16}	300
Magnesium 06	$^{27}Al^{+}$	5×10^{16}	77
Magnesium 07	$^{27}Al^{+}$	5×10^{16}	300
Magnesium 08	$^{27}Al^{+}$	5×10^{16}	77
Stainless Steel 01	$^{13}C^{+}$	5×10^{16}	300
Stainless Steel 02	$^{13}C^{+}$	5×10^{16}	77
Stainless Steel 03	$^{27}Al^{+}$	5×10^{16}	300
Stainless Steel 04	$^{27}Al^{+}$	5×10^{16}	77

36

4.2 DETECTOR CONFIGURATION

The two detectors used during the nuclear reaction analysis were a 5 cm EG&G Ortec high-purity intrinsic germanium coaxial photon detector and a 5 inch Bicron NaI-scintillation detector. Although both detectors were positioned outside the evacuated chamber, the ports were modified to position the detectors as close as possible to the target holder to ensure a large as possible solid angle. It must also be noted that the two detectors as well as the proton beam are in the same horizontal plane. The germanium detector was positioned at the largest possible scattering angle available in the existing set-up where it was possible to make a port ($\theta = 127°$) while the NaI-scintillation detector was placed at an existing port ($\theta = 90°$) on the opposite side of the vacuum chamber. Figure 4.1 illustrates the configuration of the detectors with respect to the target chamber.
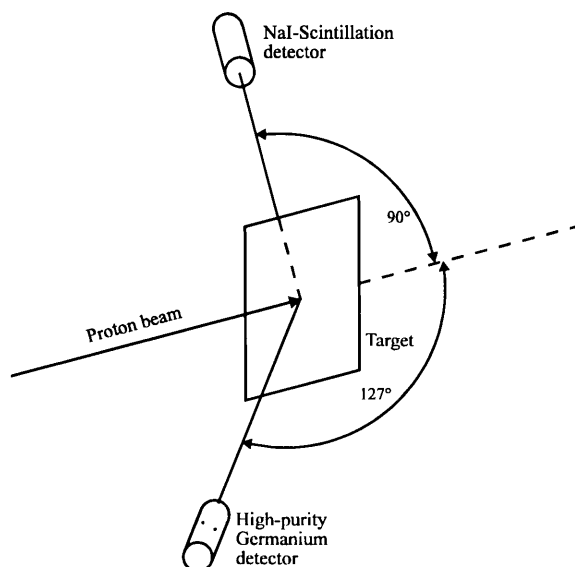

Fig. 4.1: Detector and target configuration. The detectors and the proton beam are in the same horizontal plane.

It was originally decided to use a germanium detector for this study as it has a high energy resolution and low background yield. This high energy resolution originates from the effectiveness with which the charges, that are created by the incident

37

particle, are collected. On the other hand, because it is not possible to grow large diameter germanium crystals, these detectors will only have a small volume in which the incident photons can be stopped and the efficiency of such detectors will be low. During this study it was found that, although we had excellent energy resolution, the count speed of the germanium detector was just not high enough. It was thus decided to install a NaI-scintillation detector as well to get a higher count rate.

The advantage of the NaI-scintillation detector lies in its high efficiency. This efficiency is due to the ability to grow large diameter NaI crystals and there is thus a large volume in which to stop the incident particles. The poor energy resolution and high background yield of this type of detector results from the lower effectiveness with which the light quanta, created in the crystal by the incident particles, are collected.

To optimise the counting efficiency, both detectors were used simultaneously during this investigation. The yield from the NaI-scintallation detector was about four times higher than that from the germanium detector.

4.3   DATA ACQUISITION

A block diagram of the apparatus used in the detection, amplification and collection of the gamma ray yield as well as the apparatus used in the energy scanning can be seen in figure 4.2. The nuclear reactions used for the analysis and the gamma rays emitted from them will be discussed in more detail in sections 4.5 and 4.6. The gamma rays detected by the germanium and NaI detectors were amplified by pre-amplifiers (contained in the detectors) before being fed into the main amplifiers.

As a result of the high energy of the emitted gamma rays, the majority of them form electron-positron pairs when stopped by the detector. This results in the detection of three energy peaks, namely, a photo peak and two escape peaks. To optimise the signal to noise ratio an energy window is selected to include all three peaks. The

38

first step in selecting an energy window is the calibration of the multi channel analyser (MCA) in pulse height analysis (PHA) operation. Gamma ray sources for which the energies of the emitted gamma rays are well known, such as ^{60}Co and ^{137}Cs, are used in this calibration.
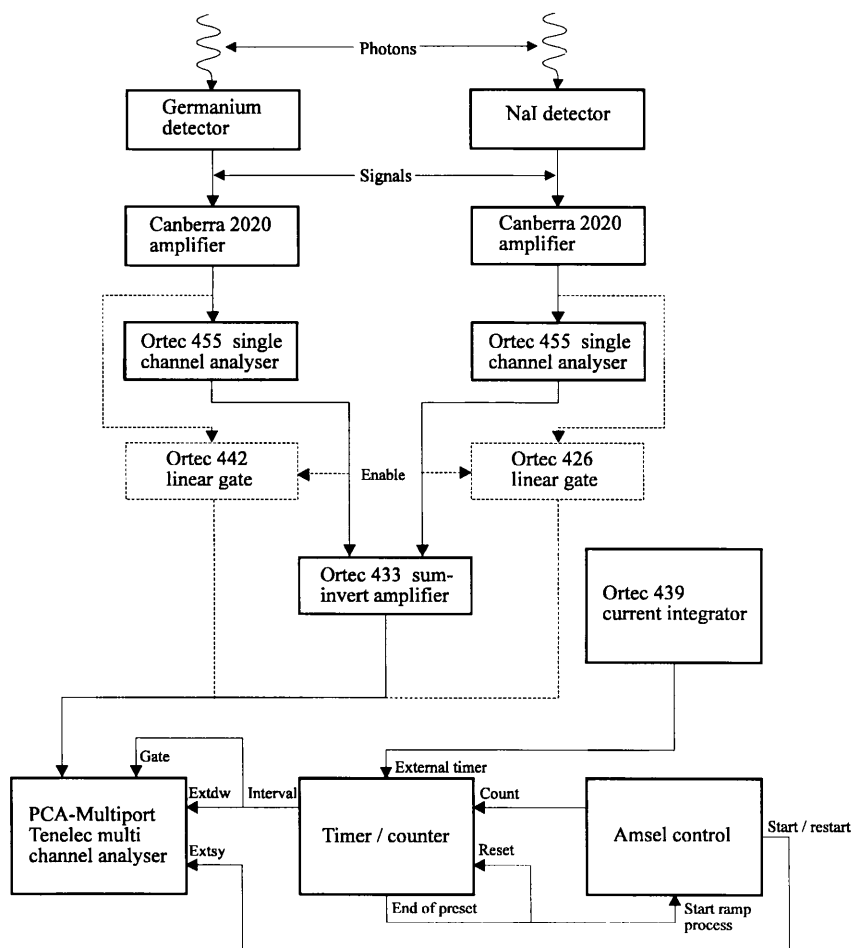
Fig. 4.2: **Block diagram of the experimental set-up for the energy scanning and gamma ray detection system.**

It must be noted that the energies of the gamma rays from the ^{60}Co and ^{137}Cs sources are between 0.662 MeV and 1.332 MeV, while the energy of the gamma rays from the nuclear reactions is 9.17 MeV for the ^{13}C(p,γ)^{14}N reaction and 10.76 MeV for the ^{27}Al(p,γ)^{28}Si reaction respectively. Thus, during the calibration an extrapolation to the energy regions under investigation was made. Care must be taken when extrapolating to much higher energy regions than the calibration

39

energies as an error of one channel in the energy position of the calibration source could result in an error of several channels in the energy of the gamma rays from the reaction.

The selection of the energy windows is done separately for each detector. For this, a linear gate is connected to the circuit (in the position indicated by broken lines in figure 4.2) so that an energy spectrum could be collected on the MCA. It must be noted that the connection between the single channel analyser (SCA) and the sum-invert amplifier is disconnected at this stage. With this connection, the signal will only pass through the linear gate to the MCA when the enable signal (from the SCA) is applied to the linear gate. An energy window can now be selected by adjusting the lower and upper energy discriminators on the SCA so that only signals with energies in the selected energy region are allowed to pass through the linear gate.

Once the energy window has been set, the linear gate is disconnected and the SCA is connected to the sum invert amplifier. The MCA is now set on multichannel scaler operation. The signals allowed through the SCA now pass through a sum-invert amplifier (which is a logic-or amplifier), so that whenever a signal is received from either of the two SCA's, a signal will appear at the output of the sum-invert amplifier. The function of this amplifier is to combine the signals from the two detectors, and the total counts of both detectors are now collected in one channel of the MCA. Because of the low count rate (~ 2 Hz counted at the MCA), the possibility of pile-up effect losses will be minimal at the sum-invert amplifier. Although the count rate at the main amplifier will be higher (amplifying the complete energy spectrum), the possibility of pile-up effect losses is still expected to be minimal.

During the nuclear reaction analysis, the incident proton energy is varied and the gamma ray yield is determined for each proton energy. The gamma ray yield for each energy step is recorded in subsequent channels of the MCA by an automatic energy scanning system (Amsel control). This energy scanning system (see section 4.4 for details) can be set to scan through a chosen energy region in equal

40

steps of a chosen energy difference. The energy scanning starts at the lower energy limit. If more than one sweep of the energy region is required, the system will automatically restart at the lower energy limit.

It is also important that for each energy step the counting should be done for the same number of incident protons on the target. For this purpose a current integrator in conjunction with a timer/counter is used. All the signals used in controlling the MCA, timer/counter and the Amsel control (bottom part of figure 4.2) are logic TTL (+5V) signals.

When the collection process is started, the Amsel control will set the incident proton energy to the lower energy limit of the sweep. When the energy is set, the Amsel control will give the start/restart signal and 5 μs later it will give the count signal (a diagram of the TTL signals is presented in figure 4.3). When the start/restart signal is received by the MCA, it moves the collection process to channel 0. The count signal will start the timer/counter, which is set to a predetermined quantity of charge. The counter in turn will give the interval signal that will step the collection process to channel 1 on the MCA. The interval signal will also open the linear gate on the MCA and the MCA will start the collection of signals from the sum invert amplifier. The linear gate on the MCA will only be open as long as the counter is active, that is when the interval signal (+5V) is present.

When the counter reaches the pre-set charge, it will stop and give the end of pre-set signal. This signal will reset the counter and at the same time the energy scanning system will, on receiving the end of pre-set signal, ramp to the next incident ion energy setting. When the counter stops, the interval signal will drop down to 0V, closing the linear gate on the MCA which in turn will stop the counting of the gamma ray signals into that particular channel. After the new incident proton beam ion energy is set by the Amsel control, it will give the count signal, starting the counter. The counter will set the interval signal high (+5V), which will step the MCA collection to the next channel and open the gate to start the collection process

into this channel. This is repeated until the energy scanning system reaches the upper energy limit of the sweep.
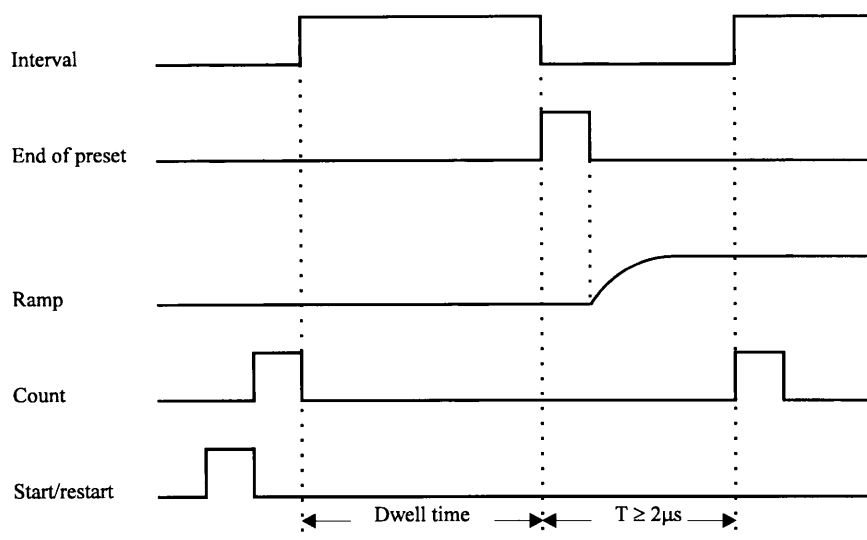
Fig. 4.3: **Diagram of the signals used in the control of the energy scanning system (Amsel control), the timer/counter and the MCA. All the signals are +5V (TTL) and are 5 μs long except for the interval signal where the length will be determined by the count speed and pre-set charge.**

4.4 THE AUTOMATIC ENERGY SCANNING SYSTEM

When nuclear reaction analyses with sharp resonances are performed, it is required that the energy of the incident beam be varied in small, precisely equal and constant steps in a reliable and reproducible way. As this is practically impossible with most available beam transport systems, various energy scanning systems have been devised to make these experiments easier [30-38]. For this investigation we have decided to employ an electrostatic energy scanning system designed by Amsel et al [39-41] and modified by Zinke-Allmang et al [42] for their experiments. The system was adapted for our accelerator by the Accelerator group of the National Accelerator Centre (NAC) at Faure.

42

In essence, the system comprises of two sets of electrostatic deflection plates, located before and after the analysing magnet, at similar (but not identical) distances from the magnet. If a voltage with opposite polarities is applied to both sets of electrostatic deflection plates, it will deflect the beam onto the energy stabilisation slits. This fools the energy-stabilisation feedback system into correcting the energy by changing the terminal voltage of the accelerator.

Figure 4.4 shows the layout of the accelerator, the beamline and the double-focusing switching magnet (which also acts as the analysing magnet), directing the particle beam along the right hand beam line. It can be seen from figure 4.4 that the entrance edge angle of the existing switching magnet is zero degrees while the exit edge angle of the magnet is 12.5°. As these edge angles are not the same, the system is not completely symmetrical about the plane through the centre of the magnet.
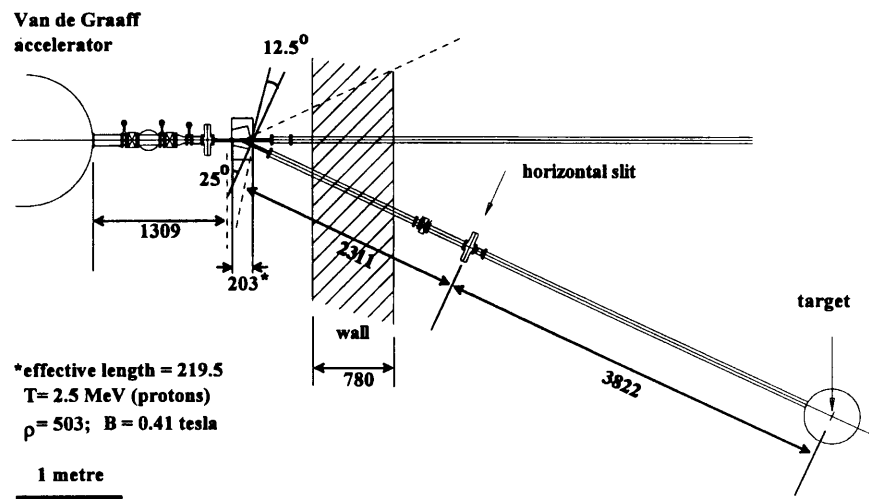
Fig. 4.4: Layout of the Van de Graaff beam line, showing the 25° right-hand beamline in which the energy scanning system is installed. Distances shown are in mm.

An analysis of the existing switching magnet, with deflection plates at distances D and D' before and after the magnet respectively, was performed by NAC after consultation with G. Amsel and E. d'Artemare. The results of the gain and linearity calculations are given in table 4.2.

43

Table 4.2: Design parameters of the energy scanning system for the existing analysing magnet geometry.

Parameter	Value
Radius of orbit in magnet, ρ_0	503.0 mm
Distance between first deflection plate & magnet, D	220.0 mm
Distance between magnet and second deflection plate, D'	210.0 mm
Length of deflection plates, l	360.0 mm
Separation of plates, ε	20.0 mm
Nominal voltage on each plate[*] for energy step of 50 keV	324.50 V
Gain, G_0	77.1 keV/kV
Non-linearity, p_1	-0.42
True voltage on each plate[*] for energy step of +50 keV	327.69 V
True voltage on each plate[*] for energy step of -50 keV	320.88 V

[*]One positive and one negative, on each set of plates.

For these parameters, the nominal gain of 77.1 implies that for an energy change (sweep) of 100 keV, a potential difference of ~1.3 kV will be required across both sets of plates. If one positive and one negative power supply is used, one on each side of the deflection plates, then a power supply voltage of only ±650 volts will be needed to still have the ~1.3 kV potential difference across the plates. Furthermore, if the power supplies are connected in series and their polarities are reversible, so that the energy sweep is carried out with deflections in both directions, with the left-hand plates of both sets connected to one power supply and the right-hand plates to another power supply, then a maximum supply voltage of only ±325 volts (nominal) would be necessary to permit the energy range of 100 keV to be covered. In our system a pair of precision bipolar 328-volt power supplies are used, giving ±656 volts across the plates. This allows for the 1% deviation from linearity, and thus an energy excursion of ±50 keV can be made, that is a total energy range of 100 keV.

44

4.5 THE $^{13}C(p,\gamma)^{14}N$ NUCLEAR REACTION

The depth profiles of the implanted $^{13}C^+$ ions were analysed by making use of the $^{13}C(p,\gamma)^{14}N$ nuclear reaction which has a resonance at an incident proton beam energy of 1.75 MeV. This resonance has a width of 75 eV [43-45] and a rather large cross section of approximately 340 mb. Figure 4.5 shows the decay scheme of the 9.17 MeV excited level in ^{14}N. The decay scheme together with the spin and parity assignments was obtained from the decay data of various authors [46-50]. The 9.17 MeV excited level in ^{14}N decays with a 79% probability directly to the ground state. Other important decay levels are the branches to the 6.44 MeV and 7.03 MeV excited states. The transition probability to the 6.44 MeV excited state is reported to be 10% [49], and that to the 7.03 MeV excited state to be 3% [45].
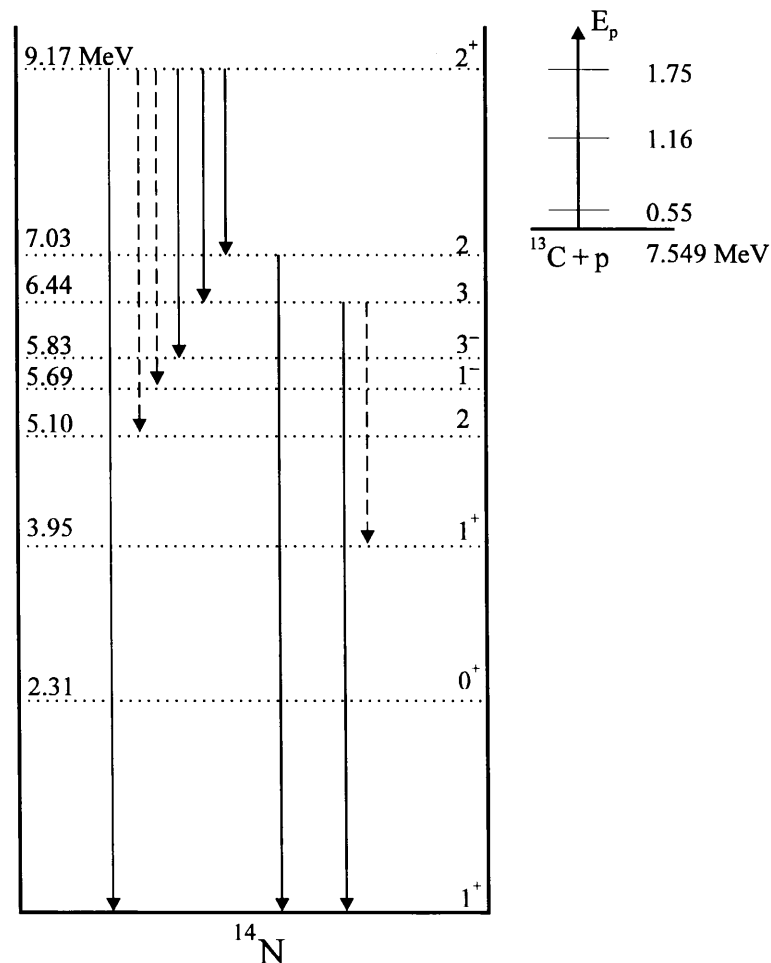
Fig. 4.5: The decay scheme of the 9.17 MeV excited level in ^{14}N. Broken arrows denote uncertain transitions.

45

If one applies the selection rules (discussed in section 3.1.2) on the 9.17 MeV to ground state transition it is clear, from values of the angular momentum of the two energy states with the same parity, that the transition ($3 \geq L \geq 1$) could be a magnetic dipole, electric quadrupole or magnetic octupole transition. Because of the multipole order, the predominant transition should be a magnetic dipole transition [51].

The high probability of the 9.17 MeV to ground state transition has the important advantage that the lower and upper energy discriminators of the γ-detector can be adjusted at relatively high energies where the background is low. However, the counting efficiency of the detector is rather poor at this energy. To optimise the signal to noise ratio, the energy window was set between 8.0 MeV and 9.3 MeV to detect the full energy peak together with its two escape peaks.

4.6 THE ^{27}Al(p,γ)^{28}Si NUCLEAR REACTION

The analysis of depth profiles resulting from ^{27}Al$^+$ implantations were performed by using the resonance of the ^{27}Al(p,γ)^{28}Si nuclear reaction at an incident proton beam energy of 0.992 MeV. Here the resonance has a width of 100 eV [52-54]. The decay scheme of the 12.542 MeV excited level in ^{28}Si together with spin and parity assignments of some of the energy levels as obtained from data of various authors [54-58] is represented in figure 4.6. The 12.542 MeV excited level in ^{28}Si decays with a probability of 78% [52] to the 1.78 MeV excited state. Other important decay levels in this reaction are the decay to the 7.8 MeV exited level (probability of 12%) and the decay to the 7.93 MeV excited level (probability of 5%)[52].

It can be seen from figure 4.6 that either the 10.76 MeV transition (12.54 MeV → 1.78 MeV) or the 1.78 MeV transition (1.78 → ground state) can be used for the detection of the gamma ray emitted from this reaction. We decided to use the former because the high energy of the gamma decay has the same

46

advantage, as the 9.17 MeV level decay in the $^{13}C(p,\gamma)^{14}N$ reaction, in that the energy discriminators are adjusted at relatively high energies where the background is low. The energy window for this reaction was set between 9.5 MeV and 11.0 MeV to again detect the full energy peak and its two escape peaks.

12.54 MeV .... 3^+

E_p 2.451

0.992

0.217

$^{27}Al+p$ 11.581 MeV

9.38 .... 2^+

7.93 .... 2^+

7.80 .... 3^+

6.88 .... 3^-

4.62 .... 4^+

1.78 .... 2^+

0^+
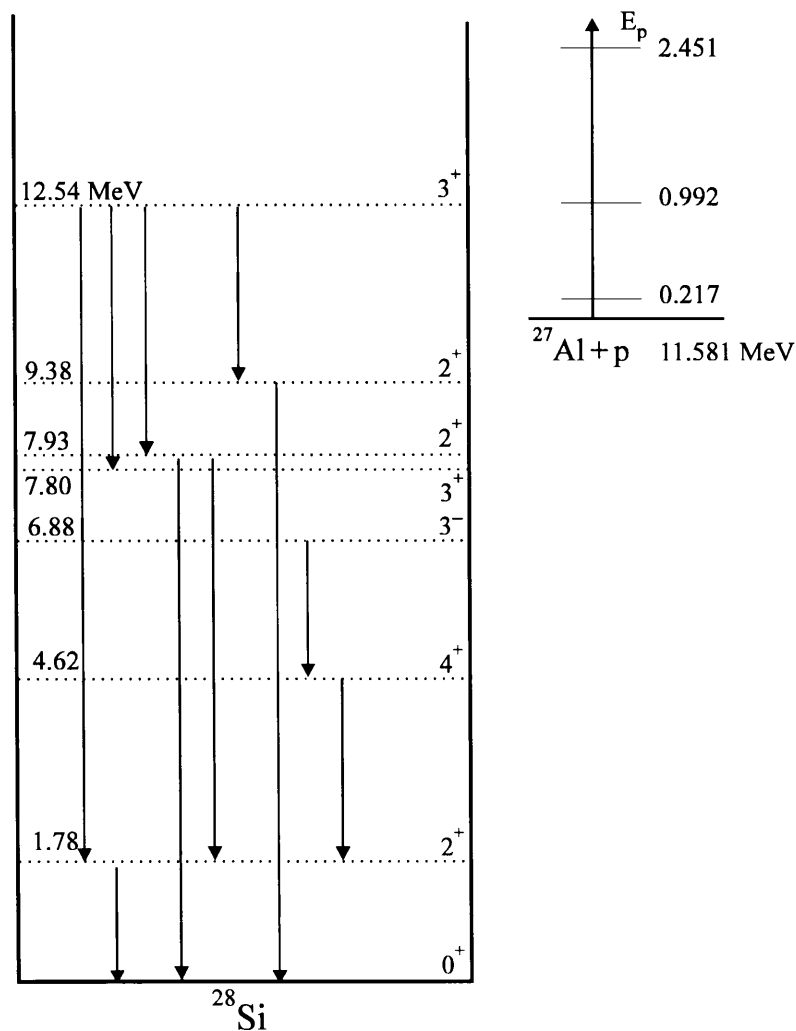
^{28}Si

Fig. 4.6: The decay scheme of some of the ^{28}Si transitions from the 12.542 MeV excited level.

It is clear from the selection rules of gamma decay in conjunction with the Weisskopf transition probability that this 10.76 MeV (12.54 MeV $\rightarrow$ 1.78 MeV) transition should be predominantly a magnetic dipole transition. It is reported [57]

47

that this transition is a mixture of magnetic dipole and electric quadrupole radiation with either 1% or 20% electric quadrupole radiation.

4.7   DATA ANALYSIS

Gamma ray yield curves from nuclear reactions were obtained by collecting a total charge of 6×10^{-4} coulomb for each step of the incident proton energy range under investigation. All the yield curves were stored on a computer, connected to the multi channel analyser, from where the depth profile analysis could be done. To determine the position of the surface, yield curves were measured for natural carbon targets [$^{13}C(p,\gamma)^{14}N$ reaction], which contain 1.1% ^{13}C, and single crystal aluminium targets [$^{27}Al(p,\gamma)^{28}Si$ reaction]. These targets were also used to determine the experimental energy resolution.

A computer program STOP was used to convert incident ion energies to depths. STOP uses the surface energy approximation and the stopping power values of Andersen and Ziegler [6], applying Bragg's rule for the gallium arsenide and stainless steel samples.

After correcting the experimental data for instrumental energy resolution and energy straggling, the range parameters of the implantation profiles were obtained by using the program VERD. This program calculates the four range moments according to definitions used in the version 91.41 of the TRIM code. The first two moments have the usual meaning of mean depth and standard deviation and are given by

$$R_1 = \frac{\sum (X_i Y_i)}{\sum Y_i}$$ 4.7.1

and

$$R_2{}^2 = \frac{\sum (X_i - R_1)^2 Y_i}{\sum Y_i} . \qquad\qquad 4.7.2$$

The third and fourth moments, which together with the second moment describe the shape of the implantation profile, are called skewness and kurtosis and are given by

$$R_3 = \frac{\sum (X_i - R_1)^3 Y_i}{\sum (Y_i)(R_2)^3} \qquad\qquad 4.7.3$$

and

$$R_4 = \frac{\sum (X_i - R_1)^4 Y_i}{\sum (Y_i)(R_2)^4} . \qquad\qquad 4.7.4$$

In the above equations, Y_i represent the number of implanted ions at depth X_i. The experimental results could now be compared with theoretical predictions obtained by computing approximately 10^5 ion trajectories, using the version 91.14 of the TRIM code.

For the calculations of the errors in the range parameters, X_i is taken as an independent variable with set values, while Y_i is taken as a dependent stochastic variable. It must however be noted that Y_i is independent of Y_{i-1} and only depends on the variable X_i. If a regression function μ is fitted to the experimental implantation profiles, the mean square deviation of Y_i from the expected values μ_i for a given X_i is given by $\sigma^2_{y|x}$. The expected values μ_i now has a functional dependence on the values X_i of the independent variable X. This functional relationship was expressed as

$$\mu_i = \mu(x_i) = b_0 + b_1 X_i + b_2 X_i^2 + b_3 X_i^3 + b_4 X_i^4 + b_5 X_i^5 + b_6 \log(X_i) .$$

49

To be able to calculate the error in the range moments it was necessary to eliminate the stochastic variable from equation 4.7.1. The assumption was thus made that

$$R_1 = \frac{\sum (X_i Y_i)}{\sum Y_i} = \frac{\sum X_i Y_i}{n\overline{\mu}}$$

$$R_2^{\,2} = \frac{\sum (X_i - R_1)^2 Y_i}{n\overline{\mu}}$$

$$R_3 = \frac{\sum (X_i - R_1)^3 Y_i}{n\overline{\mu}(R_2)^3}$$

$$R_4 = \frac{\sum (X_i - R_1)^4 Y_i}{n\overline{\mu}(R_2)^4}$$

where

$$\overline{\mu} = \frac{1}{n}\sum \mu_i$$

and n is the number of data points. The errors in the range moments can now be expressed as asymptotic expressions of the mean square deviation of the range moments and are given by [59]

$$\mathrm{var}(R_1) = \frac{\sum X_i^2}{n^2\overline{\mu}^2}\sigma_{y|x}^2$$

$$\mathrm{var}(R_2^{\,2}) = \frac{1}{n^2\overline{\mu}^2}\sum (X_i - R_1)^4 \sigma_{y|x}^2$$

$$\mathrm{var}(R_3) = \frac{1}{n^2\overline{\mu}^2(R_2)^6}\sum (X_i - R_1)^6 \sigma_{y|x}^2$$

$$\mathrm{var}(R_4) = \frac{1}{n^2\overline{\mu}^2(R_2)^8}\sum (X_i - R_1)^8 \sigma_{y|x}^2 \,.$$

50

CHAPTER 5

REVIEW OF PREVIOUS RESULTS

Since early 1960 when Davies et al [60, 61] performed the pioneering measurements, a great deal of work has been published on ranges of heavy ions after low energy implantation in solids [62-70]. Range parameters are of considerable theoretical interest and of importance for many applications in metallurgy and microelectronics. In this chapter, some of the published range parameters are discussed and compared to the theoretical predictions obtained with the TRIM 91.14 code.

5.1 HEAVY ION IMPLANTATIONS

Although experimental results generally compare reasonably well with theoretical predictions (developed by various authors [2, 19, 71-76]), significant discrepancies between theory and experiment have been reported for a variety of medium to heavy ions implanted into light mass targets. For consistency, all experimental results must be compared to the same theoretical model. With our investigation we wanted to compare the experimental results with the theoretical predictions of the TRIM 91.14 code. It was therefore necessary to compare some of the reported experimental results with the TRIM 91.14 predictions.

Fichtner et al [77] used Rutherford backscattering (RBS) to obtain the depth profiles for SiC films implanted with Pb and Au at energies between 20 keV and 250 keV. These authors made corrections for energy straggling as well as for system energy resolution when the data analysis was performed. The experimental results of Fichtner together with TRIM 91.14 predictions are presented in table 5.1.

51

Table 5.1: Experimentally determined projected ranges (R_p) and straggling width (ΔR_p) parameters (in Å) of Pb and Au implantations in SiC films [77]. Also shown are the predictions of the TRIM 91.14 code (shaded part of table).

Ion	Energy keV	Exp. R_p	Exp. ΔR_p	TRIM 91.14 R_p	TRIM 91.14 ΔR_p
Pb	20	155	25	157	29
	30	170	40	197	37
	50	240	55	266	50
	70	280	65	327	63
	100	360	75	411	79
	250	700	145	771	150
Au	20	150	30	159	30
	30	175	40	200	39
	50	240	50	271	53
	70	290	70	334	67
	100	390	80	421	85
	250	710	150	789	161

Fichtner found that the experimental projected ranges and straggling values [77] significantly exceed the TRIM 90 predictions [19]. These deviations were found to be energy independent in this energy range. By using a model developed by Grande et al [78] (a modified version of TRIM which include inelastic effects in the nuclear stopping regime), these authors were able to get remarkably good agreement between the experimental and calculated data. On the other hand, the projected range values from these authors were found to be on average 9% lower than the theoretical predictions of the TRIM 91.14 code while the straggling values agreed quite well.

Grande at al [79] investigated implantations of Bi, Pb, Au, Yb, Er and Eu into carbon films. The depth profiles were obtained with RBS and corrections for energy straggling and system energy resolution were made during the data analysis. The experimental results of Grande together with the TRIM 91.14 predictions are presented in table 5.2.

Table 5.2: Experimental range parameters (in Å) of ions implanted into carbon films [79] and compared with the TRIM 91.14 theoretical predictions (shaded part of table).

Ion	Energy keV	Exp. R_p	Exp. ΔR_p	TRIM 91.14 R_p	TRIM 91.14 ΔR_p
Bi	15	140	27	108	13
	40	245	37	191	25
	80	390	60	295	40
	150	615	115	449	61
Pb	10	138	32	85	10
	20	205	44	125	16
	30	230	46	159	21
	40	250	54	189	25
	50	315	60	216	28
	80	390	83	291	39
	100	495	91	337	45
	150	660	120	443	60
	200	790	137	542	74
Au	15	170	20	110	14
	20	197	25	129	17
	30	220	34	164	22
	50	315	47	224	31
	70	395	56	277	39
	100	460	80	350	50
	150	640	121	463	66
Yb	15	140	27	113	16
	20	176	35	133	19
	30	207	41	170	25
	50	295	59	233	35
	70	370	75	290	44
	100	490	95	370	57
	200	800	150	610	94
Er	10	135	48	87	12
	50	310	90	229	35
	75	421	95	299	46
	100	500	105	365	57
Eu	10	120	33	93	14
	30	220	45	178	28
	50	302	64	247	41
	70	350	71	310	51
	100	458	90	398	67
	200	729	140	669	112

Grande found that the experimental projected ranges [79] were significantly higher than the TRIM 87 predictions. The differences were approximately independent of the implantation energy and as high as 40% for Bi, Pb and Au and around 30% for Yb, Er and Eu. The experimental range straggling values were also higher than the TRIM 87 predictions, the difference as high as 100% for Pb and between 30% and

50% for the other ions. The predicted projected ranges and straggling values obtained with the TRIM 91.14 code did not differ significantly from that obtained with the TRIM 87 code.

Grande et al [78] also investigated Cs, Xe, Sn, Rb, Kr, Ga and Cu implantations into carbon films. They again used the RBS technique and the same corrections were made during the data analysis. The experimental results of these authors and the TRIM 91.14 predictions are presented in table 5.3.

Table 5.3: Experimental range parameters (in Å) of ions implanted into carbon films [78], compared with the TRIM 91.14 theoretical predictions (shaded part of table).

Ion	Energy keV	Exp. R_p	Exp. ΔR_p	TRIM 91 R_p	TRIM 91 ΔR_p	Ion	Energy keV	Exp. R_p	Exp. ΔR_p	TRIM 91 R_p	TRIM 91 ΔR_p
Cs	15	150	39	123	21	Kr	15	125	40	126	28
	20	170	43	146	25		30	206	60	204	46
	30	250	54	189	33		50	320	90	299	68
	50	290	69	265	48		70	440	125	392	88
	100	490	105	436	80		100	610	155	526	118
	200	820	152	751	138		150	870	220	749	165
Xe	20	150	30	120	19	Ga	20	216	52	160	39
	50	290	60	217	36		50	415	110	325	80
	100	480	100	354	58		100	730	200	588	142
	300	1200	230	824	129		200	1500	340	1120	256
							300	2000	500	1672	363
Sn	30	235	45	190	36	Cu	30	280	90	224	57
	50	310	65	270	51		50	430	130	337	86
	70	390	80	344	66		70	570	160	450	113
	100	515	100	450	87		100	785	215	618	153
	300	1300	260	1123	214		150	1180	320	904	218
							200	1547	400	1192	277
Rb	10	104	40	97	21						
	30	210	70	204	46						
	50	330	90	298	67						
	80	500	145	433	98						
	100	590	160	522	117						
	150	850	215	744	165						
	200	1077	270	965	209						

For this investigation, the authors found that there were significant discrepancies between experimental ranges [78] and TRIM 89 predictions. For the projected ranges

the deviations were as high as 30% for the Xe, Sn, Ga and Cu implantations. On the other hand, the situation is quite different for Cs, Rb and Kr implantations where the difference between the experimental projected ranges and the TRIM 89 predicted values were around 10% or less. The difference in the straggling values was however still between 30% and 50%. The predicted projected ranges and straggling values obtained with the TRIM 91.14 code did not differ significantly from those obtained using the TRIM 89 code.

Using the same experimental technique, Grande et al [78] also investigated Pb, Bi, Au, Yb, Cs and Rb implantations into boron films. These experimental results together with the TRIM 91.14 predictions are presented in table 5.4.

Table 5.4: Experimental range parameters (in Å) of ions implanted into boron films [78], compared with the TRIM 91.14 theoretical predictions (shaded part of table).

Ion	Energy keV	Exp.		TRIM 91.14	
		R_p	ΔR_p	R_p	ΔR_p
Pb	20	175	30	151	19
	50	310	70	254	34
	100	450	100	393	53
	300	1050	200	846	116
Bi	20	180	30	152	19
	50	285	60	255	34
	100	440	90	395	54
	300	1050	170	851	117
Au	20	200	50	151	20
	50	330	70	257	35
	100	470	90	401	56
	300	1100	172	876	124
Yb	20	180	40	151	21
	50	310	60	262	39
	100	480	90	414	63
	300	1100	190	937	142
Cs	20	165	45	155	26
	50	285	65	282	50
	100	450	110	464	84
	300	1180	262	1145	204
Rb	20	170	45	161	35
	50	325	80	317	70
	100	565	150	559	124
	300	1550	320	1536	314

Grande found that for the Pb, Bi, Au and Yb implantations, the TRIM 89 predicted projected range values were systematically lower than the experimental values [78]. The difference was on average 25% and found to be almost energy independent. The experimental straggling values exceeded the predicted values by almost 100%. The situation was different for Cs and Rb where the agreement between the experimental and theoretically predicted values was better than 10%. The predicted straggling values in this case were still smaller than the experimental values. Again there was not a significant difference between the predicted range parameters obtained with the TRIM 91.14 and TRIM 89 codes except for the Cs implantations into C films at 100 keV and 200 keV where the TRIM 91.14 straggling predictions were about 4% higher than those of the TRIM 89 predictions.

5.2 IONS IMPLANTED INTO SILICON

Fichtner et al [80] investigated the implantation of several elements ($29 \leq Z_1 \leq 83$) into amorphous silicon. The depth profiles were obtained by Rutherford backscattering analysis using 760 keV alpha particles ($^4He^{2+}$). Projected ranges were determined using the surface approximation while straggling values were evaluated after correcting for energy straggling and system energy resolution. The experimental results together with the theoretical predictions of TRIM 91.14 for implantation energies below 70 keV are presented in table 5.5, while those for implantation energies between 100 keV and 390 keV are presented in table 5.6.

56

Ions	Energy (keV)													
	10	10	15	15	20	20	30	30	40	40	50	50	70	70
Cu	168	130	170	171	225	211	276	286	356	358	444	430	560	571
	57	49	63	65	95	80	127	108	152	135	180	160	237	210
Ga	115	127	160	168	194	205	267	277			401	412	531	544
	45	47	57	62	71	76	98	101			150	150	190	195
Br	120	124			183	196	251	261	315	323	355	382	445	500
	40	43			65	68	85	91	110	112	130	132	165	172
Rb	108	123	140	159	172	193	256	256			325	373	502	487
	37	41	46	53	54	65	74	87			118	127	170	164
Pd	115	120			181	183	240	239			332	341	435	436
	31	36			46	56	68	74			108	106	140	135
Sn	105	121			150	183	210	236			285	333		
		34			47	52	60	69			85	98		
Cs	85	122			137	182	188	234			270	326		
		32			50	49	67	64			84	91		
Eu	144	120	177	150	194	177	247	226	286	270	318	311	395	388
		29	23	37	29	44	46	57	63	69	68	80	91	101
Yb	158	121			200	176	235	221	270	263	310	303	380	374
	30	27			43	40	51	52	64	62	84	72	92	90
Au			210	150	250	175					375	297	428	365
			50	31	52	37					84	66	103	82
Bi	110	123			160	176	198	219	245	258	270	295		
	42	24			50	36	60	46	69	55	75	63		

Fichtner found that the experimental results compared quite well with TRIM 85 predictions [19]. However, for Au, Eu and Yb they found significant deviations from the predicted values for implantation energies below 70 keV. A comparison of these results with the predictions of TRIM 91.14 shows that the results for implantation energies below 70 keV compare, as in the case with the TRIM 85 predictions, reasonably well (±10%). The only significant deviations in this case was found for Au, Sn and Cs implantations, while the 10 keV implantations for both Cu and Yb were also found to be outside the error of ±10% (experimental results larger than the TRIM 91.14 predictions). With the exception of Eu, Yb and Au, most of the experimental results were lower than the TRIM 91.14 predictions.

Table 5.6: Measured (unshaded part of table) projected ranges and straggling values (given below the ranges) of $29 \leq Z_1 \leq 83$ ions implanted into amorphous silicon with energies between 100 keV and 390 keV [80]. The results in the shaded part of the table are those calculated with the TRIM 91.14 code. Both the projected range and straggling values are in Å.

Ions	Energy (keV)											
	100		150		200		300		350		380	
Cu	793	780	1235	1137								
	294	281	487	393								
Ga	705	740	1033	1070	1373	1400			2580	2422		
	260	260		365		466				745		
Br	600	673	1122	962								
	255	229		318								
Rb	650	651			1310	1199						
	230	217			425	385						
Pd	550	573			1020	1017			1725	1682		
	185	178			315	310			500	497		
Sn	525	554			945	967					1725	1702
	155	164			267	283					550	482
Cs	445	534			785	917					1485	1589
	140	150			230	258					415	438
Eu	496	497			855	832	1180	1152			1420	1402
	115	130			202	218	296	299			350	363
Yb	468	475			796	778	1110	1061				
	126	116			220	189	280	257				
Au	484	458			782[a]	710	1100[b]	967			1366[c]	1215
	130	104			198	163	290	222			335	276
Bi	425	452	570[d]	577							1245	1153
	115	99	150	128							310	255

[a] Energy = 190 keV, [b] Energy = 290 keV, [c] Energy = 390 keV and [d] Energy = 145 keV.

For implantation energies between 100 keV and 390 keV, the comparison between the experimental results [77] and the theoretical predictions (TRIM 91.14) were within 10%, except for the Cs implantations where disagreements >10% were found.

Chu et al [81] investigated the implantation of Sb into silicon. The depth profiles were measured by secondary ion mass spectroscopy (SIMS) and the projected range, standard deviation (range straggling) and skewness of the distribution is obtained from the SIMS profiles. These experimental range distributions parameters together with the theoretical predictions of TRIM 91.14 are presented in table 5.7.

Table 5.7: Range distribution parameters (in Å) determined experimentally [81] as well as theoretically (TRIM 91.14) for Sb implantations into Si. The shaded part of the table displays the TRIM 91.14 predictions.

Energy keV	Experimental			TRIM 91.14		
	R_p	ΔR_p	Skewness	R_p	ΔR_p	Skewness
5	91	47	0.77	82	22	0.49
10	117	54	0.70	120	34	0.51
20	170	67	0.46	182	52	0.48
30	226	86	0.79	235	68	0.47
40	246	95	0.59	284	83	0.46
50	307	107	0.52	332	97	0.43
60	351	110	0.25	376	110	0.44

These authors compared their experimental distributions of implanted Sb into silicon with that obtained from three versions of the LSS theory [76, 82, 83]. They concluded that their results only agreed with the modified LSS theory proposed by Wilson et al [82] while their experimental measurements were much larger than those from LSS calculations proposed by Gibbons et al [76] and Winterbon [83]. The experimentally obtained range distribution parameters compare reasonably well with the predictions of the TRIM 91.14 code. The slightly higher straggling values might be due to ion beam mixing, which is expected during a SIMS measurement. The experimental projected ranges on the other hand, with the exception of the 5 keV implantation, were slightly smaller (~7%) than those predicted by the TRIM 91.14 code. This might be a result of the uncertainty in the sputtering rate through the implanted region and thus in the determination of the depth scale.

An investigation of implantation profiles of group III and group IV ions in amorphous silicon were performed by Crowder [84]. The depth profiles of the ^{11}B, ^{27}Al, ^{32}P, ^{121}Sb and ^{209}Bi ions were obtained by electrical evaluation of the implanted layer with the Hall effect and sheet resistivity measurements in conjunction with layer removal techniques. The depth profiles of the ^{31}P, ^{75}As, ^{123}Sb and ^{71}Ga ions were obtained using neutron activation analysis in conjunction with layer removal techniques. The experimental results and the theoretical predictions of the TRIM 91.14 code are represented in table 5.8.

Table 5.8: A comparison of range parameters (in Å) observed in amorphous silicon (after implantation with various group III and IV ions) [84] with TRIM 91.14 theoretical predictions.

Ion	Energy keV	Exp. R_p	Exp. ΔR_p	TRIM 91.14 R_p	TRIM 91.14 ΔR_p
B	60	2300	700	2123	519
	120	4000	1000	3980	871
Al	200	2600	800	3290	968
^{31}P	100	1200	480	1287	439
	140	1800	700	1807	567
	200	2800	740	2560	743
	280	3800	910	3577	934
^{32}P	120	1600	600	1543	501
Ga	140	900	350	1004	341
	280	1750	700	1941	613
As	80	600	250	586	205
	140	950	400	958	325
	280	1800	700	1836	581
^{121}Sb	120	600	160	631	187
^{123}Sb	260	1050	300	1198	344
Bi	240	800	200	821	182

Crowder demonstrated that the LSS theory does provide a reasonable estimate for the projected range. However, for the observed distribution widths the calculations of Johnson and Gibbons [85] erroneously predicted values that were too small for heavy ions. The experimental projected range and straggling width values of Crowder agree, with the exception of those obtained for the Al implantation, well with those predicted by the TRIM 91.14 code. The difference between the projected range values is mostly less than 10%, while there is reasonable agreement between the straggling widths.

For Ga ions implanted into silicon, the experimental projected ranges of Crowder [84] are ~10% lower and the experimental projected ranges of Fichtner [80] (with the exception of the 350 keV implantation which is ~7% higher) are ~4% lower than those predicted by TRIM 91.14. On the other hand, for Bi implantations into silicon, the experimental projected ranges of Crowder [84] are ~3% lower, and those of Fichtner [80] are ~7% lower, than the TRIM 91.14 predictions. The projected range of the 380 keV implantation of Fichtner [80] is ~8% higher than the TRIM 91.14

60

prediction and was excluded from the calculation of the average projected range of Fichtner [80].

When comparing the experimental projected ranges for Sb implantations into silicon with the TRIM 91.14 predictions, those of Crowder [84] are found to be ~10% lower and those of Chu et al [81] (with the exception of the 5 keV implantation which is ~11% higher) are ~8% lower.

Ranges of ^{13}C, ^{15}N and ^{27}Al ions in silicon are reported by Paltemaa et al [86] for implantation energies between 20 and 100 keV. The depth profiles were obtained using (p,γ) resonant nuclear reaction analysis (NRA) methods. During the data analysis corrections were made for energy straggling and system energy resolution. The experimentally determined projected ranges and the TRIM 91.14 predictions are presented in table 5.9.

Table 5.9: Projected ranges (in Å) of ^{13}C, ^{15}N and ^{27}Al implanted into Si [86] compared with those obtained from TRIM 91.14 predictions (shaded part).

Ion	Energy keV	Exp. R_p	TRIM 91 R_p
^{13}C	20	639	610
	40	1215	1169
	60	1768	1709
	80	2330	2230
	100	2807	2737
^{15}N	20	541	522
	40	1043	994
	60	1558	1453
	80	2051	1894
	100	2536	2330
^{27}Al	20	330	344
	40	652	653
	80	1262	1290
	100	1562	1616

The authors experimentally observed smaller ranges than theoretically predicted by the LSS theory [2, 82, 87, 88] and Monte Carlo calculations with a universal potential

calculated using Dirac-Fock electron distributions [89-91]. These authors found that the agreement between experimental and theoretical projected range values gets worse with increasing implantation energy. When comparing the experimental projected ranges with the theoretical predictions using the TRIM 91.14 code, the experimental values were found to be ~4% higher for the ^{13}C implantations, ~6% higher for the ^{15}N implantations and ~ 3% lower for the ^{27}Al implantations. The agreement between the experimental projected ranges [86] and TRIM 91.14 predictions for the ^{27}Al implantations is much better than observed by Crowder [84] where the experimental value is ~21% lower than the TRIM 91.14 prediction.

5.3 LIGHT ION IMPLANTATIONS

Relatively few results of range parameters for light ion implantations are found in the literature. Ranges of ^{13}C, ^{15}N, ^{27}Al and ^{24}Mg ions in germanium are also reported by Paltemaa et al [86] for implantation energies between 20 and 100 keV. Depth profiles were obtained in the same way (NRA) as for the implantations into silicon, and similar corrections were made during the data analysis. Experimentally obtained projected range and TRIM 91.14 predictions are presented in table 5.10.

Table 5.10: **Projected ranges (in Å) of ^{13}C, ^{15}N, ^{24}Mg and ^{27}Al ions implanted into Ge [86] compared with that obtained by TRIM 91.14 predictions (shaded part of the table).**

Ion	Energy keV	Exp. R_p	TRIM 91 R_p	Ion	Energy keV	Exp. R_p	TRIM 91 R_p
^{13}C	20	469	434	^{24}Mg	20	263	268
	40	865	811		40	489	495
	60	1297	1180		60	733	727
	80	1767	1543		80	996	961
	100	2130	1909		100	1278	1199
^{15}N	20	414	373	^{27}Al	20	226	248
	40	733	694		40	432	456
	60	1128	1010		60	639	664
	80	1485	1319		80	789	876
	100	1805	1625		100	1015	1091

These authors reported reasonable agreement between the experimental and theoretical ranges (LSS theory [2, 82, 87, 88] and Monte Carlo calculations [89-91]) for the germanium targets. For ^{13}C in germanium these authors reported better agreement between experimental and theoretical (LSS and Monte Carlo) projected range values for higher implantation energies. This is the opposite of that reported by these authors for ^{13}C in silicon (see section 5.2).

Although the agreement between the experimental ranges and that predicted by TRIM 91.14 was not as excellent as for the silicon substrates, the discrepancy was still better than 15%. When comparing the experimental projected ranges with the theoretical predictions using the TRIM 91.14 code, the experimental values were on average found to be ~10% higher for the ^{13}C implantations, ~11% higher for the ^{15}N implantations and ~7% lower for the ^{27}Al implantations. For ^{24}Mg, the experimental projected range at low implantation energies (20 keV and 40 keV) is lower than the theoretical predictions. From implantation energies higher than 60 keV, the experimental projected ranges are higher than the TRIM 91.14 predictions. All the ^{24}Mg experimental projected ranges (except the 100 keV implantation) are, however, in agreement with the TRIM 91.14 predictions.

Range determinations of ^{15}N ions implanted in ten metals (Al, Ti, Ni, Cu, Zn, Mo, Ag, Ta, W and Au) were performed by Luomajärvi et al [92]. These authors obtained depth profiles using resonant NRA and made corrections during the data analysis for energy straggling, the energy distribution of the proton beam and the natural width of the resonance. Experimental ranges and TRIM 91.14 predictions of ^{15}N implantations into the ten metals are presented in table 5.11.

63

Table 5.11: Projected ranges (in Å) of ^{15}N ions implanted into ten metals [92] compared with the TRIM 91.14 predictions (shaded part of table).

Metal	Energy keV	Exp. R_p	TRIM R_p	Metal	Energy keV	Exp. R_p	TRIM R_p
Al	20	537	508	Mo	20	333	260
	40	1037	964		40	520	475
	60	1481	1402		60	725	671
	80	1963	1808		80	922	866
	100	2333	2205		100	1127	1062
Ti	20	390	393	Ag	20	371	272
	40	733	735		40	600	484
	60	1044	1066		60	800	695
	80	1378	1384		80	1000	892
	100	1667	1692		100	1171	1085
Ni	20	281	233	Ta	20	289	246
	40	506	439		40	482	427
	60	685	640		60	675	600
	80	921	849		80	837	762
	100	1101	1045		100	1000	927
Cu	20	324	253	W	20	290	213
	40	569	480		40	472	366
	60	792	709		60	663	516
	80	982	934		80	803	656
	100	1161	1161		100	938	796
Zn	20	322	232	Au	20	306	231
	40	644	611		40	497	396
	60	938	902		60	674	551
	80	1246	1191		80	865	704
	100	1541	1475		100	1052	857

These authors observed that in almost all cases, except Ti and the 100 keV Al implantation, the experimental ranges in the polycrystalline targets were more than 20% larger than those predicted by the LSS theory [2] using amorphous material assumptions. These experimental ranges were also, with the exception of Ti, found to be larger than those theoretically predicted by TRIM 91.14. The agreement between the experimental values and the TRIM 91.14 predictions for the Ti implantation is however excellent. A relatively large difference between experimental and theoretical values is observed for the 20 keV implantations into heavy metals. This discrepancy again improved (as in the work of Paltemaa et al [86]) with increasing implantation energy. There is, however, still a serious discrepancy between the experimental and theoretical values for the implantations into W and Au.

64

Keinonen et al [93] investigated the ranges of $^{27}\text{Al}^+$ ions in nine metals, which were almost the same metals Luomajärvi et al [92] investigated. Depth profiles were obtained using resonant NRA and corrections were made during the data analysis for energy straggling, the proton beam energy width and the natural width of the resonance. The experimental ranges together with the TRIM 91.14 predicted range values are presented in table 5.12.

Table 5.12: **Projected ranges (in Å) of ^{27}Al ions implanted into Ti, Ni, Cu, Mo, Ag, Ta, W, Au and Pb [93] compared with the TRIM 91.14 predictions (shaded part of table).**

Metal	Energy keV	Exp. R_p	TRIM R_p	Metal	Energy keV	Exp. R_p	TRIM R_p
Ti	20	233	245	Ta	20	181	158
	40	464	462		40	337	273
	60	687	680		60	470	384
	80	844	902		80	608	494
	100	1044	1127		100	711	604
Ni	20	180	138	W	20	202	137
	40	326	260		40	337	236
	60	461	382		60	466	332
	80	596	508		80	606	427
	100	674	636		100	679	519
Cu	20	179	148	Au	20	192	147
	40	335	281		40	316	253
	60	469	414		60	482	354
	80	636	549		80	580	452
	100	770	693		100	658	553
Mo	20	222	161	Pb	20	316	248
	40	412	292		40	588	422
	60	559	423		60	825	588
	80	716	552		80	1000	744
	100	843	684		100	1105	899
Ag	20	257	169				
	40	429	304				
	60	581	434				
	80	724	568				
	100	826	704				

The experimental ranges of Keinonen et al [93] were in all cases found to be larger, even up to 70%, than the theoretical values obtained from the LSS theory [2] using amorphous material assumptions. Although there were still rather large discrepancies

65

when these experimental ranges were compared to TRIM 91.14 predicted range values, there was at least a 25% improvement in these discrepancies (compared to the discrepancies between experimental and LSS theoretical values). With the exception of Ti, the experimental projected ranges of all cases were found to be larger (up to ~41%) than those predicted by the TRIM 91.14 code.

With only a few exceptions, reasonable agreement was found when the experimental range parameters of medium to heavy ion implantations into light mass targets are compared with the TRIM 91.14 predictions. This agreement was found to be the same or better than that obtained by the authors of the published results when they compared experimental range parameters with other theoretical predictions. For light ion implantations, the agreement between experimental and TRIM 91.14 predicted range parameters was found to be reasonable to excellent. For implantations into Si and Ge, the agreement was good while there was (with the exception of Ti) still a discrepancy for the implantations into metals. There was however, with a few exceptions, a marked improvement in the agreement between experimental and TRIM 91.14 predicted range parameters compared to the agreement between the experimental and other theoretical values. When the experimental range parameters were found to be larger (or lower) than the published theoretical values, they were normally also larger (or lower) than the TRIM 91.14 predicted values, but by a smaller margin.

The average difference between the experimental and TRIM 91.14 predicted projected ranges, for all the energy ranges and ion-target combinations investigated here, is about 12%. It must be noted that there is, in almost all ion-target combinations, an improvement in this discrepancy with increasing ion energy. It was therefore concluded that the TRIM 91.14 code gave acceptable agreement with experiment and hence to use it for a comparison of the experimental range parameters obtained in this study.

66

CHAPTER 6

RESULTS AND DISCUSSION

Experimental depth distributions of 150 keV $^{13}C^+$ and $^{27}Al^+$ ions implanted into silicon, gallium arsenide, magnesium and stainless steel are presented for implantations at room temperature, as well as for implantations at liquid nitrogen temperature. Some of the silicon samples were pre-implanted with 300 keV $^{20}Ne^{++}$ ions to amorphize the surface region, thus eliminating the effect of channelling. The distribution parameters obtained are discussed and compared to theoretical predictions obtained from the TRIM 91.14 code.

6.1 RESULTS FOR CARBON IMPLANTATION PROFILES USING THE $^{13}C(p,\gamma)^{14}N$ REACTION.

It must be noted that the nuclear reaction analysis measurements at the University of Pretoria (UP) and at the Max-Planck-Institut für Kernphysik (MPI) were performed on the same samples. Before it was possible to analyse any of the $^{13}C^+$ implanted samples it was necessary to obtain the position of the substrate surface. This was accomplished by measuring yield curves for natural carbon (which contains 1.1% ^{13}C). The channel number corresponding to the surface position could now be coupled to the known resonance energy of the $^{13}C(p,\gamma)^{14}N$ reaction. The yield curve obtained from natural carbon is illustrated in figure 6.1. The error bars indicate standard deviations calculated from the total number of counts per channel.

67
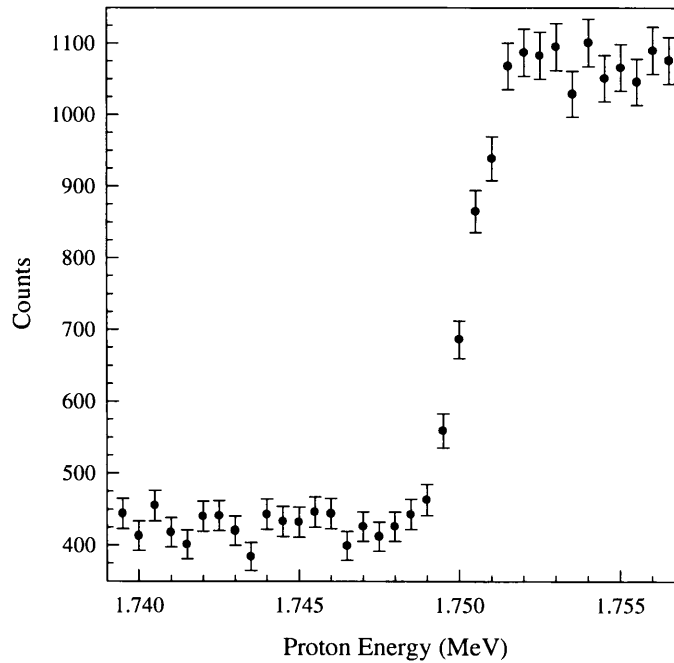
Fig. 6.1: **Yield curve from natural carbon using the ^{13}C(p,γ)^{14}N nuclear reaction to determine the surface position of the ^{13}C implanted samples.**

This yield curve was also used to determine the energy resolution of the experimental set-up. It can be seen from figure 6.1 that there are four channels between 10% and 90% peak height. As each of these channels corresponds to an energy difference of 0.5 keV, the instrumental energy resolution is found to be 2 keV.

Straggling is important for proton beams, as it is large at the relevant depths compared to the relatively small energy losses. This is evident from figure 6.2, which gives the depth resolution of the ^{13}C(p,γ)^{14}N reaction analysis as a function of the depth. The depth resolution is given by a quadratic summation of the instrumental energy resolution and the energy straggling of the analysing beam. It must, however, be kept in mind that this is only valid while both contributions are given by normal distributions. For this investigation the assumption is correct as both the instrumental energy resolution (dominated by the energy spread of the proton beam) and the energy straggling (Bohr estimate) will be given by normal distributions.
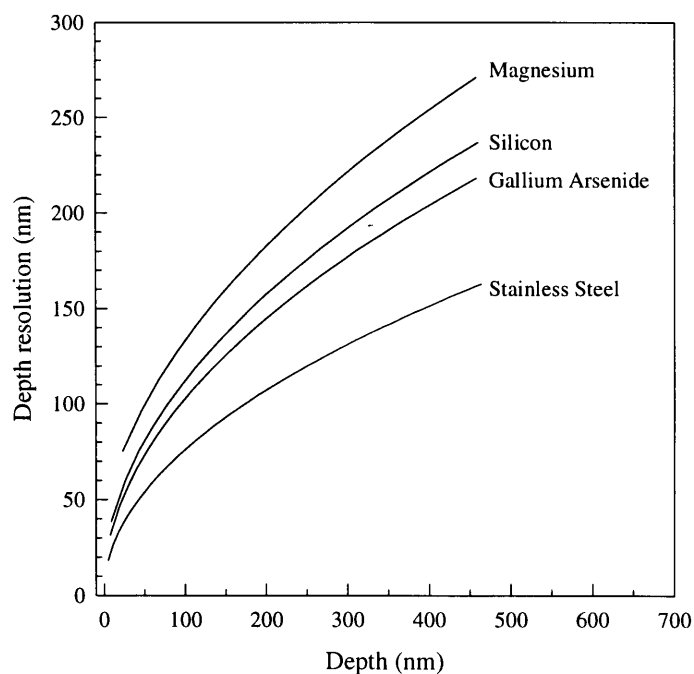
Fig. 6.2: Depth resolution (FWHM) of the $^{13}C(p,\gamma)^{14}N$ reaction in silicon, gallium arsenide, magnesium and stainless steel as a function of depth. A proton energy spread of 2 keV was taken into account when determining the depth resolution.

The Bohr straggling could be determined as a function of the depth t by using equation 2.4.2. At the ^{13}C peak position (depth of 365 nm in silicon) the energy straggling could be calculated (using equation 2.4.5) and it was found to be 3.63 keV. It must be noted that this is not a constant value, but is also a function of the depth t, and will therefore have to be determined for every depth. The energy resolution at the depth of 365 nm (given by the quadratic summation of the instrumental energy resolution and the energy straggling) was determined to be 6.38 keV. This could then be converted to a depth scale using the stopping power values of Andersen and Ziegler [6], and it was found to be 222 nm. In these calculations it was assumed that energy straggling is adequately described by the Bohr estimate, which should be valid in this energy range.

Figure 6.3 illustrates typical yield curves for implanted and unimplanted samples as a function of proton energy. The slightly higher background of the implanted sample (compared to the unimplanted sample) is the result of a large number of

69

weakly populated and overlapping states in the vicinity of the 9.17 MeV level of the ^{14}N compound nucleus. The slight energy dependence of this contribution is taken into account by adding a linear energy term to the fit equation used for the background correction during the analysis of the implanted samples.
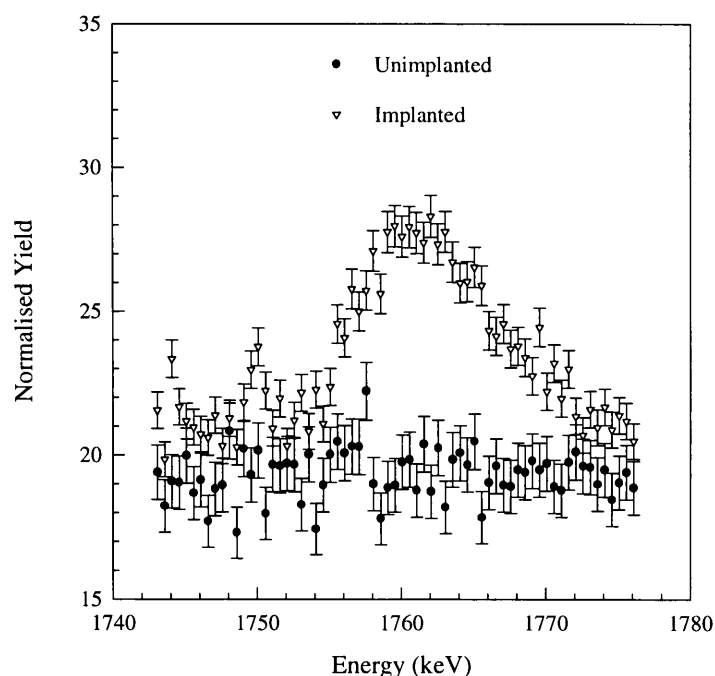
Fig. 6.3: **Yield curves from a silicon sample (silicon 03 in table 4.1) as a function of proton energy before and after implantation of 150 keV $^{13}C^{+}$ ions with a fluence of 2×10^{16} ions cm^{-2} at room temperature.**

The yield curves in figure 6.3 were used to estimate the sensitivity of the nuclear reaction analysis (NRA) for the 1.75 MeV resonance of the $^{13}C(p,\gamma)^{14}N$ reaction. In figure 6.3, the background has a mean value of 19 units with a standard deviation of 0.8 units while the ^{13}C reaction yield has a maximum value of 28 units with a standard deviation of 0.7 units. This resulted in a maximum yield height of 9 units with a standard deviation of 1.5 units. This meant that there was an experimental error of 17% for a data point in the peak. The ^{13}C yield was measured with a proton energy interval of 0.5 keV. This corresponds to a depth interval of $\Delta x = 17$ nm in silicon. As 8% of the implantation fluence ($\phi t = 2\times10^{16}$ ions cm^{-2}) will be

70

distributed in this interval at the position of the implantation peak, the fraction of ^{13}C atoms is given by

$$N = \frac{0.08 \times \phi \, t}{n \, \Delta x} = \frac{0.08 \times \left(2 \times 10^{16} \text{ cm}^{-2}\right)}{\left(4.98 \times 10^{22} \text{ cm}^{-3}\right) \times \left(17 \times 10^{-7} \text{ cm}\right)} = 0.02 \, . \qquad 6.1.1$$

Taking into account the experimental error of 17%, NRA employing the 1.75 MeV resonance of the $^{13}C(p,\gamma)^{14}N$ reaction is therefore sensitive to ^{13}C concentrations above 0.3% in silicon. The sensitivity of this method could also be estimated from the signal to background ratio seen in figure 6.1. If the above calculations are performed for this yield curve, it was found that the $^{13}C(p,\gamma)^{14}N$ reaction is sensitive to ^{13}C concentrations above 0.2% in a carbon target.

However, the yield curves in figure 6.1 and figure 6.2 were obtained by collecting a charge of 6×10^{-4} coulomb for each energy step while the proton beam current was kept at ± 0.5 µA. An increase in the amount of charge would lead to a decrease in the standard deviation and therefore an increase in the sensitivity of the method. Another factor that influences the sensitivity is the proton beam current. If the proton beam current decreases, the background (relative to the signal) might become so large that it eventually will mask the ^{13}C contribution completely.

6.1.1 $^{13}C^+$ IMPLANTED INTO SILICON

To investigate whether channelling effects play a role during implantation, some silicon samples were pre-implanted with 1×10^{15} $^{20}Ne^{++}$ ions with an energy of 300 keV to amorphize the surface region. This implantation energy is high enough to ensure amorphization to a depth of about one and a half times the depth of the $^{13}C^+$ ions implanted into silicon. As can be seen from figure 6.4, similar depth profiles were observed for samples which were pre-implanted with $^{20}Ne^{++}$ ions, independent of whether the samples were implanted at room temperature (300 K) or at liquid-nitrogen temperature (77 K).
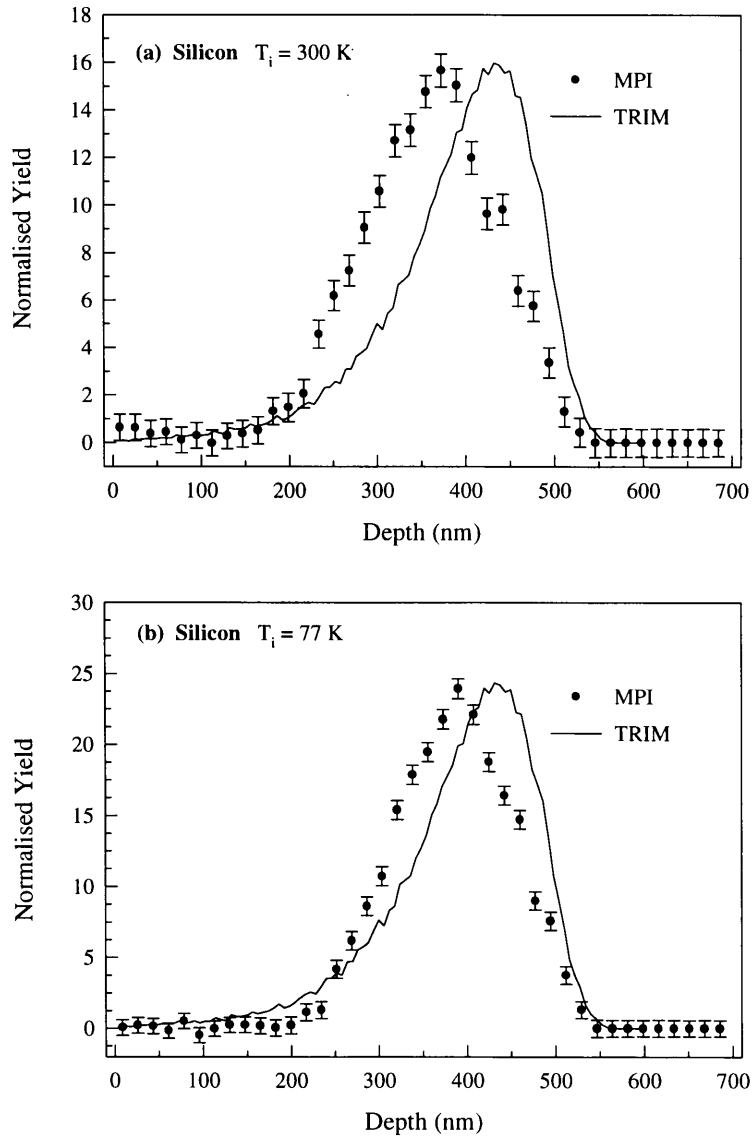
Fig. 6.4: Depth profiles of 150 keV $^{13}C^+$ ions implanted into silicon after implantation of 300 keV $^{20}Ne^{++}$ ions. The experimental results are obtained from nuclear reaction measurements done at the Max-Planck-Institut für Kernphysik (MPI) in Heidelberg. The top graph (a) shows the depth profile for a sample implanted at room temperature while the bottom graph (b) is the depth profile of an implantation performed at liquid-nitrogen temperature.

Figure 6.5 illustrates the depth profiles obtained for silicon samples, implanted at room temperature and liquid-nitrogen temperature, that were not pre-implanted with $^{20}Ne^{++}$ ions. Like the previous instance, there is clearly not a significant difference

in the depth profiles from the samples implanted at different temperatures. Furthermore, if one compares the depth profiles in figure 6.4 with those in figure 6.5, they were found to be very similar.
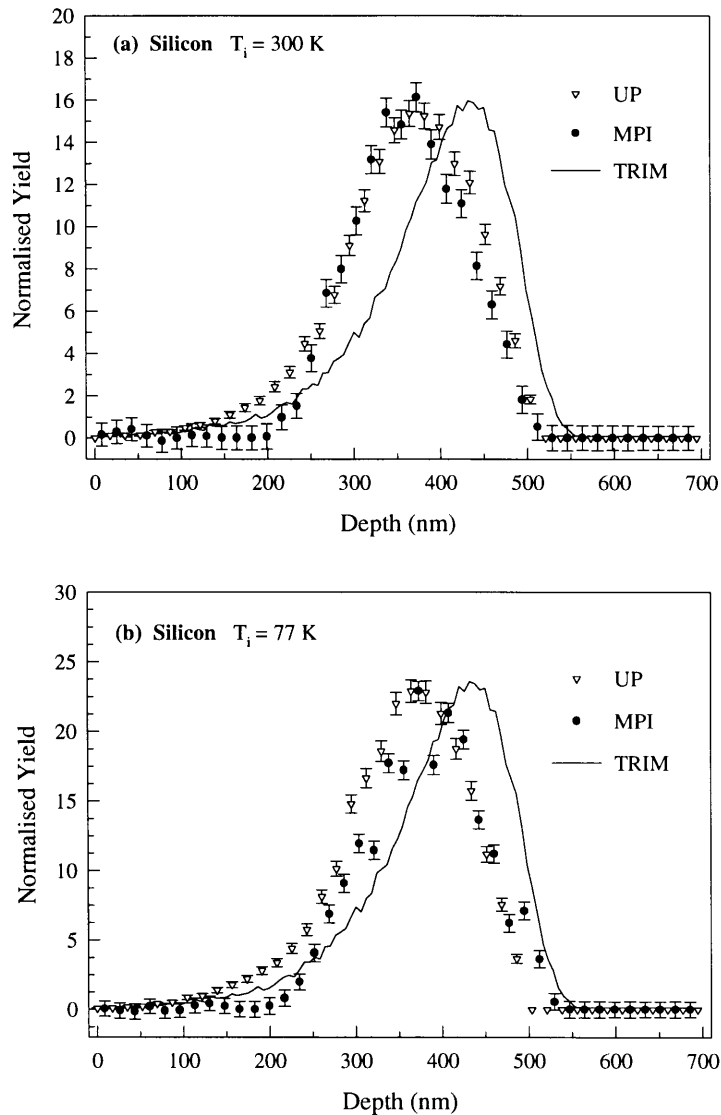
Fig. 6.5: Depth profiles of 150 keV $^{13}C^+$ ions implanted into silicon. The hollow symbols represent the results from measurements performed at the University of Pretoria (UP), while the solid symbols represent the results obtained from measurements performed at the Max-Planck-Institut für Kernphysik (MPI). The top graph (a) is the depth profile for the room temperature implant while the bottom graph (b) is the depth profile of the liquid-nitrogen temperature implant.

Channelling effects are thus not very important. This is expected for an implantation fluence of at least an order of magnitude higher than that needed for

73

complete amorphization. It must further be noted that all the samples were implanted with an incident angle of 7° to the surface normal, which is seven times larger than the critical angle for channeling of ^{13}C ions in silicon (~1°). This angle should thus be large enough to ensure that channelling of the incident particles is negligible.

Comparing the experimental depth distribution profiles with the theoretical predictions of TRIM 91.14 (see table 6.1), one finds both the projected range and the straggling somewhat smaller than expected. The average experimental projected range is found to be ~7% lower than the TRIM 91.14 estimate. The projected range values obtained from measurements done at the University of Pretoria (UP) and those obtained from measurements done at the Max-Planck-Institut für Kernphysik (MPI) agree within experimental error. The average experimental straggling value agrees within the experimental error with the TRIM 91.14 prediction.

Table 6.1: **Comparison of the experimental depth distribution moments and the theoretical predictions of TRIM 91.14 for 150 keV ^{13}C$^+$ implantations into silicon at both room (300 K) and liquid nitrogen (77 K) temperatures. The samples that were pre-implanted with ^{20}Ne^{++} were only analysed at the Max-Planck-Institut für Kernphysik (MPI) in Heidelberg. The samples that were not pre-implanted were analysed at the University of Pretoria (UP) as well as the Max-Planck-Institut für Kernphysik. The experimental errors quoted are 2σ values.**

Distribution parameters	Pre-implanted with ^{20}Ne^{++}		Not pre-implanted Analysed at MPI		Not pre-implanted Analysed at UP		Average moments	TRIM 91.14
	300 K	77 K	300 K	77 K	300 K	77 K		
Projected range (nm)	357 ± 21	382 ± 18	364 ±21	378 ± 22	357 ± 28	350 ± 28	365 ± 10	391
Straggling (nm)	71 ± 14	67 ± 14	63 ± 17	67 ± 20	80 ± 58	78 ± 59	71 ± 14	83
Skewness	-0.2 ± 0.2	-0.4 ± 0.2	0.0 ± 0.2	0.3 ± 0.2	-0.7 ± 0.2	-0.8 ± 0.3	-0.3 ± 0.2	-1.1
Kurtosis	2.8 ± 0.5	3.8 ± 0.5	2.4 ± 0.5	2.9 ± 0.5	3.7 ± 1.0	3.9 ± 1.3	3.2 ± 0.4	4.7

The differences observed for the third and fourth moments of the depth distribution are somewhat more serious. While TRIM 91.14 predicts a distinctly asymmetric

depth profile, the values for the skewness (γ) and kurtosis (β) of the experimental distributions are almost Gaussian ($\gamma \approx 0$, $\beta \approx 3$). It must, however, be born in mind that the depth resolution for silicon at the position of the maximum, compares rather unfavourably with the straggling width. This might render these moments somewhat less reliable. The nature of this asymmetry is investigated in section 6.3. A large discrepancy between the experimental skewness values is observed ($+0.3 \rightarrow -0.8$) and they do not agree within experimental error (0.2) with each other. The experimental skewness values do also not agree within experimental error with the predicted values. Some of the experimental kurtosis values also do not agree within experimental error with the predicted values, but the experimental values obtained from the different experimental facilities do agree within experimental error.

The average experimental skewness and kurtosis values do not agree within experimental error with those predicted by TRIM 91.14. In this investigation, the average experimental projected range was found to be ~7% lower than the TRIM 91.14 prediction for an implantation energy of 150 keV. Paltemaa et al [86] (see table 5.9 in section 5.3) on the other hand, found their experimental projected ranges ~4% higher than the TRIM 91.14 predictions for implantation energies ≤ 100 keV.

6.1.2 $^{13}C^+$ IMPLANTED INTO GALLIUM ARSENIDE

As it was obvious from the previous paragraph that channelling effects were not important for high dose implantations, no further samples were pre-implanted with $^{20}Ne^{++}$ for amorphization. It can be seen from figure 6.6 that the depth profiles from the samples implanted at the different temperatures are similar. These profiles also agree favourably with the theoretical predictions of TRIM 91.14.
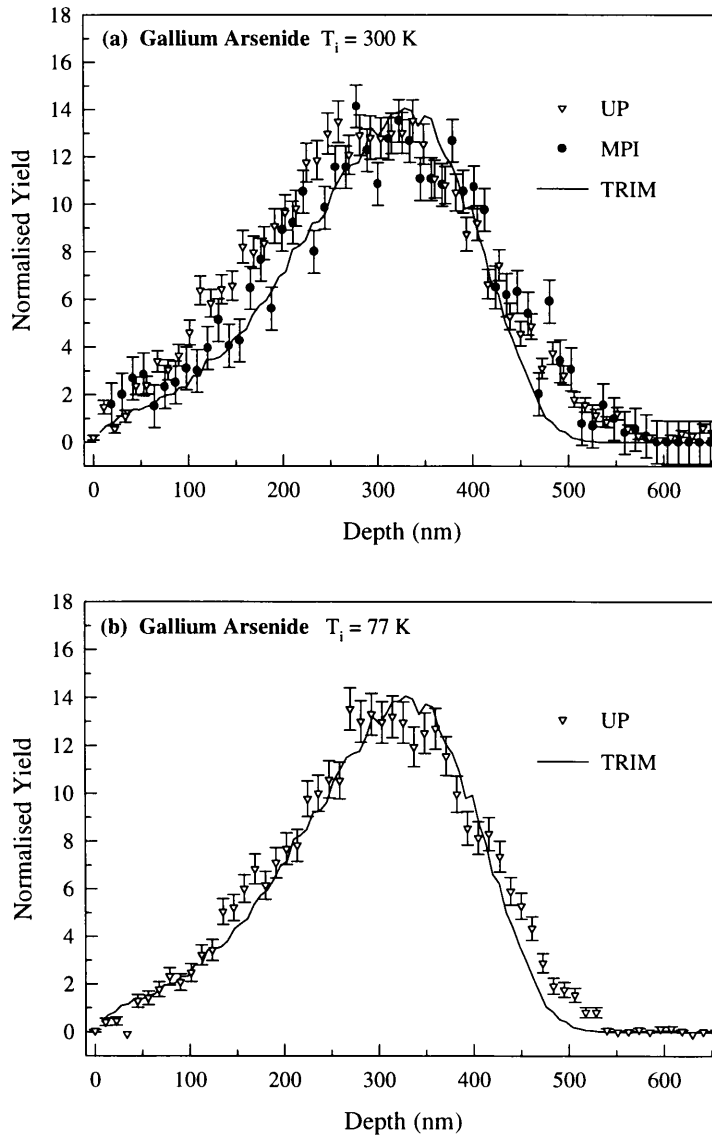
Fig. 6.6: Experimental depth profiles of 150 keV $^{13}C^+$ ions implanted into gallium arsenide. The top graph (a) represents the profile of the ^{13}C room temperature implantation (300 K) of gallium arsenide while the bottom graph (b) represents the profile of the ^{13}C liquid-nitrogen temperature implantation (77 K) of gallium arsenide. For comparison the TRIM 91.14 predicted profiles are represented as solid lines.

Excellent agreement was found between the experimental and theoretical projected ranges (see table 6.2). The agreement between the experimental values from the two analysing facilities and the agreement between the experimental and the theoretically predicted values are all within the experimental errors. Although there is a relatively large difference between the experimental values and the theoretical predictions of

76

the straggling width, this has to be compared with a high statistical uncertainty. Straggling width values from the University of Pretoria agree within experimental error with those obtained at the Max-Planck-Institut für Kernphysik.

When comparing the experimental and theoretical skewness values contained in table 6.2 it can be seen that, similar to the $^{13}C^+$ implantations into silicon, the theoretically predicted distribution profile is asymmetric with a negative skewness. In this instance it is, however, rather small. TRIM 91.14 predicts a slight asymmetric profile, while the experimental values are closer to a normal distribution. However, the experimental results, within the experimental errors, agree with an almost symmetrical profile ($\gamma \approx 0$).

Table 6.2: **Moments of the experimental depth distributions for 150 keV $^{13}C^+$ ions implanted into gallium arsenide at room temperature (300 K) and liquid-nitrogen temperature (77 K). For comparison the TRIM 91.14 results are listed in the last column.**

Distribution parameters	Analysed at MPI 300 K	Analysed at UP 300 K	Analysed at UP 77 K	Average moments	TRIM 91.14
Projected range (nm)	297 ± 13	285 ± 16	295 ± 17	292 ± 9	287
Straggling (nm)	112 ± 28	115 ± 30	102 ± 29	109 ± 17	97
Skewness	-0.2 ± 0.2	0.1 ± 0.2	-0.2 ± 0.2	-0.1 ± 0.2	-0.5
Kurtosis	2.6 ± 0.3	2.8 ± 0.6	2.6 ± 0.6	2.6 ± 0.4	2.9

Experimental kurtosis results on the other hand are in excellent agreement, and the experimental results all agree within the experimental errors with the predicted values. The average experimental moments, with the exception of the skewness value, agree within the experimental errors to those predicted by TRIM 91.14.

77

6.1.3 $^{13}C^+$ IMPLANTED INTO MAGNESIUM

Similar depth profiles were not obtained for magnesium samples implanted with $^{13}C^+$ ions at room temperature and liquid-nitrogen temperature. The experimentally obtained depth profiles were also not in good agreement with the depth profiles obtained from the TRIM 91.14 predictions. These discrepancies are clearly illustrated in figure 6.7.
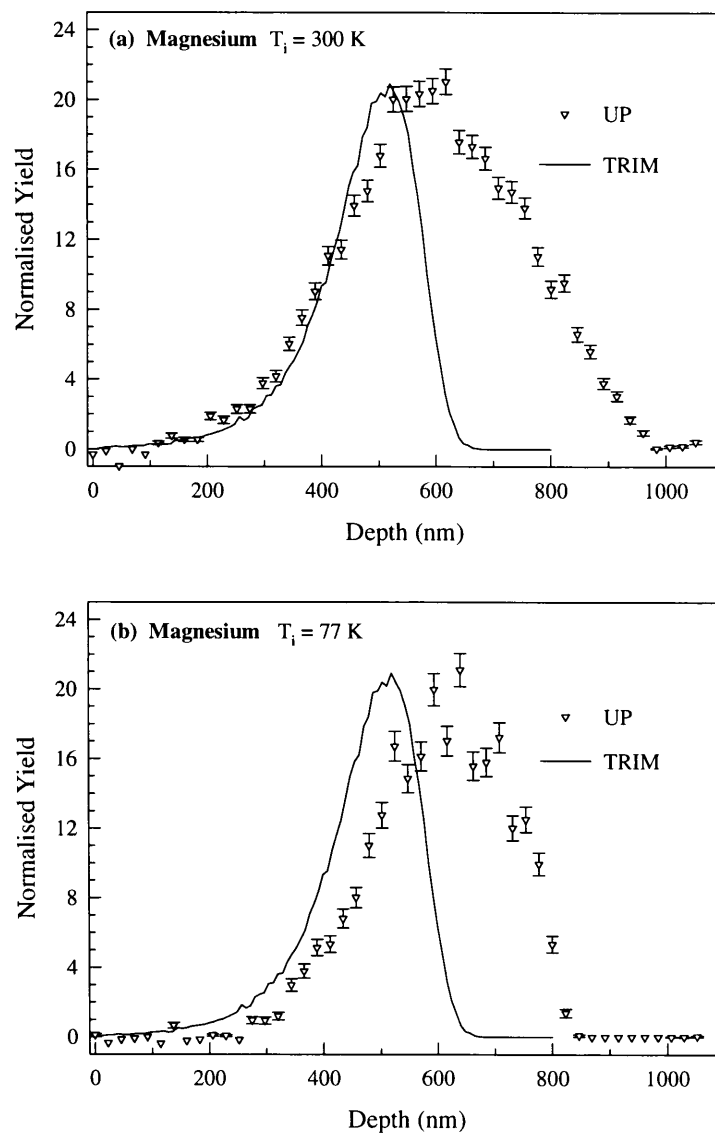
Fig. 6.7: Depth distributions of 150 keV $^{13}C^+$ ions implanted into magnesium at room temperature (top graph) and liquid-nitrogen temperature (bottom graph). The comparative theoretical predicted distribution is represented by the solid line.

78

The experimental depth distribution parameters together with the corresponding TRIM 91.14 theoretical predictions are contained in table 6.3.

Table 6.3: Experimental depth distribution parameters of 150 keV $^{13}C^+$ ions implanted into magnesium at room temperature (300 K) and liquid-nitrogen temperature (77 K), compared with the theoretical predicted distribution parameters.

Distribution parameters	Analysed at UP		Average moments	TRIM 91.14
	300 K	77 K		
Projected range (nm)	599 ± 33	602 ± 38	601 ± 25	467
Straggling (nm)	158 ± 44	115 ± 71	137 ± 41	93
Skewness	0.16 ± 0.22	-0.05 ± 1.42	0.06 ± 0.72	-1.14
Kurtosis	2.62 ± 0.67	2.24 ± 1.62	2.24 ± 0.88	4.86

Poor agreement between experimental and theoretical predicted projected ranges and straggling widths was also observed for $^{27}Al^+$ implanted magnesium (discussed in section 6.2.3). This might be due to erroneous stopping power values or diffusional redistribution of the $^{13}C^+$ ($^{27}Al^+$) ions. It must be noted that the stopping powers of protons [6] and $^{13}C^+$ ions [94] in magnesium are based on interpolations between neighbouring elements, as no experimental data were available. Another factor that might influence the accuracy of the experimental distribution parameters was the strong increase in the background observed with increasing proton energy. This can clearly be seen from figure 6.8 which illustrates the yield from implanted and unimplanted magnesium as a function of incident proton energy.

The disagreement between the experimental projected ranges and the theoretical prediction is found to be much larger than the experimental error. The disagreement between the straggling widths obtained experimentally and theoretically is just as large and is also well outside the experimental error. The high statistical uncertainty

of the experimental results makes it difficult to compare the experimental higher moments with the theoretical predictions. None of the average experimental moments agree within experimental error with the TRIM 91.14 predictions.
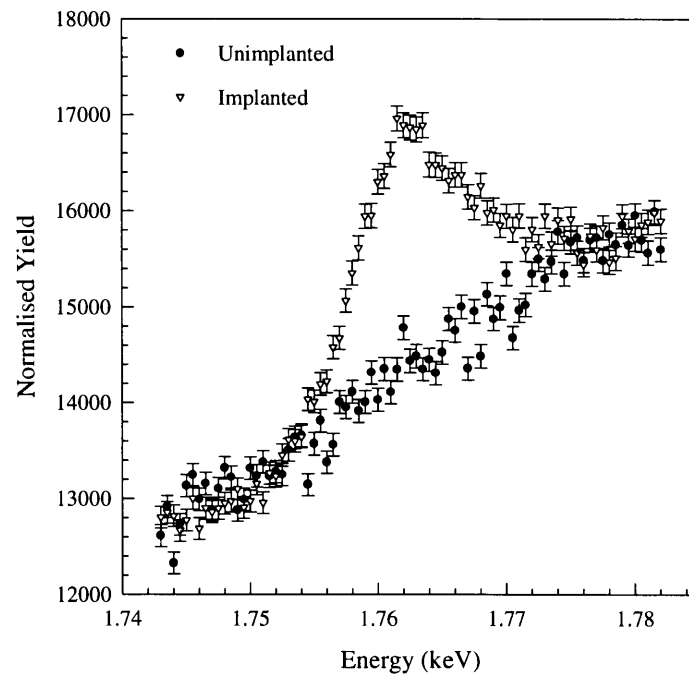
Fig 6.8:   Yield curves from magnesium samples as a function of proton energy before and after implantation of 150 keV $^{13}C^+$ ions with a fluence of 5×10^{16} ions cm^{-2} at room temperature.

6.1.4 $^{13}C^+$ IMPLANTED INTO STAINLESS STEEL

Depth distribution profiles from samples implanted at room temperature agree reasonably with those from samples implanted at liquid nitrogen temperature. These profiles are depicted in figure 6.9. The projected ranges obtained from analysis at the University of Pretoria (UP) are ~10% lower than those analysed at the Max-Planck-Institut für Kernphysik (MPI). This difference might be due to an uncertainty in the determination of the surface position.

80
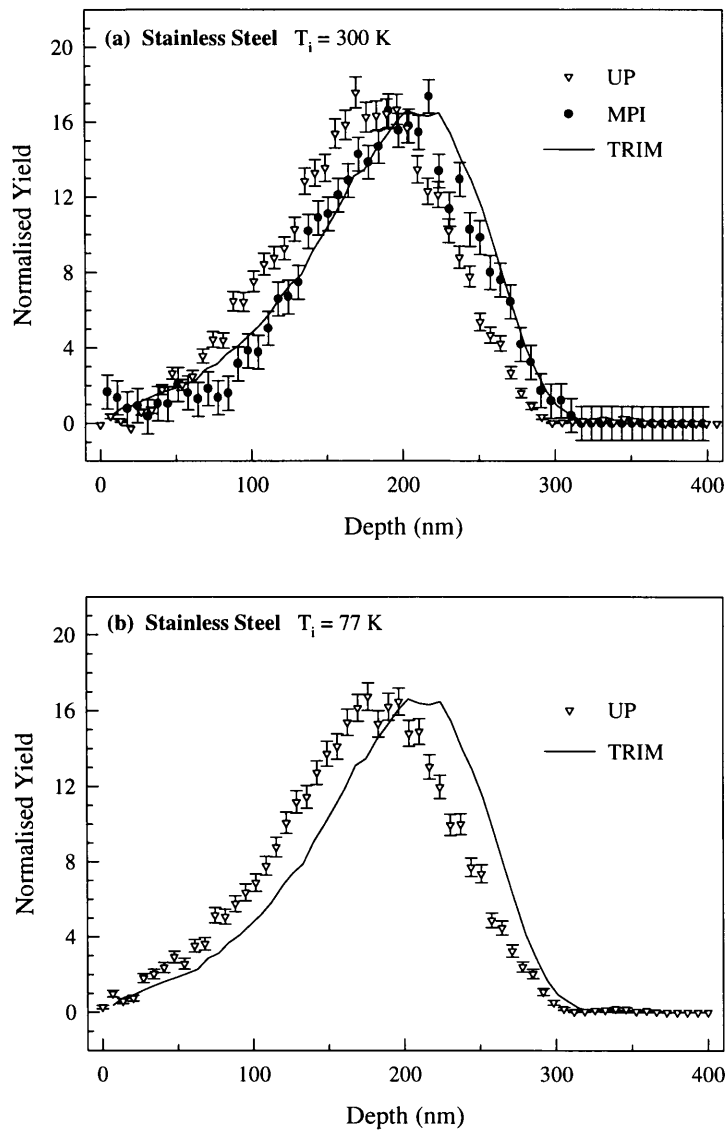
Fig. 6.9: Depth distribution profiles of 150 keV ^{13}C$^+$ ions implanted into stainless steel. The top graph (a) shows the distribution profile for the room temperature implantation, while the bottom graph (b) shows the distribution profile for the liquid nitrogen implantation.

The experimentally determined depth distribution parameters and corresponding theoretical predictions are contained in table 6.4. Experimentally determined projected ranges agree within experimental error with the theoretically predicted values. The agreement between the projected range values from the different analysing facilities is also better than the experimental error. However, it would seem that the projected range values obtained from analysis at the University of

81

Pretoria are slightly too low and the differences are just not explained by the statistical uncertainty. A possible explanation for this might be the formation of an oxide layer on the surface of the stainless steel sample after the implantation and prior to the analysis, or the formation of a carbon layer on the sample during the nuclear reaction analysis due to poor vacuum conditions. This discrepancy was, however, not investigated further.

Table 6.4: Moments of the experimental depth distributions of 150 keV $^{13}C^+$ ions implanted into stainless steel at room temperature (300 K) and liquid nitrogen temperature (77 K). For comparison the theoretical predictions of TRIM 91.14 are given in the last column.

Distribution parameters	Analysed at MPI SSteel - 77 K	Analysed at UP SSteel - 300 K	Analysed at UP SSteel - 77 K	Average moments	TRIM 91.14
Projected range (nm)	186 ± 7	170 ± 10	169 ± 10	175 ± 6	183
Straggling (nm)	57 ± 13	53 ± 19	58 ± 18	56 ± 10	59
Skewness	-0.6 ± 0.2	-0.2 ± 0.4	-0.3 ± 0.3	-0.4 ± 0.2	-0.5
Kurtosis	3.4 ± 0.4	2.8 ± 1.1	2.8 ± 0.8	3.0 ± 0.5	3.2

In view of the relatively good agreement between the experimental and theoretical predicted projected ranges, it seems unlikely that channeling effects in the polycrystalline structure of the sample play a significant role. The deviation of the experimental projected range from the theoretical prediction is furthermore in the opposite direction of what would be expected from channeling. The average grain size of the stainless steel sample was determined by scanning electron microscopy to be 7 μm.

In excellent agreement are the values of the straggling widths. Although there is a large statistical uncertainty in the experimental values, the agreement with the TRIM 91.14 values is better than the experimental error, and the difference between the straggling widths from the two analysing facilities is also better than the experimental error.

For $^{13}C^+$ implantations into stainless steel the theoretical skewness is of the same order as for the gallium arsenide implantation, and thus not as extreme as for the silicon and magnesium implantations. This asymmetry and negative skewness are investigated in section 6.3. The experimental skewness values also indicate a slight asymmetry and all these values agree within the experimental error with the TRIM 91.14 prediction.

The kurtosis values obtained experimentally agree within experimental error with those predicted by TRIM 91.14, while the experimental kurtosis values from the different facilities also agree within experimental error. Except for the projected range, which is just outside the experimental error, all the average experimental moments agree within the experimental error with the TRIM 91.14 predictions.

6.2 RESULTS FOR ALUMINIUM IMPLANTATION PROFILES USING THE $^{27}Al(p,\gamma)^{28}Si$ REACTION

The surface position of the $^{27}Al^+$ implanted samples were determined by measuring yield curves for single crystal aluminium. The yield curve from the single crystal aluminium is illustrated in figure 6.10. Figure 6.10 was also used to determine the instrumental energy resolution at the surface of the sample. It can be seen from this figure that there are two channels between 10% and 90% peak height. Because each channel corresponds to an energy difference of 0.5 keV, the instrumental energy resolution would be given by 1 keV. It must be noted that the instrument energy resolution here is two times better than the instrument resolution when the $^{13}C(p,\gamma)^{14}N$ reaction was used. This might be explained by the shorter time interval in which the nuclear reaction measurements with the $^{27}Al(p,\gamma)^{28}Si$ reaction are performed (about half of that needed with the $^{13}C(p,\gamma)^{14}N$ reaction). This shorter time interval reduces the effect of the drift of the analysing magnet on the instrumental energy resolution.

83
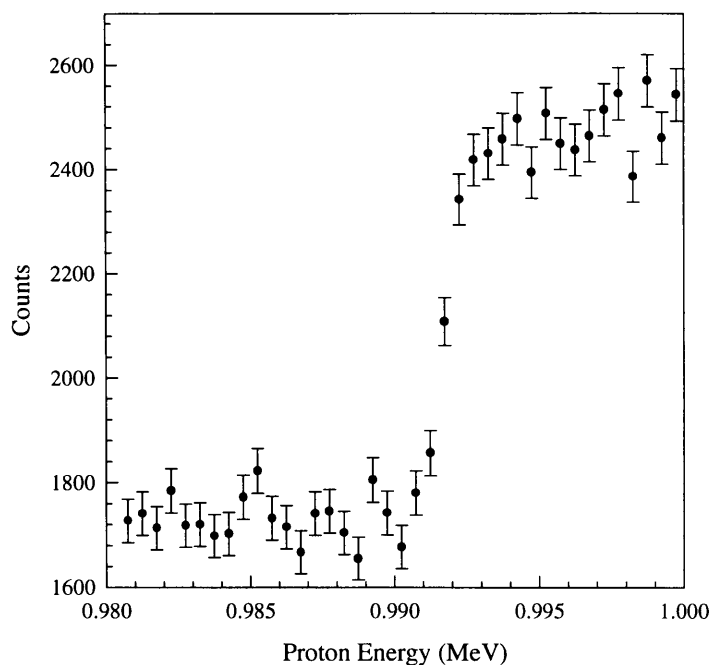
Fig. 6.10: Yield curve from single crystal aluminium using the $^{27}Al(p,\gamma)^{28}Si$ nuclear reaction to determine the surface position of the $^{27}Al^+$ implanted samples.

The Bohr straggling was determined as a function of depth (using equation 2.4.2) and at the ^{27}Al peak position (246 nm in silicon) the energy straggling was calculated (using equation 2.4.5) to be 4.47 keV. Again note that this is just an illustrative value, and that the energy straggling is a function of the depth. The energy resolution was calculated by quadratic summation of the instrumental energy resolution and energy straggling, and was determined to be 5.08 keV at 246 nm. This was converted to a depth scale and was found to be 124 nm. The validity of the Bohr estimate was acceptable for this energy range. Yield curves are simultaneously corrected for instrumental resolution and straggling before the analysis is performed.

The importance of the straggling effect for proton beams at 0.992 MeV is illustrated in figure 6.11. From this figure, it is clear that the depth resolution value depicted here at a particular depth is better than the depth resolution value depicted in figure 6.2 for the same depth. For Si the depth resolution at a typical depth of 200 nm is 112 nm compared to a depth resolution of 170 nm at the same depth in section 6.1.

84

This is due to the higher proton stopping power values at the lower proton beam energy.
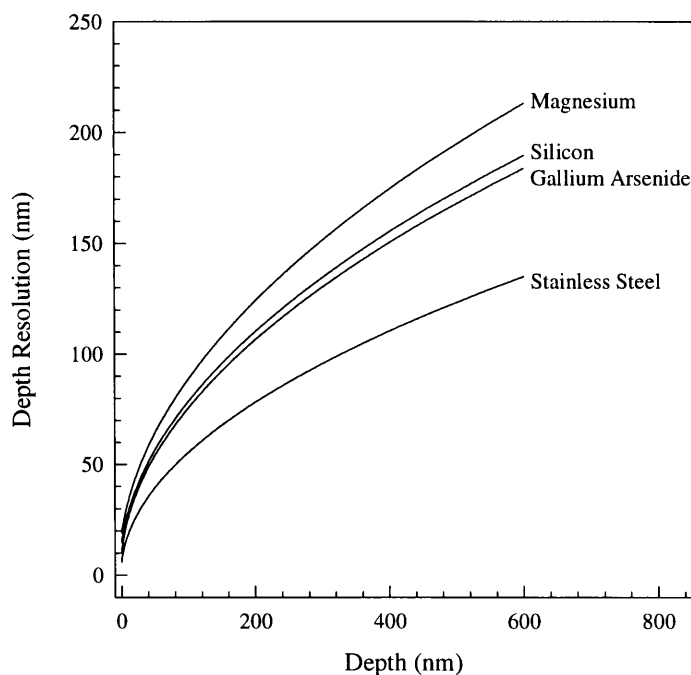
Fig. 6.11: Depth resolution (FWHM) of the ^{27}Al(p,γ)^{28}Si reaction in silicon, gallium arsenide, magnesium and stainless steel as a function of depth. A proton energy spread of 1 keV was taken into account when determining the depth resolution.

Yield curves for silicon targets, before and after implantation with ^{27}Al$^+$ ions, as a function of incident proton energy are depicted in figure 6.12. The peak of the implanted aluminium is superimposed on the background, which increases with the energy of the analysing beam. The main source of this increasing background is the large number of weak proton resonances in the silicon isotopes. As more reaction channels open up at higher energies an increasing background is observed. The energy dependence of this contribution is taken into account by adding a linear term to the fit equation used for the background correction.

85
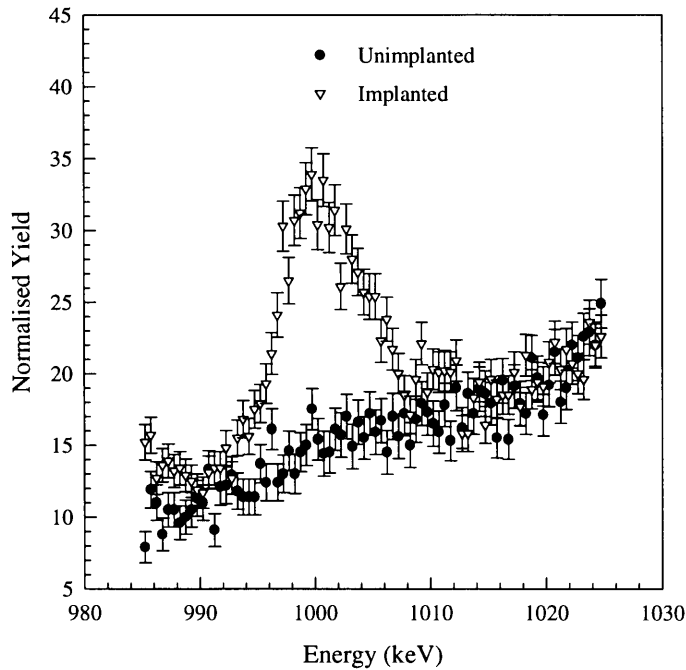
Fig. 6.12: Yield curves from a silicon sample as a function of proton energy before and after implantation of 150 keV ^{27}Al$^+$ ions with a fluence of 5×10^{16} ions cm^{-2} at room temperature.

The yield curves in figure 6.12 were used to estimate the sensitivity of the nuclear reaction analysis when the 0.992 MeV resonance of the ^{27}Al(p,γ)^{28}Si reaction was employed. It can be seen from figure 6.12 that the background at the peak position has a value of 15 units and a standard deviation of 1.6 units, while the ^{27}Al(p,γ)^{28}Si reaction yield has a maximum value of 34 units with a standard deviation of 1.8 units. The result was a maximum yield height of 19 units and a standard deviation of 3.4 units. This resulted in an experimental error of 17% for a data point in the peak. The reaction yield was measured with a proton beam energy interval of 0.5 keV which corresponds to a depth interval of 112 nm in silicon. Of the implanted fluence (5×10^{16} ions cm^{-2}), 21% will be distributed in the interval containing the maximum peak height. In this interval (using equation 6.1.1), the fraction of ^{27}Al atoms will therefore be

$$\frac{0.21 \times \left(5 \times 10^{16} \text{ cm}^{-2}\right)}{\left(4.98 \times 10^{22} \text{ cm}^{-3}\right) \times \left(112 \times 10^{-8} \text{ cm}\right)} = 0.19 .$$

86

Taking the experimental error of 17% into account, the nuclear reaction analysis with the ^{27}Al(p,γ)^{28}Si reaction will be sensitive to ^{27}Al concentrations above 3% in silicon (depending on the charge collected and the beam current). The yield curve in figure 6.12 was obtained by collecting a total charge of 6×10^{-4} coulomb while the proton beam current was kept at ± 0.5 μA.

6.2.1 ^{27}Al$^+$ IMPLANTED INTO SILICON

It can be seen from figure 6.13 that the depth profiles for samples implanted at room temperature do not differ significantly from those obtained for samples implanted at liquid nitrogen temperature. The experimental depth distribution moments together with the theoretical predictions are presented in table 6.5.

Table 6.5: Experimental depth parameters and comparative TRIM 91.14 theoretical predictions of 150 keV ^{27}Al$^+$ ions implanted into silicon at room temperature (300 K) as well as liquid nitrogen temperature (77 K).

Distribution parameters	Analysed at MPI		Analysed at UP		Average moments	TRIM 91.14
	Si - 300 K	Si - 77 K	Si - 300 K	Si - 77 K		
Projected range (nm)	252 ± 16	245 ± 15	241 ± 19	247 ± 19	246 ± 9	242
Straggling (nm)	80 ± 14	73 ± 10	62 ± 23	72 ± 23	72 ± 13	77
Skewness	-0.23 ± 0.08	-0.29 ± 0.04	0.05 ± 0.38	-0.01 ± 0.27	-0.12 ± 0.2	-0.33
Kurtosis	3.02 ± 0.16	3.11 ± 0.09	2.62 ± 1.12	2.85 ± 0.74	2.90 ± 0.4	2.80

The projected ranges of all the experimental determinations agree within experimental error to that of the TRIM 91.14 predictions. The reproducibility of the experimental projected ranges is also very good, with all the projected ranges determined at the University of Pretoria (UP) agreeing within the experimental error with that determined at the Max-Planck-Institut für Kernphysik (MPI).

Although it might seem that the difference between the experimental and theoretical values for the straggling is high, the high statistical uncertainty which leads to a large experimental error must be taken into account. The agreement between experimental and theoretical straggling values, as well as the agreement between the experimental straggling values from the different experimental facilities do, however, agree within experimental error.
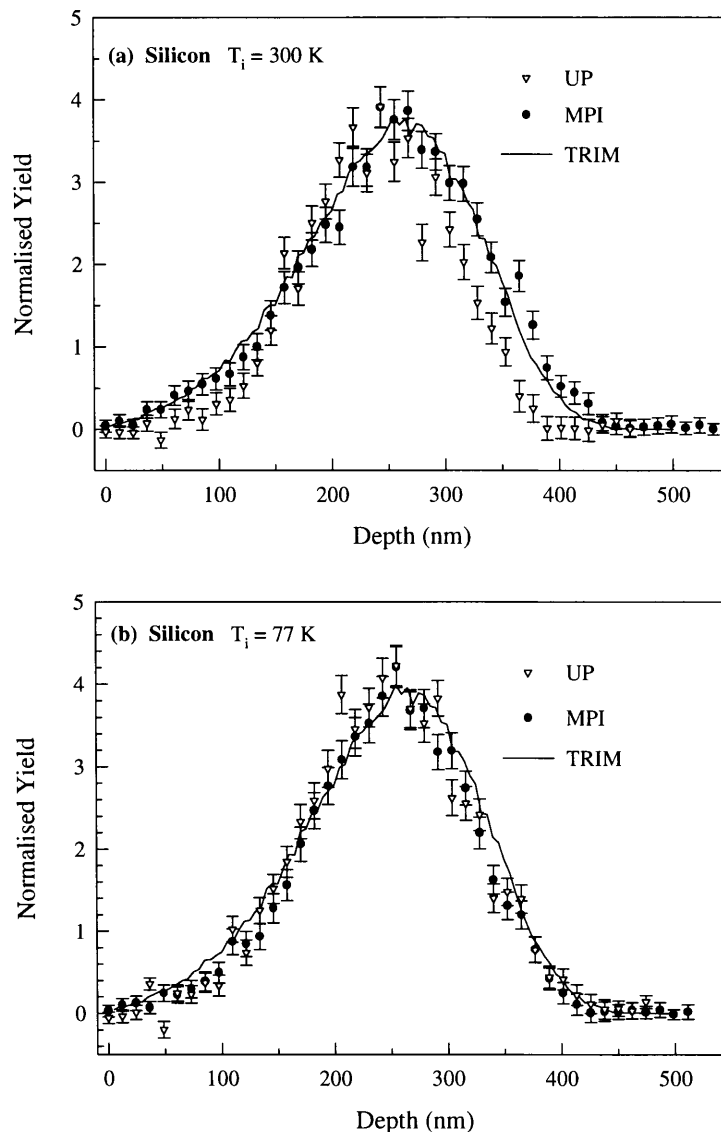

Fig. 6.13 Experimental depth profiles of 150 keV ^{27}Al$^+$ ions implanted into silicon compared with the theoretical prediction of TRIM 91.14. Graph (a) shows the result for the sample implanted at room temperature (300 K) while graph (b) depicts the results of the sample implanted at liquid nitrogen temperature (77 K).

88

A comparison of the straggling results obtained from the two analysing facilities (UP and MPI) indicates a rather large discrepancy for the room temperature implantation while that of the liquid nitrogen implantation compares quite favourably. It must, however, be noted that MPI room temperature straggling result is higher than the liquid-nitrogen value with the same margin that the UP room temperature straggling result is lower than the liquid-nitrogen value. The average room temperature straggling value from the two experimental measurements will therefore agree very well with the average liquid-nitrogen straggling value.

The values for the skewness obtained from the Max-Planck-Institut für Kernphysik (MPI) agree within experimental error with the theoretical predictions. Although the skewness values obtained from the University of Pretoria (UP) seem to differ quite significantly from the theoretical predictions, the large experimental errors have to be taken into account. The experimental kurtosis values are within experimental error in agreement with TRIM 91.14. The kurtosis values obtained from the two experimental measurements agree also within experimental error.

The experimental results obtained at UP indicate an almost Gaussian distribution ($\gamma\approx0$, $\beta\approx3$), while those obtained at MPI indicate a slight asymmetry. TRIM 91.14 on the other hand predicts an asymmetry with a larger negative skewness. This trend is investigated in section 6.3.

The average experimental projected range and straggling values agree within experimental error with those predicted by TRIM 91.14. The average experimental skewness and kurtosis values do, however, not agree within experimental error with the TRIM 91.14 predictions. In this investigation, the average experimental projected range was found to be ~2% higher than the TRIM 91.14 prediction. On the other hand, the average experimental projected range of Paltemaa et al [86] (see table 5.9 in section 5.2) is ~2% lower and that of Crowder [84] (see table 5.8 in section 5.2) ~21% lower than the TRIM 91.14 prediction.

89

6.2.2 $^{27}Al^+$ IMPLANTED INTO GALLIUM ARSENIDE

The experimental depth profiles obtained for the two implantation temperatures agree reasonably with each other and with the theoretical predictions, as is evident from figure 6.14. Profiles obtained from the two experimental measurements also agree reasonably with each other, especially in the case of the room temperature implantations.
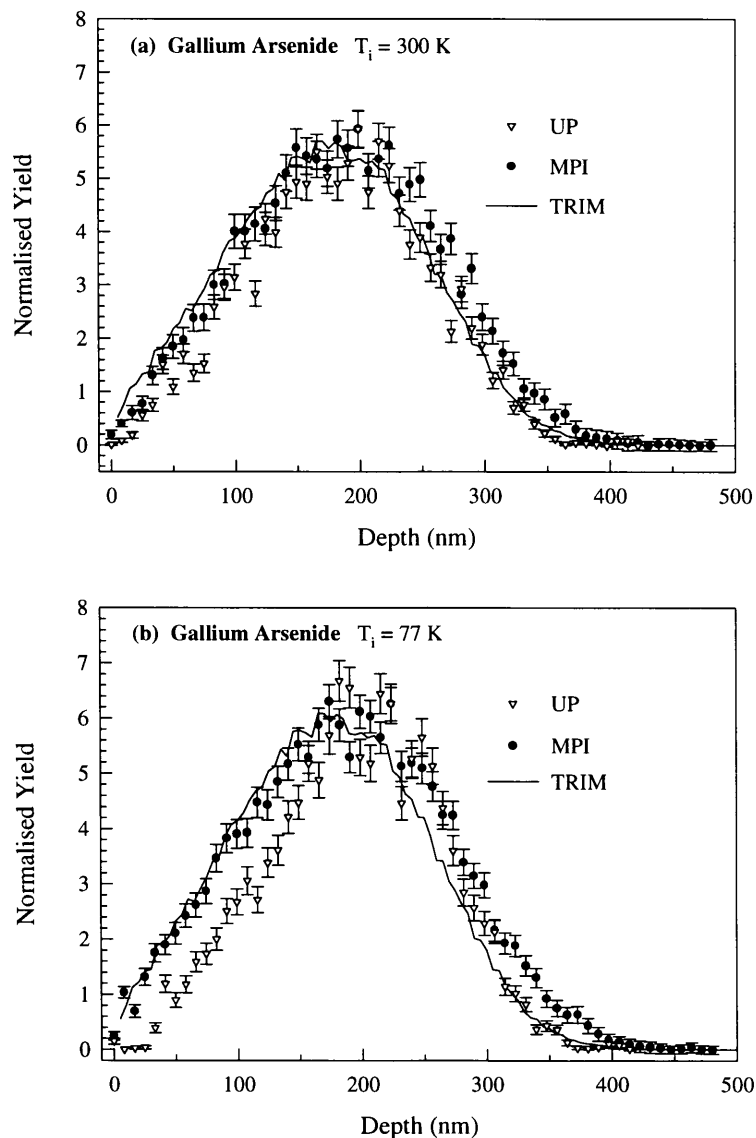
Fig. 6.14: Depth distribution profiles of 150 keV $^{27}Al^+$ implanted into gallium arsenide at (a) room temperature (300 K) and at (b) liquid nitrogen temperature (77 K). For comparison the TRIM 91.14 predicted depth distribution is also given.

90

In analysing the depth distributions, it was found that all the projected ranges are slightly larger than the values predicted by TRIM 91.14 (see table 6.6). The liquid nitrogen implantation measured at the University of Pretoria (UP) gives the largest deviation from the TRIM 91.14 prediction. The only projected range measurement that agrees within experimental error with the TRIM 91.14 prediction is the room temperature implantation measurement performed at UP. However, in view of the statistical errors listed in table 6.6, this difference is not of much significance. The agreement between the projected ranges from the different analysing facilities is excellent.

Table 6.6: Moments of the experimental depth distributions for 150 keV $^{27}Al^+$ ions implanted into gallium arsenide at room (300 K) and liquid nitrogen temperatures (77 K). For comparison the TRIM 91 results are given in the last column.

Distribution parameters	Analysed at MPI		Analysed at UP		Average moments	TRIM 91.14
	GaAs - 300 K	GaAs - 77 K	GaAs - 300 K	GaAs - 77 K		
Projected range (nm)	186 ± 11	186 ± 10	183 ± 13	194 ± 14	187 ± 6	170
Straggling (nm)	78 ± 12	82 ± 12	70 ± 20	68 ± 21	75 ± 9	76
Skewness	0.04 ± 0.05	0.05 ± 0.04	0.01± 0.21	-0.08 ± 0.25	0.01 ± 0.08	0.05
Kurtosis	2.40 ± 0.10	2.50 ± 0.09	2.54 ± 0.59	2.55 ± 0.69	2.50 ± 0.23	2.50

The experimental straggling widths agree within experimental error with those predicted by TRIM 91.14. The differences between the straggling values obtained from the different analysing facilities are also within the experimental errors. Experimentally obtained kurtosis values and TRIM 91.14 predictions are in excellent agreement. The kurtosis values obtained from the two analysing facilities also agree within experimental errors. In comparing the values for the skewness and kurtosis given in table 6.6, it is quite evident that both the experimental and theoretical values predict an almost Gaussian profile ($\gamma \approx 0$, $\beta \approx 3$). Except for the projected range, all the average experimental moments agree within experimental errors with the TRIM 91.14 predictions.

6.2.3 ^{27}Al$^+$ IMPLANTED INTO MAGNESIUM

Figure 6.15 represents the experimental and theoretical depth profiles obtained from magnesium samples implanted with aluminium. From this it is evident that there is a slight difference between the profile from magnesium implanted at room temperature and the profile from magnesium implanted at liquid nitrogen temperature. In view of the relatively large experimental error, this difference is not very significant.
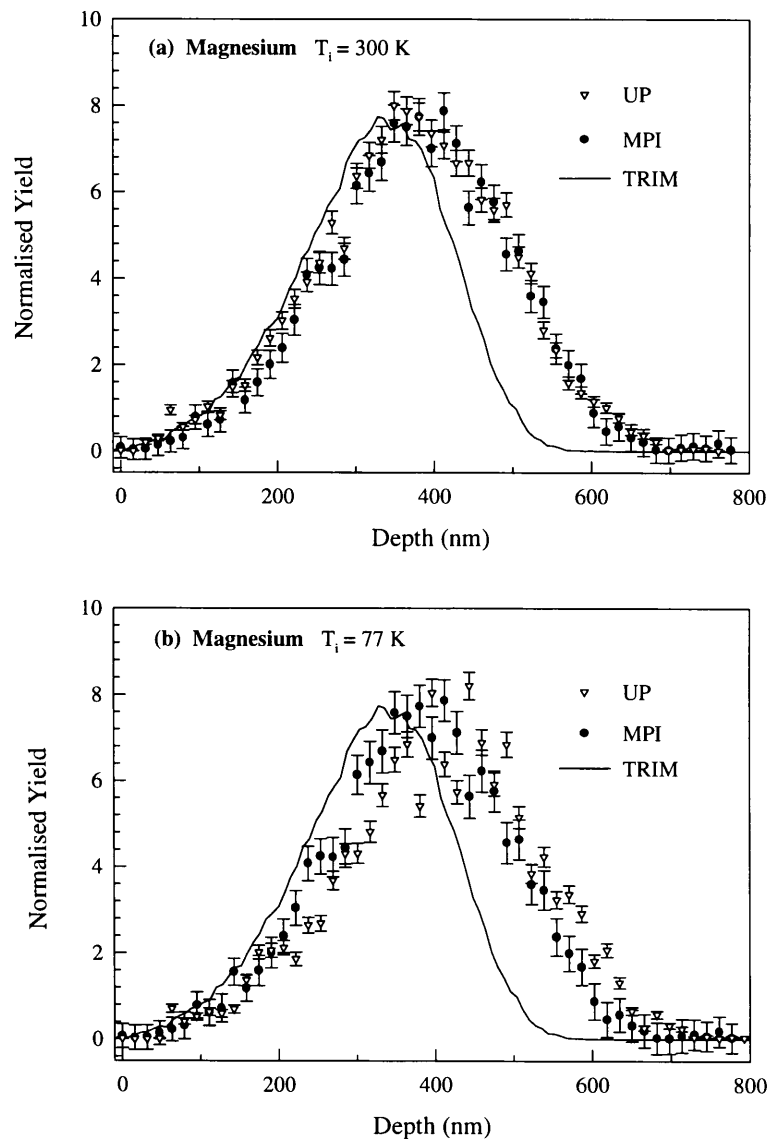

Fig 6.15: ^{27}Al$^+$ distribution profiles in magnesium after being implanted with an incident energy of 150 keV and comparative theoretical profile predicted by TRIM 91.14. The implantations were performed at (a) room temperature (300 K) as well as at (b) liquid nitrogen temperature (77 K).

92

There is, however, a significant difference between the experimental profiles and that obtained from the TRIM 91.14 prediction. The experimental values for the projected range are larger than the values obtained from the TRIM 91.14 prediction (see table 6.7). This large discrepancy is impossible to explain with experimental errors. On the other hand, the values obtained from the two analysing facilities agree very well within experimental errors. It would therefore seem that the poor agreement between the theoretical and experimental values is either due to a possible error in the theoretical prediction, or due to a possible error during the implantation process. This last possibility, however, seems unlikely as both targets show similar deviations from theory. Experimental depth distribution parameters and corresponding TRIM 91.14 predictions are given in table 6.7.

Table 6.7: Experimental depth distribution parameters of 150 keV $^{27}Al^+$ ions implanted into magnesium at room temperature and liquid nitrogen temperature, compared with the theoretically predicted distribution parameters.

Distribution parameters	Analysed at MPI		Analysed at UP		TRIM 91.14
	Mg - 300 K	Mg - 77 K	Mg - 300 K	Mg - 77 K	
Projected range (nm)	377 ± 17	405 ± 17	370 ± 23	404 ± 23	314
Straggling (nm)	116 ± 23	122 ± 23	120 ± 23	124 ± 23	95
Skewness	-0.09 ± 0.09	-0.23 ± 0.08	-0.13 ± 0.09	-0.14 ± 0.09	-0.35
Kurtosis	2.95 ± 0.21	2.96 ± 0.22	2.84 ± 0.21	2.73 ± 0.22	2.85

A similar trend is observed in the values of the straggling widths. The experimental straggling widths are also larger than those predicted by TRIM 91.14. In this case, a large part of the discrepancy can be explained by the statistical uncertainty of the experimental distribution. It is rather unlikely that the discrepancies in projected range and straggling values are due to channelling, as the lattice order is strongly

93

distorted in metals after high dose implantations. Furthermore, one would then expect a highly skewed distribution with a positive third moment [95], which is not observed. The agreement between the two experimental facilities is excellent and well within the experimental error.

It is, as in the previous case (section 6.1.3), difficult to make a comparison between the experimental and theoretical predicted skewness values. Although the different experimental values agree within experimental error with each other, the agreement between experimental and theoretical values is well outside the experimental error. Excellent agreement is obtained between experimental kurtosis values and theoretical kurtosis values predicted by TRIM 91.14. The discrepancy between experimental and theoretical values as well as the discrepancy between experimental values from the different facilities are within experimental error. This is, however, not of much significance, as the projected range and straggling are the dominant parameters. It must, however, be noted that all the values for the skewness and kurtosis indicate a close to normal distribution ($\gamma \approx 0$ and $\beta \approx 3$).

Due to the large discrepancies between the experimental and theoretically predicted projected range and straggling width values, it was decided to repeat the experiment. To try and ensure an "oxide free" surface, special care was taken during the sample preparation. After the usual mechanical polishing, the magnesium samples were etched with a solution of one part nitric acid to twenty parts methanol. Afterwards the samples were rinsed in pure methanol followed by a rinse in ethanol. Of the four samples prepared, two were implanted at the Schonland Research Centre for Nuclear Sciences and analysed at the University of Pretoria (UP). The other two samples were implanted at the Max-Planck-Institut für Kernphysik (MPI) and analysed at both MPI and UP.

No significant improvement was obtained in the correlation between the experimental and the theoretical predicted distribution profiles for the samples implanted at Schonland. There was a large improvement in the correlation for the MPI analysis of the samples implanted at MPI. However, when the same samples were analysed at UP, the projected ranges were found to be very similar to that obtained previously,

94

the only difference being an increase in the straggling values. This serious inconsistency can not be explained at this stage and will have to be investigated further.

The average depth distribution parameters of all the $^{27}Al^+$ implantation profiles in magnesium are presented in table 6.8. These parameters were obtained by simultaneously fitting the five room temperature implantation profiles as well as the five liquid nitrogen implantation profiles. It must be noted that these profiles were analysed at MPI and at UP. These results still indicate larger than expected projected range and straggling parameters, while the skewness value is not as negative as expected. The kurtosis value on the other hand seems to be in good agreement. It is clear from table 6.8 that, except for the kurtosis, all the experimentally obtained range parameters do not agree within experimental error with the theoretical prediction.

Table 6.8: Depth distribution moments obtained by simultaneously fitting all the MPI and UP profiles of 150 keV $^{27}Al^+$ implantations into magnesium and the comparative TRIM 91.14 predictions.

Distribution parameters	Results obtained by simultaneously fitting all the MPI and UP profiles	TRIM 91.14
Projected range (nm)	364 ± 10	314
Straggling (nm)	120 ± 12	95
Skewness	-0.15 ± 0.10	-0.35
Kurtosis	2.81 ± 0.16	2.85

The discrepancy between experimental and theoretical projected ranges is similar to that observed when the ^{13}C implantations into magnesium were analysed. The assumption was made there that this discrepancy might be due to erroneous stopping power values. To investigate this assumption the stopping power of magnesium was determined by Rutherford Backscattering (RBS). Figure 6.16 illustrates the backscattering spectra of 1.5 MeV and 1.8 MeV ^4He ions incident on magnesium and silicon samples.

95
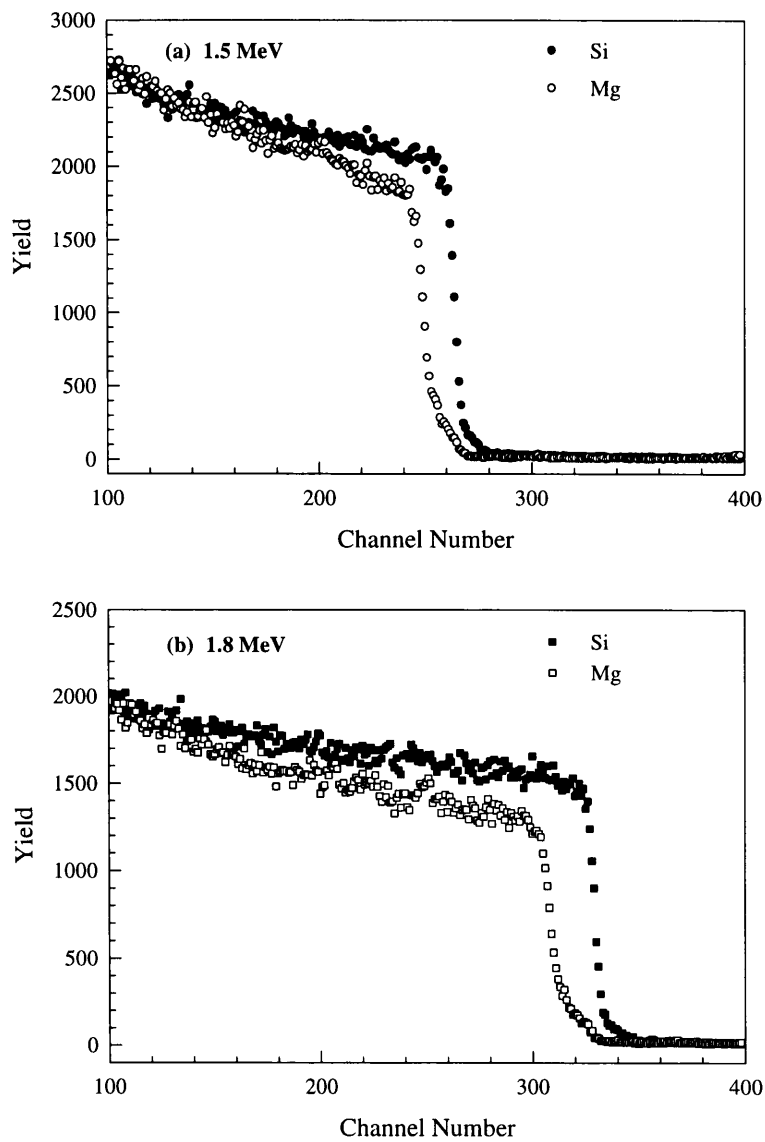
Fig 6.16: Backscattering spectra for (a) 1.5 MeV and (b) 1.8 MeV ^{4}He ions incident on magnesium and silicon samples.

The number of detected particles for a thickness element δx, for a backscattering spectrum is given by

$$A = \left(\frac{d\sigma}{d\Omega}\right) \cdot \mu \cdot \delta x \cdot \Omega \cdot Q. \qquad 6.2.1$$

96

Here $\left(\dfrac{d\sigma}{d\Omega}\right)$ is the differential scattering cross section, μ is the atomic density of the target, Ω is the detector solid angle and Q is the number of incident particles. The thickness element δx can be chosen in such a way that it represents the width of one channel of the RBS spectra. Using the stopping power definition $\left(S = \dfrac{dE}{dx}\right)$ the number of detected particles per channel is now given by

$$N = \left(\frac{d\sigma}{d\Omega}\right) \cdot \mu \cdot \frac{\delta E}{S} \cdot \Omega \cdot Q.$$
6.2.2

By determining the ratio of the number of detected particles for magnesium and silicon and assuming Rutherford scattering, one can obtain the following equation

$$S_{Mg} = \left(\frac{Z_{Mg}}{Z_{Si}}\right)^2 \cdot \frac{\mu_{Mg}}{\mu_{Si}} \cdot \frac{N_{Si}}{N_{Mg}} \cdot S_{Si}.$$
6.2.3

As the ^{4}He stopping power in silicon given in the Ziegler tables $\left(S_{Si}\right)$ is based on many experimental data, the assumption can be made that this value would be close to correct. If the number of detected particles for both magnesium and silicon is measured at the surface position (figure 6.16), and are both substituted together with S_{Si} into equation 6.2.3, the value obtained for the ^{4}He stopping power in magnesium (at an incident energy of 1.5 MeV) is found to be 38.39 eV cm^2/10^{15} atoms, which is around 17% lower than that given in the Ziegler tables [96](46.38 eV cm^2/10^{15} atoms). If the above calculation is done for an incident energy of 1.8 MeV, the ^{4}He stopping power in magnesium is found to be 36.19 eV cm^2/10^{15} atoms, which is again around 17% lower than that given in the Ziegler tables (43.45 eV cm^2/10^{15} atoms).

As the scattering cross-section for protons at 992 keV is not described by the Rutherford formula, this determination can not be done for protons. However, it is

suspected that similar deviations from the listed stopping powers as found for α-particles are also present for the proton and heavy ion stopping powers.

A lower stopping power would result in an increase of the depth at which the implanted ions are stopped. On the other hand, because of the smaller energy losses of the analysing protons, it would apear as if the implanted ions are situated at smaller depths than they really are. Due to the scaling of the stopping power with the effective charge, it is expected that the influence of the erroneous stopping power will be larger for the implanted ions than for the analysing protons. The assumption of erroneous stopping powers therefore seems to be true and this will have to be investigated further.

6.2.4 $^{27}\text{Al}^+$ IMPLANTED INTO STAINLESS STEEL

From figure 6.17, it can be seen that the agreement between the experimental and theoretical depth profiles obtained for stainless steel samples implanted with aluminium are very good for both the room temperature and the liquid nitrogen implantations. Furthermore, the agreement between the experimental distribution profiles obtained from the different experimental facilities is also good.

The experimental values for the depth distribution parameters and comparative theoretical predictions are presented in table 6.9. The experimentally determined projected ranges agree within experimental errors with those predicted by TRIM 91.14 and the values obtained from the two experimental facilities also agree within experimental errors. Also in very good agreement are the experimental and theoretical straggling widths. The values from the different experimental facilities agree also well within the experimental errors.

98
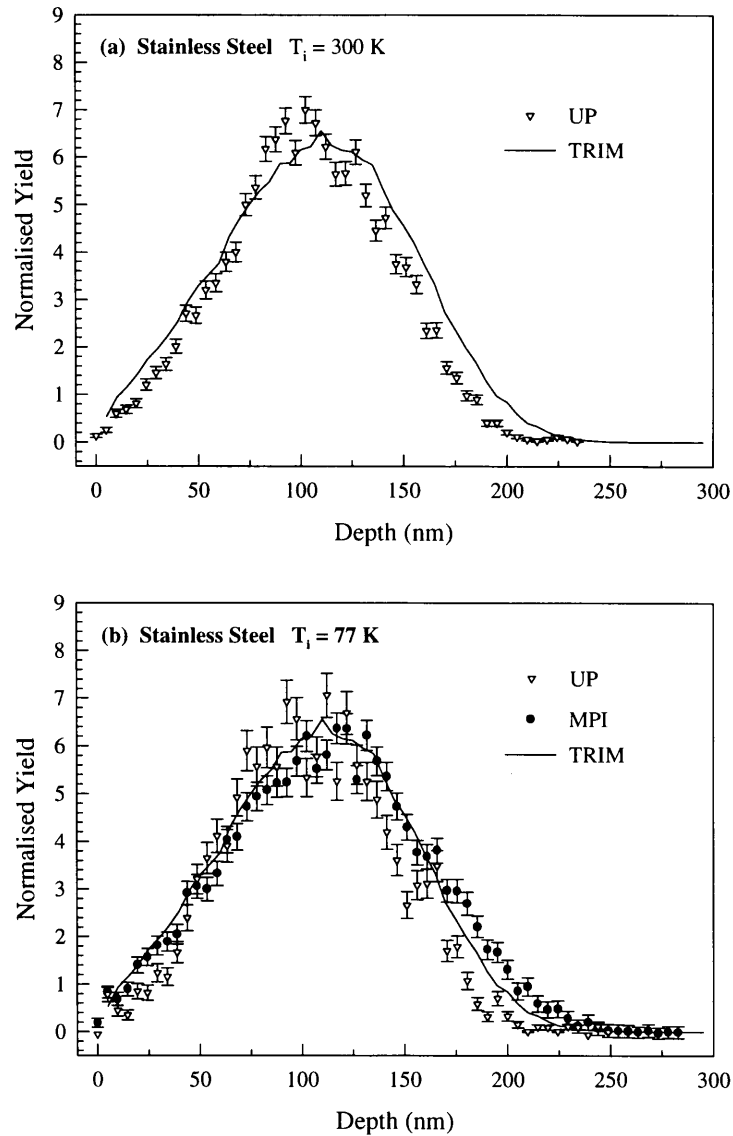
Fig. 6.17: Experimental depth distributions and comparative theoretical distributions for $^{27}Al^+$ ions implanted into stainless steel at (a) room temperature (300 K) and at (b) liquid nitrogen-temperature (77 K).

The experimental skewness values are in good agreement with the theoretically predicted ones. Also in good agreement are the experimental skewness values obtained from the two experimental facilities. Experimental values for kurtosis are again in very good agreement with the theoretical predictions of TRIM 91.14, and the difference is always smaller than the experimental error. The difference between kurtosis values from the different analysing facilities is also small. The skewness and kurtosis values indicate an almost Gaussian profile ($\gamma \approx 0$, $\beta \approx 3$).

Table 6.9: Moments of the experimental depth distributions of 150 keV $^{27}Al^+$ ions implanted into stainless steel at room temperature (300 K) and liquid-nitrogen temperature (77 K). For comparison the theoretical predictions of TRIM 91.14 are given in the last column.

Distribution parameters	Analysed at MPI SSteel - 77 K	Analysed at UP SSteel - 300 K	SSteel - 77 K	Average moments	TRIM 91.14
Projected range (nm)	112 ± 5	103 ± 7	104 ± 8	106 ± 4	105
Straggling (nm)	47 ± 8	39 ± 10	40 ± 12	42 ± 6	45
Skewness	0.03 ± 0.05	-0.01 ± 0.48	0.08 ± 0.25	0.05 ± 0.19	0.06
Kurtosis	2.51 ± 0.11	2.68 ± 0.48	2.69 ± 0.75	2.63 ± 0.30	2.51

6.3 SKEWNESS AND KURTOSIS OF THE IMPLANTATION PROFILES

During the analysis of the implantation distributions in section 6.1 and section 6.2, it was found that theoretically predicted distributions for light targets had an asymmetry with a large negative skewness. The experimentally determined distributions on the other hand were almost normal ($\gamma \approx 0$, $\beta \approx 3$). It was therefore decided to systematically analyse the theoretical predictions of the skewness and kurtosis values as a function of incident ion energy, incident ion mass as well as target mass.

Figure 6.18 illustrates theoretically obtained skewness and kurtosis values for $^{13}C^+$ implantation profiles into silicon, gallium arsenide, magnesium and stainless steel as a function of implantation energy. It can be seen from this figure that the theoretical distribution for the $^{13}C^+$ implantations, will only be approximately Gaussian for very low implantation energies. There is a decrease in the skewness values with increasing ion energy. This negativity in the skewness values is much more notable for the lighter mass targets. Furthermore, there is a sharp increase in the kurtosis values of the silicon and magnesium targets as the implantation energy increases. For the gallium arsenide and stainless steel targets the kurtosis values first drop a little

before increasing slightly. However, the kurtosis values of these two targets stay relatively close to that for a normal distribution ($\beta \approx 3$).
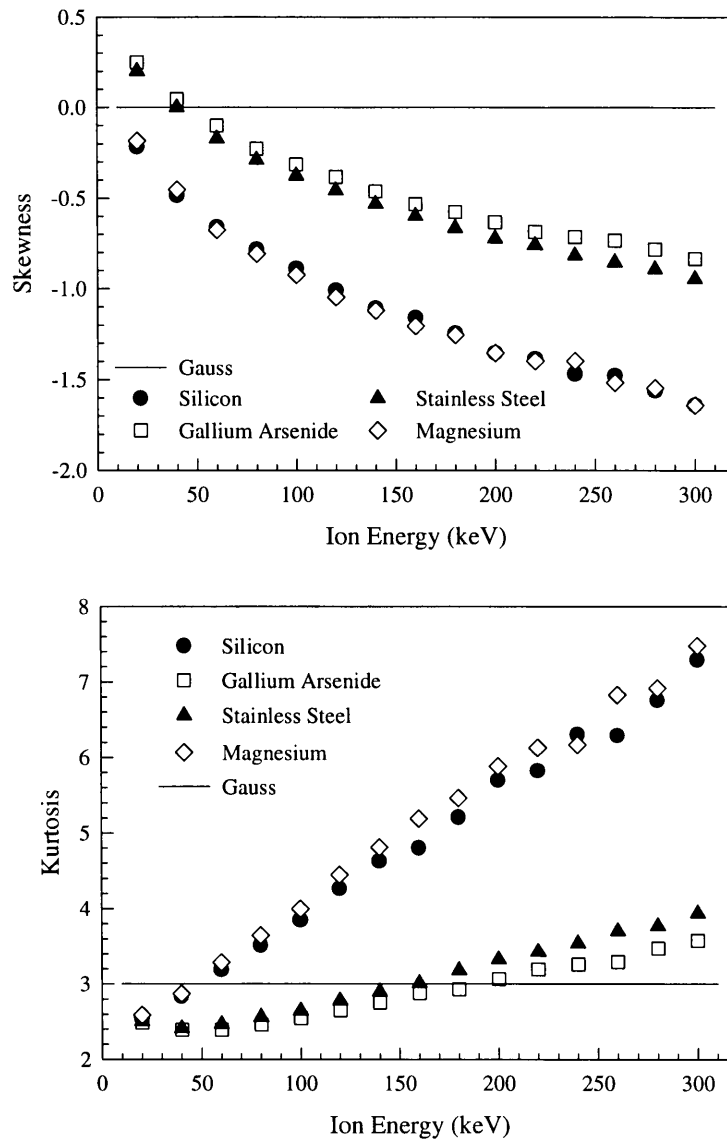

Fig. 6.18: Theoretically predicted skewness and kurtosis values for $^{13}C^{+}$ implanted silicon, gallium arsenide, magnesium and stainless steel samples as a function of implantation energy.

Theoretically obtained skewness and kurtosis values of $^{27}Al^{+}$ implanted silicon, gallium arsenide, magnesium and stainless steel as a function of implantation energy are illustrated in figure 6.19. A similar decrease in the skewness values (more

101

negative), as observed for the $^{13}C^+$ implantation, is observed with increasing ion energy. The skewness value at a given implantation energy is, however, either more positive or less negative than the corresponding skewness value of the $^{13}C^+$ implantation and the deviation from a symmetric distribution ($\gamma \approx 0$) is therefore smaller. As before, the lighter targets again display the larger deviations from symmetry at higher energies.
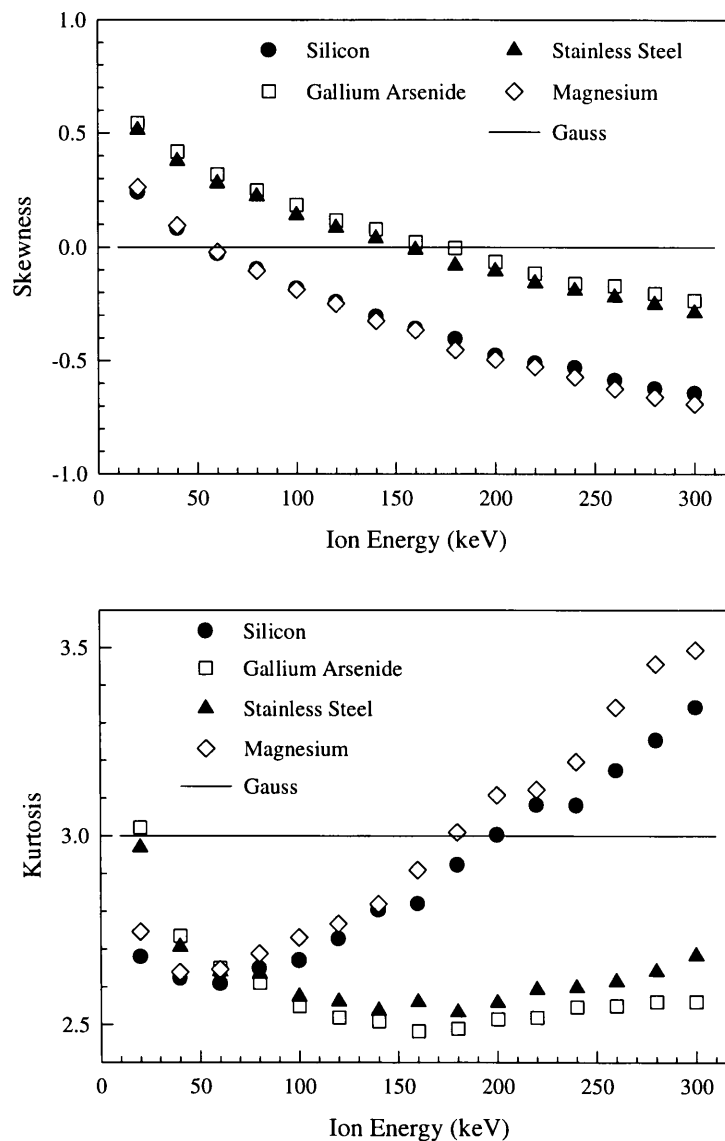
Fig. 6.19:Theoretical skewness and kurtosis values of $^{27}Al^+$ implanted samples as a function of implantation ion energy.

102

The kurtosis values obtained for the silicon and magnesium targets first decrease slightly (up to an implantation energy of 60 keV) and then increase with increasing implantation energy. The values do, however, stay between 2.5 and 3.5 in the energy region investigated. For the gallium arsenide and stainless steel targets, the kurtosis values decrease until an implantation energy of around 150 keV is reached before it starts to increase slowly. Kurtosis values stay between 2.5 and 3 for these targets.

The dependence of skewness and kurtosis values on the atomic mass of the incident ion (at an incident ion energy of 150 keV) is illustrated in figure 6.20. It can be seen from this figure that the skewness values for the four targets under investigation become less negative as the atomic mass of the implanted ion increases. The silicon and magnesium targets again illustrate a larger negative skewness value than the heavier mass gallium arsenide and stainless steel targets.

The kurtosis values, on the other hand, decrease with increasing implantation ion atomic mass, with the values for the heavier targets much closer to a normal distribution than that of the lighter targets. If one considers the last three implantation ion masses, it would seem that the skewness values reached a maximum value around an implantation ion mass of 25. The same trend can be observed when the kurtosis values of these ion masses are considered, only this time a minimum value is reached. It must be noted, that the skewness and kurtosis values obtained for hydrogen implantation into the targets are omitted from figure 6.20. These values were large (negative for skewness, positive for kurtosis) and made the presentation of the values obtained for the other implantation ions difficult.
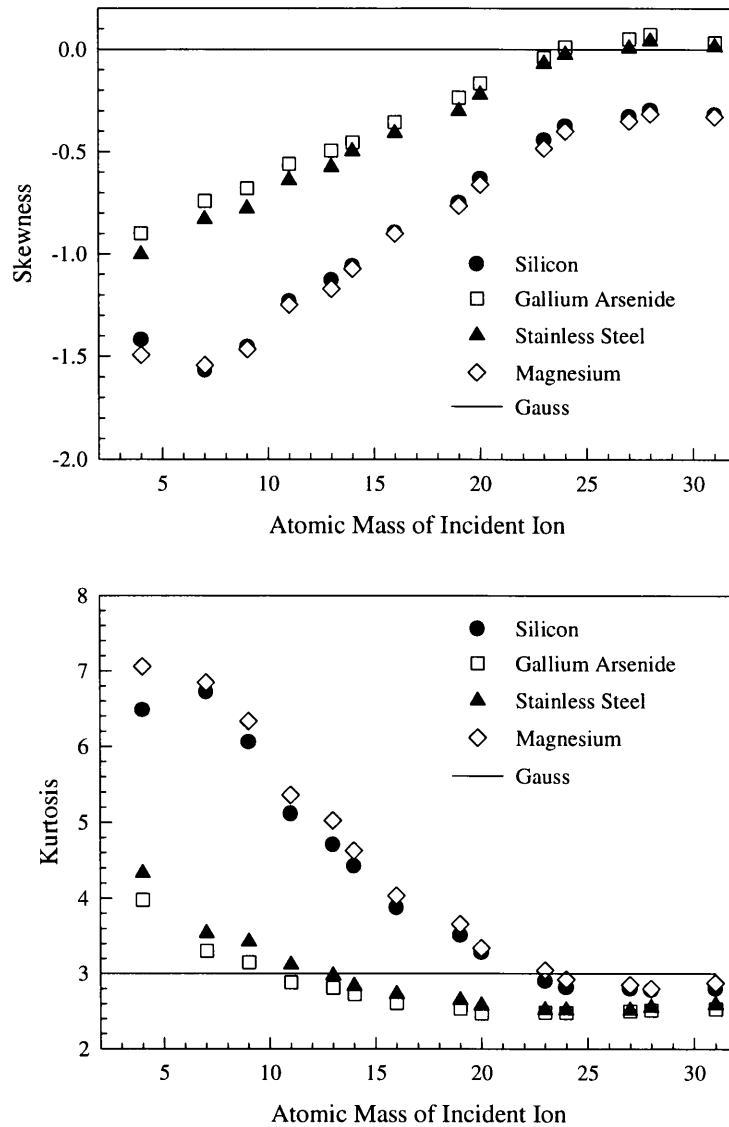
103

Fig. 6.20: Theoretical skewness and kurtosis values of 150 keV implantations into silicon, gallium arsenide, magnesium and stainless steel targets as a function of implantation ion atomic mass.

It was clear from the above investigations that the atomic mass of the target has a large influence on the skewness and kurtosis values. This is evident from figure 6.21, which illustrates the skewness and kurtosis values for 150 keV $^{13}C^+$ and $^{27}Al^+$ implantations as a function of the atomic mass of targets. The skewness value increases (less negative) with increasing target mass, while the kurtosis values decrease with increasing target mass. For both the skewness and kurtosis values there seem to be three distinct regions. A region between target atomic mass 25 and 60 in

104

which there is a steady increase (skewness) or decrease (kurtosis). Then there is a region below target atomic mass 25, where there is first a decrease and then an increase in the skewness values and vice versa for the kurtosis values. Lastly, there seems to be a region above target atomic mass 60, where the skewness and kurtosis values seem to fluctuate around a constant value.
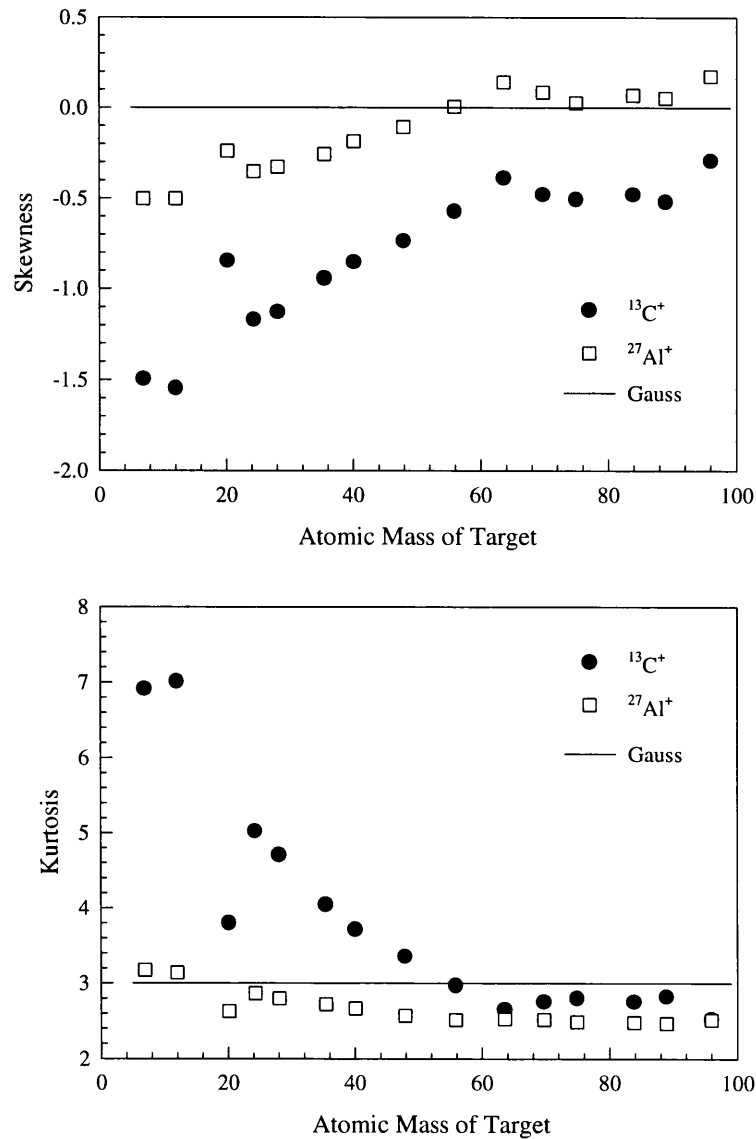
Fig. 6.21: Theoretical skewness and kurtosis values of 150 keV $^{13}C^+$ and $^{27}Al^+$ implantations as a function of atomic mass of the target.

105

The above theoretical investigation into the shape of the implantation profiles indicates an increasing asymmetry, with negative skewness and increasing kurtosis, with increasing ion energy and decreasing ion and target mass. This was not reflected in the experimental skewness and kurtosis values presented in sections 6.1 and 6.2. It would therefore seem that the TRIM 91.14 skewness and kurtosis predictions become less realistic with increasing incident ion energy as well as with decreasing ion and target mass. This tendency should be experimentally investigated further using different light ion-target combinations.

CHAPTER 7

SUMMARY OF RESULTS

The distribution profiles of $^{13}C^+$ and $^{27}Al^+$ ions implanted into silicon, gallium arsenide, magnesium and stainless steel samples at room temperature and at liquid nitrogen temperature were determined by making use of the $^{13}C(p,\gamma)^{14}N$ and $^{27}Al(p,\gamma)^{28}Si$ resonant nuclear reactions. The procedure used to analyse the distribution profiles yielded projected range, straggling width, skewness and kurtosis parameters. These experimentally measured parameters are compared with the theoretically predicted parameters obtained from the TRIM 91.14 code. The results of this study can be summarised as followed.

7.1 THE $^{13}C(p,\gamma)^{14}N$ REACTION ANALYSIS

Nuclear reaction analysis was employed successfully to obtain the distribution profiles of $^{13}C^+$ ions implanted into silicon, gallium arsenide, magnesium and stainless steel. No significant discrepancies were found between distributions from ions implanted at room temperature and those implanted at liquid nitrogen temperature.

The experimental projected range and straggling parameters of $^{13}C^+$ implantations into silicon were found to be slightly smaller (~7% for projected range and ~17% for straggling) than the TRIM 91.14 calculations. On the other hand, previously determined projected ranges of $^{13}C^+$ in silicon [86] were found to be ~4% larger than the TRIM 91.14 predictions for implantation energies ≤100 keV. The determined third and the fourth moments, are experimentally close to those of a normal distribution, while TRIM 91.14 predicts a strongly asymmetric distribution. Although it is generally expected that implantation profiles should display negative skewness, TRIM 91.14 seems to grossly overestimate this for silicon. The TRIM 91.14 predicted kurtosis value also seems to be too high.

107

For $^{13}C^+$ ions implanted into gallium arsenide, all the experimentally obtained distribution moments agree within experimental errors with those obtained from the theoretical predictions of TRIM 91.14. The experimental projected ranges are ~2% larger than the TRIM 91.14 prediction. Previous projected range measurements of $^{13}C^+$ implantations into germanium (similar mass), are ~10% larger than the TRIM 91.14 predictions for implantation energies $\leq$100 keV. There is still a slight asymmetry with negative skewness predicted by TRIM 91.14, but not as extreme as for $^{13}C^+$ implantations into silicon. The experimental results also show a slight asymmetry with negative skewness. Both the experimental results and theoretical prediction are, however, close to normal distributions.

Poor agreement was found between experimental and theoretical predictions for all the distribution moments of $^{13}C^+$ implantations into magnesium. The projected range and straggling parameters were found to be appreciably higher (~22% for projected range and ~32% for straggling) than the theoretically predicted values. The high statistical uncertainty and increasing background with increasing proton energy make the estimation of the accuracy of the experimental projected range and straggling parameters difficult. TRIM 91.14 predicts an asymmetric profile with a large negative skewness and a large kurtosis, while the experimental results indicate a profile close to a normal distribution. Although the third and fourth moments are less significant, as there are already large discrepancies in the first two moments, it should be noted that TRIM 91.14 again seems to overestimates the negativity of the skewness as well as the kurtosis.

Good agreement was found between the experimental distribution moments of $^{13}C^+$ implantations into stainless steel and the theoretical calculations of TRIM 91.14. Asymmetry with negative skewness is predicted by TRIM 91.14 but not as extreme as for the implantations into silicon. Experimental results also indicate a slight asymmetry with negative skewness and both experimental and theoretical results are close to normal distributions. It seems that the accuracy by which the third and fourth moments are predicted by TRIM 91.14 gets better with increasing target mass.

108

As very few results of implantation distributions in the literature give more than the projected range, it is not possible to compare the higher moments of the experimental results of this study with previous work. For $^{13}C^+$ implantations into silicon and gallium arsenide the conclusion can be drawn that the nuclear reaction analysis performed in this study gave accurate projected ranges. Although no previous $^{13}C^+$ implantations into stainless steel are reported, there is excellent agreement of all the experimental distribution moments with TRIM 91.14 predictions. However, because of the large discrepancies between experimental and theoretical projected ranges and straggling values, the same can not be said for the $^{13}C^+$ implantations into magnesium. The stopping power values of magnesium are most probably erroneous. Because of the steep increase in the background with increasing analysing ion energy, the statistics were also poor.

The discrepancies between the experimental and theoretical skewness and kurtosis values found for the lighter targets should be experimentally investigated. This investigation should also be expanded to include lighter implantation ions and higher implantation energies.

7.2   THE $^{27}Al(p,\gamma)^{28}Si$ REACTION ANALYSIS

Depth distribution profiles of $^{27}Al^+$ implantations into silicon, gallium arsenide, magnesium and stainless steel were obtained by employing nuclear resonance reactions. There were no significant differences between ion distributions implanted at room temperature and at liquid nitrogen temperature.

Except for the third moment, good agreement was obtained between all the experimentally measured and theoretically predicted moments of $^{27}Al^+$ implanted into silicon.   The average experimental projected range is ~2% larger than the TRIM 91.14 prediction.   This compares well with the experimental results of Paltemaa [86], which is about ~4% lower than the TRIM 91.14 prediction for implantation energies ≤ 100 keV.   However, in disagreement are the experimental

109

results of Crowder [84], which are ~21% lower than the TRIM 91.14 prediction for an implantation energy of 200 keV. TRIM 91.14 predicts a slight asymmetry with a negative skewness, while experimental results indicate an almost normal distribution. It would again seem that TRIM 91.14 overestimates the negativity in the skewness for the lighter mass targets. The severity of this overestimation is, however, much smaller while the kurtosis value is more correct.

Except for the projected range, all the experimental depth distribution moments, of $^{27}Al^+$ implantations into gallium arsenide, compare reasonably with the TRIM 91.14 predictions. The projected range was found to be ~9% larger than the TRIM 91.14 prediction. Larger deviation from theoretical values are found for experimental results of $^{27}Al^+$ implantations into similar mass targets [92] ($^{27}Al^+$ implanted into Ni and Cu) at energies ≤100 keV. The experimental results for Ni targets are ~20% larger and those for Cu are ~16% larger than the TRIM 91.14 predictions. On the other hand, the experimental results for $^{27}Al^+$ implanted into germanium are ~7% lower than the TRIM 91.14 predictions for implantation energies ≤100 keV. Experimental results and theoretically predicted third and fourth moments indicated a close to normal distribution with a slight positive moment.

For $^{27}Al^+$ ions implanted into magnesium, both the experimental projected range and straggling parameters were found to be appreciably higher (14% for projected range and 21% for straggling) than expected. This deviation is assumed to be due to erroneous stopping power values for magnesium. The stopping power of magnesium was experimentally obtained with Rutherford Backscattering and found to be around 17% lower than that given in the Ziegler tables [96]. Experimental skewness values indicated a close to normal distribution, while TRIM 91.14 predicted an asymmetric distribution with a negative skewness. The overestimation of the negativity of the skewness for light mass targets, although not as severe as for the $^{13}C^+$ implantations, is again illustrated. The theoretical kurtosis value is, however, closer to the experimental value.

The experimentally obtained distribution moments of $^{27}Al^+$ ions implanted into stainless steel are in good agreement with the theoretical predictions of TRIM 91.14.

The experimental projected range is ~1% larger than the TRIM 91.14 prediction. Larger differences are found between TRIM 91.14 predictions and experimental results of $^{27}Al^+$ implantation into similar mass targets [92] ($^{27}Al^+$ implanted into Ni and Cu). The experimental results for the Ni are ~20% larger and those for Cu are ~16% larger than the TRIM 91.14 predictions. Experimental results and TRIM 91.14 predicted third and fourth moments indicate a close to normal distribution with a slight positive moment.

The experimental projected ranges of $^{27}Al^+$ implanted silicon obtained in this study compare well with previous results. The experimental projected ranges of $^{27}Al^+$ implanted gallium arsenide and stainless steel also compare well with previous results of $^{27}Al^+$ implantations into similar mass targets. Although there is a larger than experimental error difference between the experimental and TRIM 91.14 predicted projected range of $^{27}Al^+$ implanted magnesium, the difference is probably explained by erroneous stopping power values for magnesium. The discrepancies found between the experimentally obtained and TRIM 91.14 predicted third and fourth moments of the lighter mass targets are smaller than those found for $^{13}C^+$ implantations.

111

CHAPTER 8

REFERENCES

[1]   H.E. Schiøtt, Matt. Fys. Medd. Kgl. Vid. Selsk. 35 no. 9, 1966.

[2]   J. Lindhard, M. Scharff and H.E. Schiøtt, Matt. Fys. Medd. Kgl. Dan. Vid. Selsk. 33 no. 14, 1963.

[3]   J.F. Ziegler, "Ion Implantation Science and Technology", Academic Press Inc., publ. Harcourt, Brace, Jovanoviech, 1984.

[4]   G. Carter and W.A. Grant, "Ion Implantation of Semiconductors", eds. A.H.W. Beck, and J. Lamb, Edward Arnold, London, 1976, p42.

[5]   W.K. Chu, W.J. Mayer and M.A. Nicolet, "Backscattering Spectrometry", Academic Press, London, 1978.

[6]   H.H. Andersen and J.F. Ziegler, "Hydrogen Stopping Powers and Ranges in All Elements", vol. 3, Pergamon Press, New York, 1977.

[7]   O.B. Firsov, Zh. Eksp. Teor. Fiz. 32, 1957, p1464.

[8]   J. Lindhard, Matt. Fys. Med. Kgl. Dan. Vid. Selsk. 28 no. 8, 1954.

[9]   C. Varelas, and J.P. Biersack, Nucl. Instr. and Meth. 79, 1970, p213.

[10]   J. Lindhard and M. Scharff, Kgl. Dan. Vid. Selsk. Mat. Fys. Medd. 27 no. 15, 1953.

[11]   E. Bonderup and P. Hvelplund, Phys. Rev. A4, 1971, p562.

[12]   W.K. Chu, Phys. Rev. A13, 1976, p2057.

[13]   F. Besenbacher, J.U. Andersen and E. Bonderup, Nucl. Instr. and Meth. 168, 1980, p1.

[14]   M. Luomajärvi, A. Fontell and M. Bister, "Ion Beam Surface Layer Analysis", eds. O. Meyer, G. Linker and F. Käppeler, Plenum Press, New York, 1976, p75.

[15]   G.E. Hoffman and D. Powers, Phys. Rev. A13, 1976, p2042.

[16]   E. Friedland and J.M. Lombaard, Nucl. Instr. and Meth. 163, 1979, p523.

[17]   E. Friedland and J.M. Lombaard, Nucl. Instr. and Meth. 168, 1980, p25.

[18]   E. Friedland and C.P. Kotze, "Nucl. Instr. and Meth. 191, 1981, p490.

[19]   J.F. Ziegler, J.P. Biersack and U. Littmark, "The Stopping and Range of Ions in Solids", vol. 1, ed. Ziegler, J.F., Pergamon Press, New York, 1985.

[20]   J.R. Bird, B.L. Campbell and P.B. Price, Atomic Energy Rev. 12, 1974, p481.

[21]   J.B. Blatt and V.F. Weisskopf, "Theoretical Nuclear Physics", John Wiley and Sons Inc., New York, 1952.

[22]   W.E. Meyerhof, "Elements of Nuclear Physics", McGraw-Hill, New York, 1967.

[23]   R.D. Evans, "The Atomic Nucleus", McGraw-Hill, New York, 1955.

[24]   L.C. Feldman. and J.W. Mayer, "Fundamentals of Surface and Thin Film Analysis", Elsevier Science Publishing Co. Inc., New York, 1986.

[25]   G. Amsel and D. Samuel, Anal. Chem. 39, 1967, p1689.

[26]   E.A. Wolicki, "References to Activation and Prompt Radiation Analysis: Material Analysis by Means of Nuclear Ractions", in "New Uses of Ion Accelerators", ed. J.F. Ziegler, Plenum Press, New York, 1975.

[27]   B. Maurel, G. Amsel and J.P. Nadai, Nucl. Instr. and Meth. 197, 1982, p1.

[28]   G. Amsel and B. Maurel, Nucl. Instr. and Meth. 218, 1983, p183.

[29]   E. Friedland, Nucl. Instr. and Meth. 150, 1978, p301.

[30]   G. Amsel and D Samuel, J. Phys. Chem. Solides 23, 1962, p1707.

[31]   J.G. Skofronick, J.A. Ferry, D.W. Palmer, G. Wendt and R.G. Herb, Phys. Rev. A135, 1964, p1429.

[32]   J.M. Morris and T.R. Ophel, Nucl. Instr. and Meth. 40, 1966, p245.

[33]   G. Amsel and E. d'Artemare, IEEE Trans. Nucl. Sci. NS-14 no. 1, 1967, p189.

[34]   L. Sandor, Atoki Közlemények (Debrecen, Hungary) 18, 1976, p97.

[35]   R.O. Bondelid and C.A. Kennedy, Phys, Rev. 115, 1959, p1601.

[36]   R.O. Bondelid and J.W. Butler, Phys. Rev. 130, 1963, p1078.

[37]   A. Barcz, A. Bienkowski, A. Turos, L. Wielunski and L. Zemlo, Nucl. Instr. and Meth. 113, 1973, p413.

[38]   M.R. Wormald and J. Takacs, Nucl. Instr. and Meth. 114, 9174, p263.

[39]   G. Amsel, J.P. Nadai, E. d'Artemare, D. David, E. Girard, and J. Moulin, Nucl. Instr. and Meth. 92, 1971, p418.

[40]   G. Amsel, E. d'Artemare and E. Girard, Nucl. Instr. and Meth. 191, 1981, p189.

114

[41]   G. Amsel, E. d'Artemare and E. Girard, Nucl. Instr. and Meth. 205, 1983 a, p5.

[42]   M. Zinke-Allmang, S. Kalbitzer and M. Weiser, Nucl. Instr. and Meth. B15, 1986, p563.

[43]   H.J. Rose, F. Riess and W. Trost, Nuclear Physics 21, 1960, p367.

[44]   R.E. Segel, J.W. Daughtry and J.W. Olness, Physical Review 123 no. 1, 1961, p194.

[45]   R.O. Bondelid and C.A. Kennedy, Physical Review 115 no. 6, 1959, p1601.

[46]   H.J. Rose, Nuclear Pysics 19, 1960, p113.

[47]   H.J. Rose, W. Trost and F Riess, Nuclear Physics 12, 1959, p511.

[48]   E.K. Warburton and W.T. Pinkston, Phys. Rev. 118 no. 3, 1960, p733.

[49]   E.K. Warburton, Phys. Rev. 113 no. 2, 1959, p595.

[50]   H.H. Woodbury, R.B. Day and A.V. Tollestrup, Phys. Rev. 92 no. 5, 1953, p1199.

[51]   A.A. Strassenburg, R.E. Hubert, R.W. Krone and F.W Prosser, Bull. Am. Phys. Soc. 3, 1958, 372.

[52]   M.A. Meyer and N.S. Wolmarans, Nuclear Physics A136, 1969, p663.

[53]   P.M. Endt and C. van der Leun, Nuclear Physics A310, 1978, p235.

[54]   J.M. Donhowe, J.A. Ferry, W.G. Mourad and R.G. Herb, Nuclear Physics A102, 1967, p383.

[55]   Y.P. Antoufiev, L.M. El-Nadi, D.A.E. Darwish, O.E. Badawy and P.V. Sorokin, Nuclear Physics 46, 1963, p1.

[56]   L. Simons, K.E. Nysten, M.Koskelin, O. Siltanen, E. Spring and G, Wendt, Phys. Lett. 3 no. 6, 1963, p306.

[57]   R.E. Azuma, L.E. Carlson, A.M. Charlsworth, K.P. Jackson, N. Anyas-Weiss and B. Lalavic, Can. J. Phys 44, 1966, p3075.

[58]   T. R. Ophel and D.R. Osgood, Proc. Phys. Soc. 85, 1965, p1093.

[59]   N.A.S. Crowther, Private communication.

[60]   J.A. Davies, J. Friesen and J.D. McIntyre, Can. J. Chem. 38, 1960, p1526.

[61]   J.A. Davies, J.D McIntyre and G.A. Dims, Can. J. Chem. 39, 1961, p611.

[62]   F. Besenbacher, J. Bøttinger, T. Laursen, P. Loftager and W Möller, Nucl. Instr. and Meth. 170, 1980 b, p183.

[63]   P. Oberschachtsiek, V. Schüle, R. Günzler, M. Weiser and S. Kalbitzer, Nucl. Instr. and Meth. B45, 1990, p20.

[64]   S. Kalbitzer and H. Oetzman, Rad. Effects 47, 1980, p57.

[65]   J. Berthold and S. Kalbitzer, Phys. lett. A91, 1982, p37.

[66]   D.J. O'Connor, B.W. Farmery, D. Chivers and M.W. Thompson, Nucl. Instr. and Meth. 178, 1980, p517.

[67]   D.J. O'Connor, Nucl. Instr. and Meth. 196, 1982, p493.

[68]   H.H. Andersen, J. Bøttiger and H. Wolder Jørgensen, Appl. Phys. Lett. 26 no. 12, 1975, p678.

[69]   F. Jahnel, H. Ryssel, K. Hoffmann, K. Müller, J. Biersack and R. Henkelmann, Nucl. Instr. and Meth. 182/183, 1981, p223.

[70]   P.F.P. Fichtner, M. Behar, C.A. Olivieri, R.P. Livi, J.P. De Souza, F.C. Zawislak, D. Fink and J.P. Biersack, Rad. Effects Lett. 87, 1986, p191.

[71]   K.B. Winterbon, P. Sigmund and J.B. Sanders, Kgl. Dansk. Vis. Selsk. Matt. Fys. Medd. 37 no.14, 1970.

[72]   G. Moliére, Z. Naturf 2a, 1947, p133.

[73]   W. Lenz, Z. Physik 77, 1932, p713.

[74]   H. Jensen, Z Physik 77, 1932, p722.

[75]   J.P. Biersack and J.F. Ziegler, in Springer Series in Electro-Physics vol 10: "Ion Implantation Techniques", eds. H. Ryssel and H. Glawischnig, Springer, Berlin, 1982.

[76]   J.F. Gibbons, W.S. Johnson and S.W. Mylroie, "Projected Range Statistics", 2 ed., Hutchinson and Ross, Stroudsberg, 1975, p22.

[77]   P.F.P. Fichtner, M. Behar, D. Fink, P. Goppelt and P.L. Grande, Nucl. Instr. and Meth. B64, 1992, p668.

[78]   P.L. Grande, F.C. Zawislak, D Fink and M. Behar, Nucl. Instr. and Meth. B61, 1991, p282.

[79]   P.L. Grande, P.F.P. Fichtner. M. Behar and F.C. Zawislak, Nucl. Instr. and Meth. B33, 1988, p122.

[80]   P.F.P. Fichtner, M. Behar, C.A. Olivieri, R.P. Livi, J.P. De Souza, F.C. Zawislak, J.P. Biersack and D. Fink, Nucl. Instr. and Meth. B28, 1987, p481.

[81]   W.K. Chu, R.H. Kastl and P.C. Murley, Rad. Effects 47, 1980, p1.

[82]   W.D. Wilson, L.G. Haggmark and J.P. Biersack, Phys. Rev. B15, 1977, p2458.

[83]   K.B. Winterbon, "Ion Implantation Range and Energy Deposition Distributions, vol. 2, Plenum Press, New York, 1975.

[84]   B.L. Crowder, J. Electrochem. Soc. 118 no. 6, 1971, p943.

[85]   W.S. Johnson and J.F. Gibbons, "Projected Range Statistics in semiconductors", Stanford University Bookstore, 1970.

[86]   R. Paltemaa, J. Räisänen, M. Hautala and A. Anttila, Nucl. Instr. and Meth. 218, 1983, p785.

[87]   J. Lindhard, V. Nielsen and M. Scharff, Matt. Fys. Medd. Kgl. Dan. Vid. Selsk. 36 no. 10, 1968.

[88]   H.E. Schiøtt, Rad. Effects 6, 1970, p107.

[89]   W.D. Wilson and Y.S. Kim, J. Chem. Phys. 56, 1972, p3122.

[90]   M. Bister, M. Hautala and M. Jäntti, Rad. Effects 42, 1979, p201.

[91]   M. Hautala, Rad. Effects 51, 1980, p35.

[92]   M. Luomajärvi, J. Keinonen, M. Bister and A. Anttila, Phys. Rev. B18 no. 9, 1978, p4657.

[93]   J. Keinonen, M. Hautala, M. Luomajärvi, A. Anttila and M. Bister, Rad. Effects 39, 1978, p189.

[94]   U. Littmark and J.F. Ziegler, "The Stopping and Ranges of Ions in Matter", vol. 6, ed. J.F. Ziegler, Pergamon Press, New York, 1980.

[95]   K.H. Ecker, M.P. Macht and V. Naundorf, Nucl. Instr. and Meth. B15, 1986, p66.

[96]   J.F. Ziegler,"The Stopping and Ranges of Ions in Matter", vol 4, Pergamon Press, New York, 1977.

CHAPTER 9

PUBLICATIONS

(1) E. Friedland, M. Hayes, S. Kalbitzer and P. Oberschachtsiek, "Range parameters of ^{13}C implants in semiconductor and metal targets", Nucl. Instr. and Meth. B 85, 1994, p272.

(2) M. Hayes, E. Friedland, S. Kalbitzer, B. Hartman and S. Fabian, "Depth profiling of $^{27}Al^+$ implanted samples by NRA", Accepted for publication in Nucl. Instr. and Meth. B, May 1995.

Range parameters of ^{13}C implants in semiconductor and metal targets

E. Friedland *, M. Hayes

Department of Physics, University of Pretoria, Pretoria 0002, South Africa

S. Kalbitzer, P. Oberschachtsiek

Max-Planck-Institut für Kernphysik, Postfach 10 39 80, D-69029 Heidelberg, Germany

Silicon, gallium arsenide and stainless steel samples were implanted with 150 keV ^{13}C ions at room and liquid-nitrogen temperatures. The depth distributions were analyzed by making use of the narrow ^{13}C(p,γ)-resonance at 1.75 MeV. The experimentally determined moments of the depth distributions for gallium arsenide and stainless steel are in reasonable agreement with theoretical predictions. In the case of silicon the agreement is less satisfactory, especially as far as the third and fourth moments are concerned. The experimental results indicate a symmetrical implantation profile in silicon, whilst from theoretical calculations a strongly skewed distribution is expected.

1. Introduction

As range parameters of implanted ions are of considerable theoretical interest and of importance for many applications in metallurgy and microelectronics, many experimental determinations of implantation profiles are found in the literature [1–5]. Although results generally compare reasonably well with TRIM calculations [6], significant discrepancies between theory and experiment have been reported for a variety of medium to heavy ions implanted into some light mass targets. Relatively large deviations from TRIM-predictions have been reported for range parameters in silicon at low energies, whilst at higher energies reasonable agreement was found [7]. Contrary to these results, where discrepancies only exist at low energies, in other light target materials the range parameters deviate also at higher energies from theoretical predictions. Such energy independent behaviour is reported for beryllium [8], boron, carbon [9] and silicon carbide [10].

Relatively few results of range parameters for light ion implantations are found in the literature. Ranges of carbon ions in silicon and germanium are reported for energies between 20 and 100 keV in ref. [11]. For silicon targets these workers observed smaller ranges than expected from theory, whilst reasonable agreement was found for the heavier germanium targets. In

order to check whether this indicates a general trend for carbon ions as far as target mass is concerned, we determined range parameters for 150 keV ^{13}C ions in silicon, stainless steel and gallium arsenide.

2. Experimental

Polycrystalline stainless steel as well as single crystals of silicon and gallium arsenide were used as samples. Implantations with ^{13}C ions at 150 keV and with fluences in the 10^{16} cm^{-2} range were performed both at room temperature and at liquid nitrogen temperature. Some of the silicon samples had been pre-implanted with 300 keV Ne ions at a fluence of 10^{15} cm^{-2} in order to amorphize the surface region. Dose rates were kept at 10^{13} ions cm^{-2} s^{-1} in all cases and the single crystals were tilted 7° relative to the $\langle 100 \rangle$ orientation to limit possible channeling effects.

Depth profiles were analyzed by making use of the ^{13}C(p, γ)^{14}N resonance at 1.75 MeV. This resonance has a width of 75 eV and a rather large cross section of approximately 340 mb. The excited 9.17 MeV level in ^{14}N decays with a 90% probability directly to the ground state. This has the important advantage, that the lower and upper energy discriminators of the γ-detector can be adjusted at relatively high energies where the background is low. However, the counting efficiency of the detector is rather poor at this energy. In order to optimize the signal-to-noise ratio, the energy window was set between 8.0 and 9.3 MeV to detect the photo peak together with its two escape peaks.

* Corresponding author, phone +27 12 420 2453, fax +27 12 342 4143.

Measurements were performed at the 3 MV Pelletron accelerator of the Max-Planck-Institut für Kernphysik in Heidelberg and at the 2.5 MV Van de Graaff accelerator of the University of Pretoria. In Heidelberg use was made of the low-level γ-ray detection system, which employs a 10 inch NaI(Tl) scintillation detector. Furthermore, this accelerator is equipped with an automatic energy scanning system [12] with a channel width much smaller than the beam spread of approximately 600 eV. In Pretoria the detection system consists of a 5 cm intrinsic Ge-diode. Energy scanning is done manually by adjusting the field of the analyzing magnet in steps of 1 keV, which is in accordance with the energy width of the proton beam. An analyzing beam current of 200 to 500 nA was used in both experiments with beam spot diameters of 1 and 4 mm in Heidelberg and Pretoria respectively.

3. Data analysis and results

Typical yield curves for implanted and unimplanted silicon targets as a function of proton energy are shown in fig. 1. The slightly higher background of the implanted sample is the result of a large number of weakly populated and overlapping states in the vicinity of the 9.17 MeV level of the ^{14}N compound nucleus. A slight energy dependence of this contribution is taken into account by adding a linear energy term to the fit

Fig. 2. Resolution functions (FWHM) for silicon, stainless steel and gallium arsenide as a function of depth. A proton beam energy spread of 600 eV was taken into account and Bohr straggling was assumed.
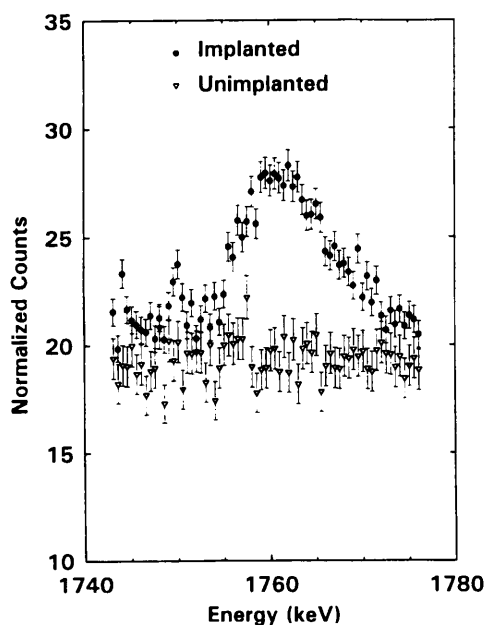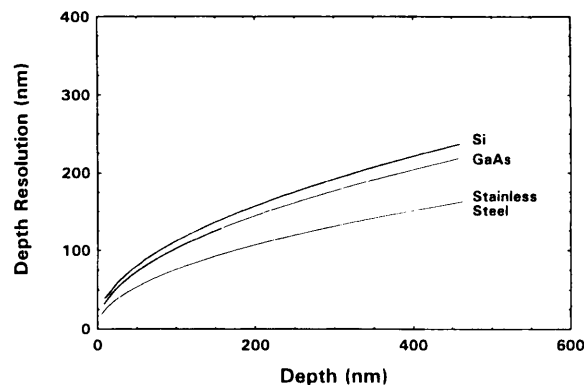

Fig. 1. Yield curves as a function of proton energy for silicon targets before and after implantation of 150 keV ^{13}C ions with a fluence of 2×10^{16} cm^{-2} at room temperature.

equation used for the background correction. To determine the position of the surface, yield curves were measured for natural carbon targets, which were also used to determine the experimental energy resolution. Energies were converted to depths by making use of the stopping power values of ref. [13], applying Bragg's rule if appropriate. The effect of the instrumental resolution and energy straggling is corrected for by using a deconvolution algorithm described in ref. [14]. As is evident from fig. 2, the effect of straggling is quite important for proton beams because of its large contribution compared to the relatively small energy loss. The figures along the ordinate are obtained by quadratic summation of the instrumental energy resolution and the energy spread (FWHM) of the analyzing beam, which is then converted to a depth scale. In these calculations it was assumed that energy straggling is adequately described by the Bohr estimate, which should be valid in this energy range. The experimental results are compared with theoretical predictions. These were obtained by computing approximately 10^5 ion trajectories, using version 91.14 of the TRIM code. It should be noted that the results of previous TRIM versions (e.g. TRIM 85) differ from the one used here by up to 3, 6, 10 and 10% for the first four range moments respectively.

3.1. Silicon

Silicon targets were implanted with a fluence of 2×10^{16} $^{13}C^+$ cm^{-2} at liquid-nitrogen and room temperature. Some of the samples were pre-implanted with a dose of 10^{15} Ne$^+$ cm^{-2} at an energy of 300 keV. Similar depth profiles were observed, independent of whether samples were pre-implanted (a-Si) or not (c-Si). Channeling effects are apparently not important, which

IV. THIN FILMS

was expected for a dose of at least an order of magnitude higher than needed for complete amorphization. Furthermore the distributions found for samples implanted at room temperature did not differ significantly from those implanted at liquid-nitrogen temperature. Comparing the results with TRIM calculations, one finds both the projected range and straggling parameters slightly smaller than expected, although this is not very significant in the case of straggling because of the statistical uncertainties. Somewhat more serious seems to be the discrepancy observed for the third and fourth moments of the distributions. Whilst theory predicts a distinctly asymmetric profile, the values for skewness (γ) and kurtosis (β) of the experimental distributions are almost Gaussian ($\gamma = 0$, $\beta = 3$). It must, however, be borne in mind that, particularly for silicon, the depth resolution at the position of the maximum compares rather unfavourably with the straggling width. This might render the higher moments somewhat less reliable. The experimental results are shown in fig. 3 together with the theoretical predictions.

3.2. Gallium arsenide

Gallium arsenide samples were implanted at room temperature with a fluence of 5×10^{16} $^{13}C^+$ cm^{-2}. The experimental depth profiles agree reasonably well with theoretical predictions as is evident from fig. 4a. By comparing the distribution moments listed in table 1, all of them agree within experimental error with the TRIM predictions. The experimental straggling width is found to be approximately 15% larger than the theoretical value, but this has to be compared with an exceptionally large statistical uncertainty of 25% for this particular distribution.

3.3. Stainless steel

The stainless steel samples were implanted at room temperature with a fluence of 5×10^{16} $^{13}C^+$ cm^{-2}. Good agreement between the experimental distribu-
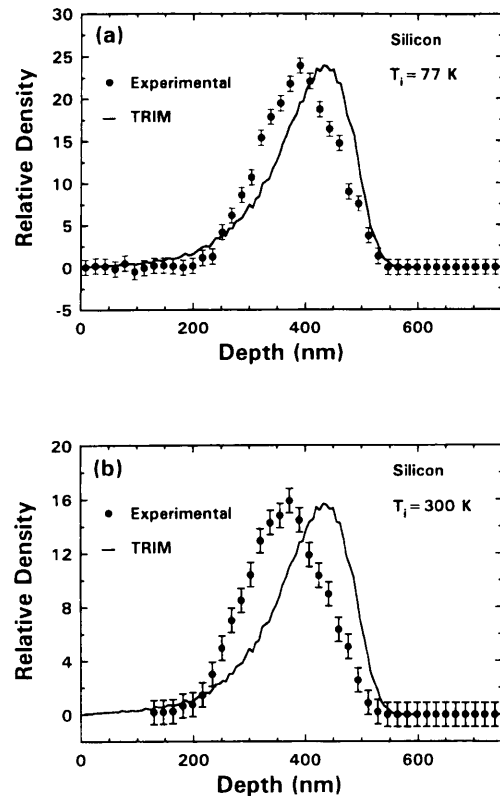

Fig. 3. Experimental depth profiles of 150 keV ^{13}C ions implanted into silicon compared with TRIM simulations. Fig. 3a shows the results for a sample implanted at liquid nitrogen temperature, whilst fig. 3b exhibits the results of an implantation at room temperature. The implanted fluence was in both cases 2×10^{16} ions cm^{-2} and the dose rate was approximately 10^{13} ions cm^{-2} s^{-1}.

tions and the theoretical predictions are found. The moments of the distributions are listed in table 1 and all of them are in good agreement with TRIM calculations. The depth profile is depicted in fig. 4b together with the TRIM simulation. In view of the good agreement it seems unlikely that channeling effects in the

Table 1
Moments of the experimental depth distributions, $R^{(i)}$, $i = 1$–4, for 150 keV ^{13}C implantations into silicon, gallium arsenide and stainless steel. For comparison the TRIM results are printed in brackets. The quoted errors are 1σ values.

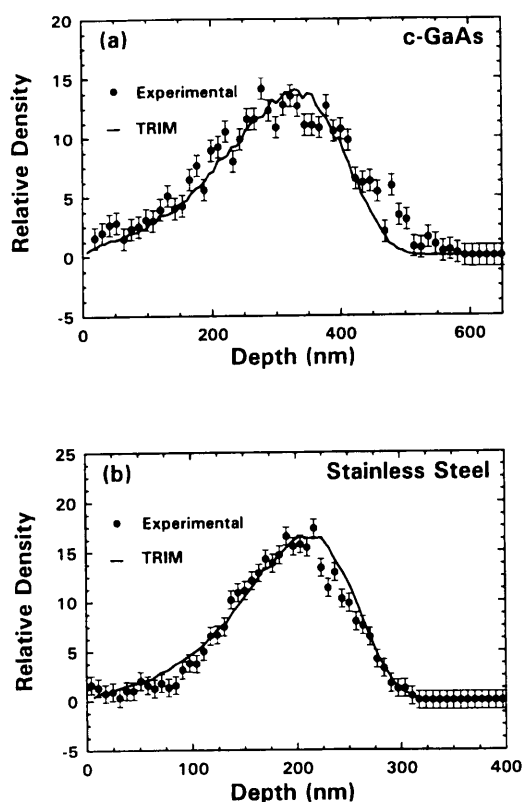| Sample	$R^{(1)}$ [nm]	$R^{(2)}$ [nm]	$R^{(3)}$	$R^{(4)}$
a-Si (RT)	357 ± 21 [391]	71 ± 14 [83]	-0.2 ± 0.2 [-1.1]	2.8 ± 0.5 [4.7]
c-Si (RT)	364 ± 21 [391]	63 ± 17 [83]	0.0 ± 0.2 [-1.1]	2.4 ± 0.5 [4.7]
a-Si (LN)	382 ± 18 [391]	67 ± 14 [83]	-0.4 ± 0.2 [-1.1]	3.8 ± 0.5 [4.7]
c-Si (LN)	378 ± 22 [391]	67 ± 20 [83]	-0.3 ± 0.2 [-1.1]	2.9 ± 0.5 [4.7]
GaAs (RT)	297 ± 13 [287]	112 ± 28 [97]	-0.2 ± 0.2 [-0.5]	2.6 ± 0.3 [2.9]
Steel (RT)	186 ± 7 [183]	57 ± 13 [59]	-0.6 ± 0.2 [-0.5]	3.4 ± 0.4 [3.2]

Fig. 4. Experimental depth profiles of 150 keV ^{13}C ions implanted at room temperature with fluences of 5×10^{16} cm^{-2} and a dose rate of approximately 10^{13} cm^{-2} s^{-1} compared with TRIM simulations. The results for stainless steel are shown in (b) and those of gallium arsenide in (a).

polycrystalline structure of the sample play a significant role. The average grain size was determined as 7 μm by electron scanning microscopy.

4. Conclusions

The range moments listed in table 1 are calculated according to definitions used in the TRIM code 91.14. The first two moments have the usual meaning of mean depth and standard deviation, whilst the third and fourth moments are defined as follows:

$$R^{(3)} = \sum \left(X_i - R^{(1)} \right)^3 Y_i / \sum (Y_i)(R^{(2)})^3$$

and

$$R^{(4)} = \sum \left(X_i - R^{(1)} \right)^4 Y_i / \sum (Y_i)(R^{(2)})^4$$

Errors quoted are calculated from asymptotic expressions of standard deviations of the moments $R^{(i)}$, which are treated as parameters of a regression function describing the ion distribution. Furthermore the experimental uncertainty of the surface position is included in the error stated for the first moment.

The four moments show the following behaviour: Projected ranges and longitudinal straggling parameters of implantation profiles for ^{13}C ions at relatively large reduced energies (15 > ε > 5) in gallium arsenide and stainless steel are in reasonable agreement with TRIM predictions, whilst for silicon somewhat smaller values are observed. As far as the third and fourth moments of the distributions are concerned, satisfactory agreement is only found for the gallium arsenide and stainless steel samples. In silicon the shape of the depth profile is found to be close to that of a normal distribution, whilst TRIM predicts a strongly asymmetric profile.

References

[1] F. Besenbacher, J. Bøttinger, T. Laursen, P. Loftager and W. Möller, Nucl. Instr. and Meth. 170 (1980) 183.

[2] H. Oetzmann and S. Kalbitzer, Radiat. Eff. 47 (1980) 57.

[3] J. Berthold and S. Kalbitzer, Phys. Lett. A 91 (1982) 37.

[4] M. Behar, P.F.P. Fichtner, C.A. Olivieri, J.P. de Souza, F.C. Zawislak and J.P. Biersack, Nucl. Instr. and Meth. B 6 (1985) 453.

[5] P. Oberschachtsiek, V. Schüle, R. Günzler, M. Weiser and S. Kalbitzer, Nucl. Instr. and Meth. B 45 (1990) 20.

[6] J.F. Ziegler, J.P. Biersack and U. Littmark, in: Stopping and Ranges of Ions in Solids, vol. 1, ed. J.F. Ziegler (Pergamon, New York, 1985).

[7] P.F.P. Fichtner, M. Behar, C.A. Olivieri, R.P. Livi, J.P. de Souza, F.C. Zawislak and J.P. Biersack, Nucl. Instr. and Meth. B 28 (1987) 481.

[8] P.L. Grande, M. Behar, J.P. Biersack and F.C. Zawislak, Nucl. Instr. and Meth. B 45 (1990) 689.

[9] P.L. Grande, F.C. Zawislak, D. Fink and M. Behar, Nucl. Instr. and Meth. B 61 (1991) 282.

[10] P.F.P. Fichtner, M. Behar, D. Fink, P. Goppelt and P.L. Grande, Nucl. Instr. and Meth. B 64 (1992) 668.

[11] R. Paltemaa, J. Räisänen, M. Hautala and A. Antilla, Nucl. Instr. and Meth. 218 (1983) 785.

[12] G. Amsel, E. d'Artemare and E. Girard, Nucl Instr. and Meth. 191 (1981) 189;
M. Zinke-Allmang, S. Kalbitzer and M. Weiser, Nucl. Instr. and Meth. B 15 (1986) 563.

[13] H.H. Andersen and J.F. Ziegler, in: The Stopping and Ranges of Ions in Matter, vol. 3, ed. J.F. Ziegler (Pergamon, New York, 1977).

[14] E. Friedland, Nucl. Instr. and Meth. 150 (1978) 301.

IV. THIN FILMS

Depth profiling of ^{27}Al$^+$ implanted samples by NRA

M. Hayes[a], E. Friedland[a], S. Kalbitzer[b], B. Hartmann[b] and S. Fabian[b]

[a]Department of Physics, University of Pretoria, Pretoria 0002, South Africa

[b]Max-Planck-Institut für Kernphysik, Postfach 10 39 80, D-69029 Heidelberg, Germany

Silicon, gallium arsenide, magnesium and stainless steel samples were implanted with 150 keV ^{27}Al$^+$ ions at room and liquid nitrogen temperatures. The implantation profiles were analysed by making use of the ^{27}Al(p,γ)^{28}Si resonance at 0.992 MeV. The experimentally determined moments of the depth distributions for silicon, gallium arsenide and stainless steel agree within the quoted experimental errors reasonably well with theoretical predictions. For magnesium, however, an approximately 25% larger projected range is observed than expected from theory, indicating that the published empirical stopping power values might be erroneous.

1. INTRODUCTION

Range parameters of implanted ions are of considerable importance for many applications in metallurgy and micro-electronics. Of the many experimentally determined profiles found in the literature [1, 2], most compare reasonably well with the theoretical predictions obtained by the TRIM code [3]. However, there are some cases where significant discrepancies between theory and experiment have been reported. Relatively large deviations from TRIM predictions have been reported for range parameters in silicon implanted at energies below 70 keV, while at higher implantation energies reasonable agreement was found [4]. Other workers have found that for beryllium [5], boron and carbon [6] and silicon carbide[7] the discrepancies in the range parameters are energy independent.

Relatively few experimental range parameters for light ion implantations are found in the literature. Ranges of carbon implants into silicon and germanium are reported for implantation energies between 20 and 100 keV [8]. These workers observed smaller ranges than predicted by theory for the silicon targets, while reasonable agreement was found for the germanium targets. Reasonable agreement between TRIM predictions and experimentally determined range parameters are reported for carbon implants into gallium arsenide and stainless steel [9]. However, this group observed deviations from theory for the third and fourth moments for carbon implants into silicon. In this contribution, range parameters for implantations of 150 keV ^{27}Al$^+$ ions into silicon, gallium arsenide, magnesium and stainless steel are compared with TRIM predictions.

2. EXPERIMENTAL

Polycrystalline stainless steel with an average grain size of 7μm as well as <100> silicon and gallium arsenide and <0001> magnesium single crystals were implanted with 150 keV ^{27}Al$^+$ ions at room and liquid nitrogen temperature. The fluence was 2x10^{16} ions cm^{-2} in the case of silicon, whilst a dose of 5x10^{16} ions cm^{-2} was implanted in all other samples. Dose rates were kept at 10^{13} ions cm^{-2} s^{-1} in all cases and the single crystals were tilted 7° relative to the surface normal to limit possible channeling effects. Depth profiles were obtained by making use of the ^{27}Al(p,γ)^{28}Si resonance at 0.992 MeV. This resonance has a width of 100 eV [10]. The excited 12.54 MeV level decays with a probability of 78% to the 1.78 MeV excited state. All the nuclear reaction analyses were performed at room temperature.

Measurements were performed at the 3 MV Pelletron accelerator of the Max-Planck-Institut für Kernphysik in Heidelberg (MPI) and at the 2.5 MV van de Graaff accelerator of the University of Pretoria (UP). In Heidelberg use was made of a low background system employing a 10 inch NaI scintillation detector. In Pretoria the detection system consists of a 5 cm intrinsic Ge-diode and a 5-

inch NaI scintillation detector. Both accelerators are equipped with automatic energy scanning systems [11, 12] with channel widths much smaller than the beam spreads of approximately 600 eV and 1 keV at Heidelberg and Pretoria respectively. An analysing beam current of 200 to 500 nA was used in both experiments with beam spot diameters of 1 mm and 4 mm in Heidelberg and Pretoria respectively. Combining results from two completely independent measurements should reduce significantly any possible systematic errors.

3. DATA ANALYSIS AND RESULTS

Yield curves for silicon targets before and after implantation as a function of proton energy are depicted in figure 1. Error bars indicate standard deviations calculated from the total counts per channel. The yield from the implanted aluminium is superposed on a background which increases with the energy of the analysing beam. The main source of this background is a large number of weak proton resonances in the silicon isotopes. As more reaction channels open up at higher energies an increasing background is observed. The energy dependence of this contribution is taken into account by adding a linear term to the fit equation used for the background correction.

The yield curve for an aluminium single crystal was used to obtain the position of the surface. This measurement was also used to determine the instrumental energy resolution at the surface of the sample. Energies were converted to depths using the stopping power values of reference [13], applying Bragg's rule for the gallium arsenide and stainless steel samples. The results are corrected for instrumental resolution and energy straggling by using a deconvolution algorithm described in reference [14]. The corrected experimental depth profiles are compared with the theoretical predictions obtained by computing range distributions for 10^5 ion trajectories. The first four range moments, corresponding to the projected range, range straggling, skewness (β) and kurtosis (γ), were calculated according to the definitions used in version 91.14 of the TRIM code. Experimental errors are calculated from asymptotic expressions of standard deviations in the moments $R^{(i)}$, which are treated as parameters of a regression function describing the ion distribution. The experimental
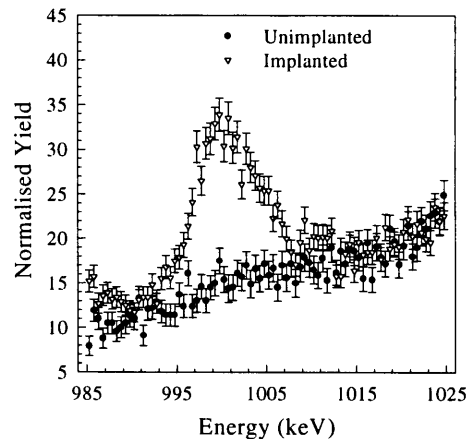

Figure 1. Yield curves of silicon samples as a function of incident proton energy before and after implantation of 2×10^{16} $^{27}Al^+$ cm^{-2} at room temperature with an energy of 150 keV.

uncertainty of the surface position is included in the calculation of the error for the first moment.

3.1. Silicon

As can be seen from figure 2, the depth profiles for samples implanted at room temperature did not differ significantly from those obtained for samples implanted at liquid nitrogen temperature. Comparing these results with those predicted by TRIM, one finds good agreement, except for the third moment. TRIM predicts a slight asymmetry with a negative skewness, while the experimental results indicate an almost Gaussian distribution ($\gamma = 0$, $\beta = 3$). Typical experimental results together with the theoretical predictions are shown in figure 2 and the moments of the distributions are listed in Table 1.

3.2. Gallium arsenide

In the case of the MPI measurements, the depth distribution obtained for the sample implanted at room temperature corresponds well with that obtained for the sample implanted at liquid nitrogen temperature, whilst the UP results indicate a slightly larger projected range at 77 K. However, in view of the statistical errors listed in Tabel 1, this difference is not of much significance. As seen from the distributions moments listed in Table 1, the higher moments agree reasonably well with the TRIM results, whilst the projected range was found to be slightly larger than expected.
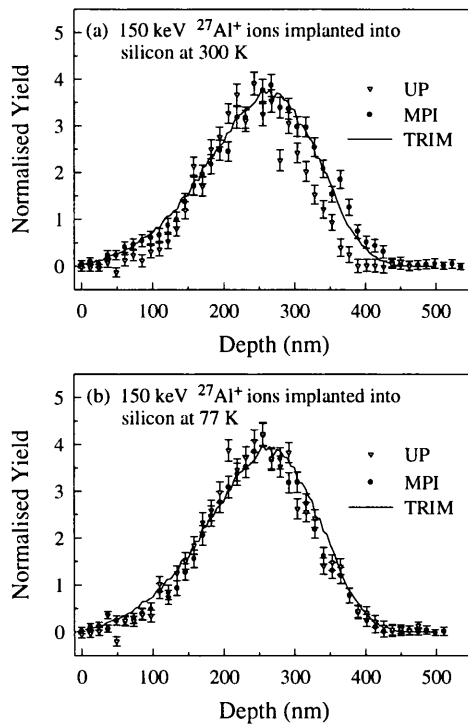
126

Figure 2. Depth profiles of 150 keV $^{27}Al^+$ ions implanted into silicon at room temperature (a) and liquid nitrogen temperature (b) compared with the TRIM prediction.
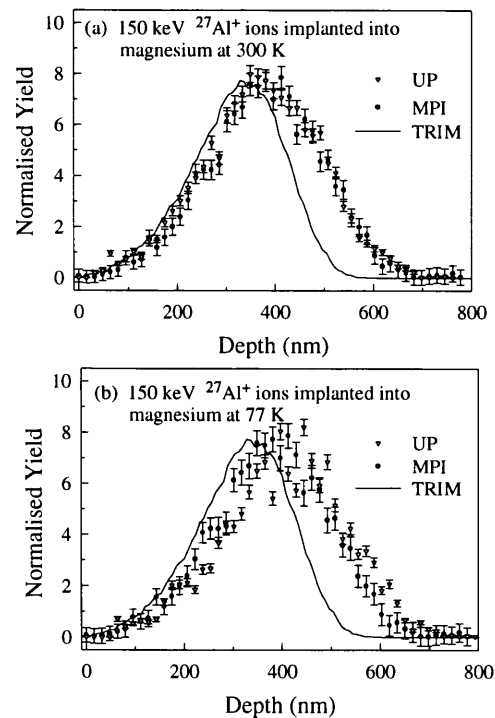

Figure 3. Depth profiles of 150 keV $^{27}Al^+$ ions implanted into magnesium at room temperature (a) and at liquid nitrogen temperature (b) compared with the TRIM prediction.

3.3. Magnesium

The experimental depth distributions obtained for the liquid nitrogen implant agree reasonably well with those obtained for room temperature, although the projected range seems to be somewhat larger for the low temperature implantation. In view of the relatively large experimental error, this difference is probably insignificant. Comparing the results with TRIM predictions, one finds that both the projected range and straggling parameters are appreciably higher than expected. The projected ranges for the liquid nitrogen and room temperature implants are found to be respectively 29% and 20% larger than the theoretical estimate, which is far outside the experimental error. Experimental straggling widths were found to be 22% and 28% larger than predicted, but this has to be compared with a large statistical uncertainty of approximately 20%. It is obvious from figure 3 that the experimental distributions are much broader than expected from TRIM simulations. That these discrepancies are due to channeling is rather unlikely, as the lattice order is

strongly distorted in metals after high dose implantations. Furthermore, one would then expect a highly skewed distribution with a positive third moment [15], which is not observed. Probably the observed deviations from the TRIM estimate are due to erroneous stopping power values. In this respect it is worth noting, that both the stopping powers of protons [13] and heavy ions [16] used in the analysis are based on interpolations between neighbouring elements, as no experimental data for magnesium were available. The experimental distribution moments and TRIM predictions are given in Table 1.

3.4. Stainless steel

The samples were cut from type 304 stainless steel rods, containing 10% Ni, 18% Cr and 3% Mo. Similar depth profiles were observed, independent of whether the sample was implanted at room or liquid nitrogen temperature. The distribution moments are listed in Table 1 and good agreement between the experimental results and the TRIM predictions are found.

127

Table 1

Experimental range moments for 150 keV $^{27}Al^+$ ions implanted into silicon, gallium arsenide, magnesium and stainless steel at liquid nitrogen and room temperatures compared with TRIM simulations. The experimental results are obtained by simultaneously fitting the MPI and UP implantation profiles. The quoted errors are 2σ values.

Sample	$R^{(1)}$ (nm)		$R^{(2)}$ (nm)		$R^{(3)}$		$R^{(4)}$	
	EXP	TRIM	EXP	TRIM	EXP	TRIM	EXP	TRIM
Si - 300 K	241 ± 12	242	62 ± 14	77	0.04 ± 0.19	-0.30	2.66 ± 0.57	2.80
Si - 77 K	247 ± 12	242	72 ± 13	77	-0.01 ± 0.14	-0.30	2.87 ± 0.37	2.80
GaAs - 300 K	183 ± 9	170	70 ± 12	76	0.01 ± 0.11	0.05	2.54 ± 0.30	2.50
GaAs - 77 K	195 ± 9	170	68 ± 12	76	-0.08 ± 0.13	0.05	2.56 ± 0.35	2.50
Mg - 300 K	371 ± 16	314	120 ± 21	95	-0.13 ± 0.15	-0.35	2.84 ± 0.42	2.85
Mg - 77 K	404 ± 17	314	123 ± 23	95	-0.14 ± 0.16	-0.35	2.73 ± 0.46	2.85
Ssteel - 300 K	103 ± 7	105	39 ± 10	45	-0.01 ± 0.48	0.06	2.70 ± 0.48	2.51
Ssteel - 77 K	104 ± 5	105	40 ± 7	45	0.08 ± 0.13	0.06	2.70 ± 0.38	2.51

4. CONCLUSIONS

The experimental range moments given in Table 1 are the final results obtained by combining the MPI and UP data. Experimental projected ranges and straggling parameters of the implantation distribution of $^{27}Al^+$ in silicon, gallium arsenide and stainless steel are in reasonable agreement with predictions by TRIM, independent of whether the samples were implanted at room or liquid nitrogen temperature. For magnesium significant deviations from the TRIM simulation are observed, which indicate that published energy loss data might be unreliable. The third and fourth moments of the experimental distributions are in all cases corresponding to nearly gaussian distributions, while TRIM predicts slightly asymmetric profiles for the light elements.

ACKNOWLEDGEMENTS

REFERENCES

[1] F. Besenbacher, J. Bøttinger, T. Laursen, P. Loftager and W. Möller, Nucl. Instr. and Meth. 170 (1980) 183.

[2] H Oetzmann and S Kalbitzer, Radiat. Eff. 47 (1980) 57.

[3] J.F. Ziegler, J.P. Biersack and U. Littmark, in : Stopping and ranges of ions in solids, vol. 1, ed. J.F. Ziegler (Pergamon, New York, 1985).

[4] P.F.P Fichtner, M. Behar, C.A. Oliviera, R.P. Livi, J.P. de Souza, F.C. Zawislak and J.P.Biersack, Nucl. Instr. and Meth. B 28 (1987) 481.

[5] P.L. Grande, M. Behar, J.P. Biersack and F.C Zawislak, Nucl. Instr. and Meth. B 45 (1990) 689.

[6] P.L. Grande, F.C. Zawislak, D. Fink and M. Behar, Nucl. Instr. and Meth. B 61 (1991) 282.

[7] P.F.P. Fichtner, M. Behar, D. Fink, P. Goppelt and P.L. Grande, Nucl. Instr. and Meth. B 64 (1992) 668.

[8] R. Paltemaa, J. Räisänen, M. Hautala, and A. Antilla, Nucl. Instr. and Meth. 218 (1983) 785.

[9] E. Friedland, M. Hayes, S. Kalbitzer and P. Oberschachtsiek, Nucl. Instr. and B 85 (1994) 272.

[10] M.A. Meyer and N.S. Wolmarans, Nuclear Physics A 136 (1969) 663.

[11] G. Amsel, E. d'Artemare and E. Girard, Nucl. Instr. and Meth. 191 (1981) 189.

[12] M. Zinke-Allmang, S Kalbitzer and M. Weiser, Nucl. Instr. and Meth. B 15 (1986) 563.

[13] H.H. Andersen and J.F. Ziegler, in: The Stopping and Ranges of Ions in Matter, vol. 3, ed J.F.Ziegler (Pergamon, New York, 1977).

[14] E. Friedland, Nucl. Instr. and Meth. 150 (1978) 301.

[15] K.H.Ecker, M.-P. Macht and V. Naundorf, Nucl. Instr. and Meth B15 (1986) 66.

[16] U. Littmark and J. F. Ziegler, in: The Stopping and Ranges of Ions in Matter, vol. 6, ed J.F. Ziegler (Pergamon, New York, 1980).